

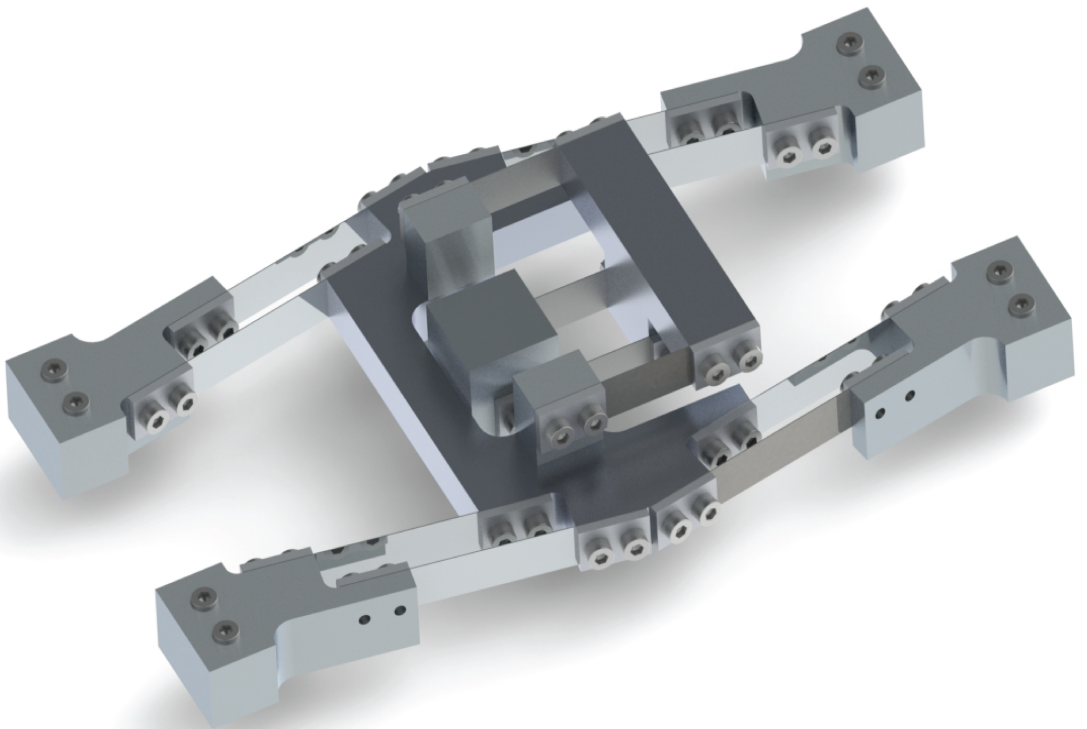
Department of Precision and Microsystems Engineering

Miniaturized Vibration Energy Harvesting from Human Motion

Based on Frequency up-conversion through Impact

Thijs Willem Albert Blad

Report no : 2017.048
Coach : N. Tolou
Professor : J.L. Herder
Specialisation : MSD
Type of report : M.Sc. Thesis
Date : 18 October 2017



VIBRATION ENERGY HARVESTING FROM HUMAN MOTION

BY FREQUENCY UP-CONVERSION THROUGH IMPACT

VIBRATION ENERGY HARVESTING FROM HUMAN MOTION

BY FREQUENCY UP-CONVERSION THROUGH IMPACT

M.Sc. Thesis

In partial fulfillment of the requirements for the degree of
Master of Science in Mechanical Engineering,
at the Department of Precision and Microsystems Engineering,
Delft University of Technology, Delft, The Netherlands
to be defended on Wednesday November 1st, 2017 at 13:45.

by

Thijs Willem Albert BLAD

born in Orandjestad, Aruba.

Report no: 2017.048
Mentor D.F. Machekposhti
Coach: N. Tolou
Professor: J. L. Herder
Specialization MSD
Type of report M.Sc. Thesis
Date: November 1, 2017

This thesis was approved by the thesis committee:

| | |
|-----------------------------|--------------------|
| Prof. dr. ir. J. L. Herder, | PME, 3ME, TU Delft |
| Dr. N. Tolou, | PME, 3ME, TU Delft |
| Ir. D.F. Machekposhti, | PME, 3ME, TU Delft |
| Dr. Ir. C. Ayas | PME, 3ME, TU Delft |

Reserve members

| | |
|--------------------------|--------------------|
| Prof. dr. P.G. Steeneken | PME, 3ME, TU Delft |
|--------------------------|--------------------|



Keywords: Vibration energy harvesting, Frequency up-conversion, Human motion

Printed by: Repro van de Kamp

Front & Back: Marit van de Kamp

Copyright © 2017 by T.W.A. Blad

This thesis is confidential and cannot be made public until November 1, 2019

An electronic version of this thesis is available at
<http://repository.tudelft.nl/>.

*“If you want to find the secrets of the universe, think in terms of energy,
frequency and vibration.”*

Nikola Tesla

Preface

I've always wanted to be an inventor. There has always been this mysterious attraction towards making new things that could do things that were not possible before. Ever since I learned about the topic of energy harvesting, this inner spider-sense went off that told me I wanted to build my own generators. Even after a thousand times, I am still excited when I flip the switch of my first prototype and detect a minuscule flash of the LED. The realization that you have just generated electrical power by rigorously shaking the device back and forth remains one of the most rewarding experiences one can achieve.

My affinity with health care and interests in the field of medical technology lined up perfectly with the application of a generator that harvests energy from human motion to power a hearing aid. Although this particular application will most likely not be realized in the near future, the case provides an extremely interesting set of engineering challenges to be solved. Due to these challenges, human motion is not a particularly convenient source of energy, and the attempt to capture energy from it to power wearable devices has even been referred to as a useless effort by some. Nevertheless, my conviction that with a proper strategy and design the power output would converge towards the theoretical limit formed the basis of a great persistence to continue on a project in a field where virtually insignificant efficiencies are the state-of-the-art.

"It is until you make your own designs that you realize many things are the way they are because somebody liked that particular choice"

*Thijs Willem Albert Blad
Delft, October 2017*

Contents

| | |
|---|------------|
| Preface | vii |
| 1 Vibration energy harvesting from human motion | 1 |
| 1.1 Introduction to energy harvesting. | 2 |
| 1.2 Vibration energy harvesting. | 4 |
| 1.3 Case study | 6 |
| 1.4 Thesis outline. | 6 |
| 2 Energy harvesting from multi-directional sources | 9 |
| 3 Mechanical analysis and design process | 23 |
| 3.1 Introduction | 24 |
| 3.2 Mechanical analysis of the vibration energy harvester | 24 |
| 3.3 Design problem formulation | 30 |
| 3.4 Mechanical design | 31 |
| 3.5 Integration | 43 |
| 3.6 Conclusions. | 44 |
| 4 The Parametric frequency up-converter generator | 45 |
| 5 Reflection, conclusions and recommendations | 63 |
| 5.1 Overview of research activities | 64 |
| 5.2 Successes | 65 |
| 5.3 Unsuccessful attempts | 66 |
| 5.4 Conclusions. | 68 |
| 5.5 Recommendations | 68 |
| Acknowledgements | 71 |
| Appendices | 73 |
| A Collaboration paper | 75 |
| B Design process | 83 |
| C Prototypes and practical work | 89 |
| C.1 Introduction | 89 |
| C.2 Functional vibration energy harvester systems | 89 |

| | | |
|----------|---|------------|
| C.3 | Other manufacturing projects. | 98 |
| D | Technical drawings of PFupCG | 101 |
| E | PRBM models of buckled flexures | 105 |
| E.1 | Pseudo rigid body models of building blocks | 105 |
| E.2 | Compliant models of the building blocks | 115 |
| E.3 | Simulink implementation. | 115 |
| F | Transducer models of piezoelectric beams | 117 |
| F1 | Mechanical Equation of Motion and Modal Analysis of Cantilever Beam | 117 |
| F2 | Electrical coupling modeling | 120 |
| F3 | Constitutive equations of piezoelectric cantilevered beam | 122 |
| F4 | Simulink implementation. | 123 |
| G | Literature search data | 125 |
| G.1 | Multi-DoF vibration energy harvesters | 125 |
| G.2 | Generators with human motion vibration sources | 126 |
| H | References | 127 |
| | References | 127 |

Chapter 1

Vibration energy harvesting from human motion

Thijs BLAD

“If you can't explain it to a six year old, you don't understand it yourself.”

Albert Einstein

This chapter introduces the reader to the topic of energy harvesting by explaining the basic principles and applications. Vibration energy harvesting is introduced as the main research theme of this thesis and an overview of transduction processes is presented. The case study of harvesting from human walking motion to power a hearing aid will be introduced and the outline of the thesis is sketched.

1.1 Introduction to energy harvesting

Energy harvesting is the name for a process that extracts energy from an ambient source and uses it to generate electrical power. Excellent examples of this principle are the 'green-power' solutions such as wind turbines, solar panels or hydro-powered dams. These examples respectively use the ambient energy sources of gas flow, electromagnetic radiation and fluid flow and convert them into electrical energy that can be used to feed the power grid. Another example of an energy harvester is a an electricity generating road, which harnesses the vibrations induced by vehicles to produce electrical power. On a smaller scale, the bicycle dynamo is an example of a human powered energy harvester which can be used to power the lights, or on-board electronics of the bicycle. Other human powered applications can be found in various flashlights, which are equipped with dynamos that provide power shaken, wound or squeezed by hand. One of the earliest miniaturized applications of energy harvesting techniques to power electronic devices is the crystal radio. This device, which was invented in the late 19th century and could play radio signals over a set of earphones, was solemnly powered by energy harvested from the radio waves themselves. A particularly elegant energy harvester is applied in the Seiko kinetic wristwatch, which is powered by the arm swinging motion of the user and is one of the few examples of commercially applied energy harvesting from human motion.

A particularly interesting application was pointed out over 20 years ago, in 1996, by Williams and Yates [1]. They argued that the techniques of energy harvesting could also be applied to power micro-electromechanical systems (MEMS). Billions of those devices were fabricated in the decades to follow and billions more will be fabricated in the future. Electrochemical batteries are the to-go solution for powering all of those devices. As a result of the finite amount of energy that can be stored in a battery, they have to be recharged or replaced. The main advantage of energy harvesting boils down to the virtually unlimited amount of energy that can be extracted from environmental sources. As a result, battery replacement can be postponed or eliminated which amounts to a huge saving in maintenance costs and ecological ramifications.



Figure 1.1: Examples of energy harvester systems; (a) solar panel, (b) bicycle dynamo (c) kinetic wristwatch mechanism [2–4].

1.1.1 Applications and relevance

One of the most prominent applications of energy harvesters are the *wireless sensor networks*. These sensor networks can be applied for purposes such as structural health monitoring, forest fire detection or air pollution monitoring and can therefore greatly increase public safety. Currently, the greatest limiting factor for the mass scale application of these sensor networks is the power supply.

Other applications of energy harvesting are low-power electronic devices at locations that are difficult to access. Complete disassembly of a product may be required if the batteries are inaccessible from the outside, and replacing the batteries of sensors at a very remote location may require a costly expedition. Moreover, replacing the batteries of a device inside the human body, such as a pacemaker, requires a surgery with all corresponding risks.

Lastly, the large-scale energy harvesting processes have received an increasing amount of attention over the past decades as an alternative to fossil fuels due to themes such as climate change, CO₂ emissions. Although their effects are huge compared to the miniaturized generators, a great portion of the energy that was generated will be lost during transport. Therefore, localized energy harvesting is not only a convenient way to power the electronic devices of the future, it is also an efficient way to further reduce our energy consumption by reducing the wasting of energy due to transport.

1.1.2 From ambient energy to useful power

Powering our devices with harvested energy requires the transformation of virtually useless energy from an ambient source into useful electric power. For this transformation two things are fundamentally required: An ambient source with a relevant amount of available energy and a harvesting device that can facilitate this transformation with a relevant efficiency.

The ambient sources of energy where energy can be harvesting from are essentially of four forms: solar, radio frequency (RF) electromagnetic radiation, thermal gradients, and motion. In Tbl. 1.1 a number of these sources and harvesting techniques are compared to energy storage methods. Of those sources direct sunlight contains by far the most harvest-able energy. Moreover, this energy can typically be harvested at very relevant efficiencies which makes this form of energy harvesting an excellent alternative power source. However, the major flaw of this energy source is that the harvest-able power rapidly diminishes when direct sunlight is not available, such as on cloudy days and inside. Techniques for harvesting energy from RF electromagnetic radiation, as in the example of the crystal radio, are very capable of reaching relevant efficiencies. However, the availability of harvest-able energy is highly dependent on the distance to and the broadcasted power of the source. Since the broadcasting of RF energy is limited by regulation this harvesting method is only suitable for extremely low power applications. Thermal gradients can contain relevant power levels and have been successfully used as a power source in military and aerospace applications. However, the efficiencies that

are reached in the transformation of this power source are low and remain dependent on environmental conditions which limits their practical use. The general opinion from the literature is that while each application should be evaluated to find the best energy-harvesting method, kinetic energy in the form of motion or vibration is generally the most versatile and ubiquitous ambient energy source available [5].

| Energy source | Power density ($\mu\text{W cm}^{-3}$) one year lifetime | Power density ($\mu\text{W cm}^{-3}$) 10 year lifetime |
|---------------------------------------|--|---|
| Solar (outdoors) | 150-15.000 | 150-15.000 |
| Solar (indoors) | 6 | 6 |
| Vibrations (piezoelectric conversion) | 250 | 250 |
| Acoustic noise (75dB) | 0.003 | 0.003 |
| Acoustic noise (100dB) | 0.96 | 0.96 |
| Temperature gradient (10 K) | 15 | 15 |
| Heel strike | 330 | 330 |
| Batteries (regular) | 45 | 3.5 |
| Hydrocarbon fuel (micro heat engine) | 333 | 33 |
| Fuel cells (methanol) | 280 | 28 |

Table 1.1: Comparison of power densities of various energy sources and harvesting technique (top) with energy storage methods (bottom) [6].

1.2 Vibration energy harvesting

Any structure or system that moves, shakes, rotates or is subject to flow of fluid or air is vibrating. These vibrations are a direct result of the mechanical energy that is stored in the system. Given the right conditions, large amounts of energy can build up in a vibrating system. Vibrations are generally undesired as they may lead to instability and even breakdown the system. Therefore, damping is often used to limit the energy that can build up in vibrating systems by dissipating energy. Instead of dissipation of the vibration energy into mostly heat, the energy can be transformed into useful electrical energy. This electrical energy can then be stored and used as a power source. The systems that employ this process of 'recycling' the energy in the vibrations of mechanical structure are grouped by the term *vibration energy harvesters* (VEH) or generators. In essence, a generator can fulfill two functions simultaneously: damping of undesired vibrations, and the generation of useful power. This capability makes vibration energy harvesters extremely interesting devices for a wide range of environments.

1.2.1 Transduction processes

The core of vibration energy harvesting devices is formed by a transducer. The transducer is an embodiment of one or more physical processes that convert the mechanical vibrations to electrical power. These *transduction* processes exhibit a special coupling between the mechanical and electrical domains. This coupling allows energy to flow from one domain to the other. The four transduction processes that are commonly used in vibration energy harvesters are piezoelectricity, magnetostriction, electrostriction and

| Process | Physical domains | Working principle |
|-------------------|----------------------------------|--|
| Piezoelectricity | Mechanical, electrical | Charge generation resulting from deformation of a polarised atomic structure. |
| Magnetostriction | Mechanical, electrical, magnetic | Change in a magnetic field strength due to mechanical load, electromagnetic induction generates a current in the surrounding coil. |
| Electrostriction | Mechanical, electrical | A change in capacitance with a given electrical charge, resulting in a voltage change. |
| Electromechanical | Mechanical, electrical, magnetic | Electromagnetic induction of a coil passing through a magnetic field. |

Table 1.2: A number of transduction mechanisms suitable for power harvesting [7]

electromechanical couplings. These processes, the physical domains which they interact with and a brief summary of their working principles are presented in Tbl. 1.2.

Piezoelectricity is a form of coupling between the mechanical and the electrical behaviors that is observed in specific crystals, ceramics and polymers. The coupling consists of the *piezoelectric* and the inverse piezoelectric effects that were discovered by Pierre and Jacques Curie in 1880 and 1881. The piezoelectric effect describes the phenomenon in which an electrical charge is induced on the material surface due to mechanical stress. As the name suggests, the inverse piezoelectric effect describes the phenomenon in which strain is induced in response to an applied electric field. An example of a piezoelectric transducer can be found in electric lighters.

Magnetostriction is the magnetic equivalent of the piezoelectric effect. In magnetostrictive materials a deformation is induced by placing them in a magnetic field. Its inverse known as the *Villari effect* is the working principle for the magnetostrictive transducer. Due to an applied mechanical stress the magnetostrictive material is magnetized. By placing this material inside a conductive wire loop, a voltage can be induced.

Electrostrictive transduction processes rely on using a variable capacitor structure to generate charges from a relative motion between two plates. By changing the distance between or the overlap of the two plates, an electric voltage or current can be induced. In order to provide transformation of relevant quantities of energy, the capacitor plates must be precharged. The two commonly used methods for this are the use of a power source that provides a voltage difference or the use of *electret* material which exhibits this property itself. The voltage is limited by either breakdown of the dielectric medium, or the attached circuit components.

Electromechanical couplings are the working principle of electric drives and dynamos. Governed by Faraday's law of induction, a changing magnetic field induces a voltage in a conductor. In a dynamo, a permanent magnet is rotated within a coil of conductive wire which results voltage over the terminals. Some electric cars cleverly demonstrate this coupling in both ways: acceleration is facilitated by the motor using electric energy from the battery, and electric energy is recovered when braking.

Of all the transduction processes, piezoelectricity has received the greatest attention in research and is generally considered to be the most promising transduction process for miniaturized vibration energy harvesting devices. The main reasons for this are the large power densities and ease of application [8].

1.3 Case study

The specific examples used throughout this thesis will be based on the case study of a vibration energy harvester for a hearing aid that is powered by human walking motion. Therefore, the vibration conditions in the human head area will be the targeted source of mechanical energy. Furthermore, general user comfort requirements w.r.t. size and weight will be taken into consideration in the design.

1.4 Thesis outline

In this thesis the main line of research is the vibration energy harvesting from human motion. The following sub-topics are included in these lines of research. Vibration energy harvesting from multi-directional motion sources, harvesting from low-frequency-large-amplitude vibrations, frequency up-conversion, compliant mechanisms and piezoelectric transducers.

The second chapter of this work presents the resulting research paper of the literature review phase on the topic of vibration energy harvesting from multi-directional motion sources. In this chapter, a categorization, analysis and optimization of the strategies to harvest from a 2D vibration environment are presented. This resulted in the development of a design metric and corresponding flowchart to guide a designer in the selection of a MDoF strategy. The process was demonstrated for the considered case study and it was found that under the optimal conditions the power output of a generator would have an upper limit of 10mW. This was considered a workable figure for powering a 1 mW hearing aid and it was concluded that the case study was feasible.

The third chapter covers the topics of harvesting from low-frequency-large-amplitude vibrations, frequency up-conversion and compliant mechanisms. The analysis of this chapter shows that the classical models from literature are unfit for the case study due to a scaling problem in the transducer damping characteristics. To address this problem, a new concept based on the frequency-up conversion strategy is proposed, called the parametric frequency up-converter (PFupCG). The background, design process and mechanical analysis that led to this concept are presented in this chapter.

The results of the design phase are presented in the design paper that forms the fourth chapter. In this paper, the PFupCG concept is presented along with a theoretical framework and generalized model. Simulation of the model with a Q -factor of 0.2 for the vibration conditions of the case study showed that the PFupCG can have a significantly higher

power output compared to the classical models when the scaling problem of the damping is considered in the analysis. Moreover, the dynamical properties of the PFupCG were validated using a prototype and experiment.

The fifth and final chapter contains a critical reflection of the author on the process and the results and present the conclusions, recommendations and directions of future work.

To preserve a clear focus on the main line of research and keep the thesis concise, work that did not directly add to the main conclusions was not included in the thesis. Instead, the following appendices were added. Appendix [A](#) presents the resulting paper of a collaboration project on the thermal damage of laser micro-machining piezoelectric material. Appendix [B](#) shows schematics, drawings and methods that were used in the design process. Appendix [A](#) demonstrates the practical work done in this project and includes manufacturing methods, pictures of resulting prototypes and practical tips regarding the prototyping of energy harvesters. In Appendix [D](#) the technical drawings of the final concept are included for reproduction. Appendices [E](#) and [F](#) describe the modeling procedures used in the modeling of compliant flexures and piezoelectric transducers, respectively. Lastly, two tables with an overview of the literature search data are presented in appendix [G](#).

Chapter 2

Energy harvesting from multi-directional sources

Thijs BLAD

"If I have seen further, it is by standing on the shoulders of giants."

Isaac Newton

In this chapter, the resulting research paper of the literature review phase on the topic of vibration energy harvesting from multi-directional motion sources is presented. A categorization, analysis and optimization of the strategies to harvest from a 2D vibration environment are presented. This resulted in the development of a design metric and corresponding flowchart to guide a designer in the selection of a MDoF strategy. The process was demonstrated for the considered case study and it was found that under the optimal conditions the power output of a generator would have an upper limit of 10 mW. This was considered a workable figure for powering a 1 mW hearing aid and it was concluded that the case study was feasible.

Originally appeared as: "Design Metric for Vibration Energy Harvesting from Multi-Directional Motion Sources" by T.W.A. Blad, D. Farhadi Machekposhti, J.L. Herder, A.S. Holmes and N. Tolou which was submitted for review at the Journal of Smart Materials and Structures. The article was reformatted to fit the style of the thesis.

Design Metric for Vibration Energy Harvesting from Multi-Directional Motion Sources

T.W.A. Blad, D. Farhadi Machekposhti, J.L. Herder, A.S. Holmes and N. Tolou

Abstract—Vibration energy harvesting can be used as a sustainable power source for various applications. Usually, the generators are designed to harvest from a single degree of freedom (SDoF) in the direction with the largest vibration power. In this research, harvesting from multi-directional translational motion sources will be investigated. Three strategies are assessed: a reference SDoF generator, a SDoF generator using an orientation strategy, and a Multi Degree of Freedom (MDoF) system. This led to the development of a design metric and a flowchart by which any 2D design problem can be described by two dimensionless parameters: the relative strength of vibrations, p_v , and the relative dimension of the design space, p_l . It was shown that the relative power density (RPD) of a 2DoF system compared to a reference SDoF system only depends on the product $p^* = p_v p_l$, and has a maximum of 1.185 for $p^* = 1$.

The application of powering a hearing aid for children is investigated as a case study. The components of vibrations in the area of the human head while walking are found to be represented by a two-directional vibration source with $p_v = 0.55$. Three different design spaces are assessed for a miniaturized generator and three different optimal embodiments are found. For one of the considered situations where $p^* = 1.1$, a 2DoF system was found to have a 16% higher power output compared to a SDoF reference.

Index Terms—Vibration energy harvesting, Multi degree of freedom, Multi-direction, Human motion, Head area.

I. INTRODUCTION

VIBRATION energy harvesting has been investigated for over 20 years since the early work of Williams and Yates in 1996 [1] which investigated the piezoelectric, electromagnetic, and electrostatic transduction

mechanisms for the purpose of vibration-to-electric energy conversion. Devices that incorporating such a transduction mechanisms, called vibration energy harvesters (VEH) or generators have received much interest as they may provide an alternative to batteries in powering microelectronic devices such as wireless sensors for biomedical applications. The work at hand was motivated by the desire to develop a VEH for the purpose of powering a hearing aid for children. Children make up 32 million of the individuals that suffer from disabling hearing loss [2]. The impact of hearing loss on these children is a significantly reduced ability to communicate, which greatly affects their ability to follow education, and therefore, their future. Especially in developing countries the dependency on batteries limits the availability of hearing aids. Therefore, a sustainable power source in the form of a vibration EH can provide a resolution.

Three fundamental types of VEHs can be identified: the velocity-damped resonant generator (VDRG), the Coulomb-damped resonant generator (CDRG) and the Coulomb-force parametric generator (CFPG) [3]. Here, the case of a VDRG at the location of the human head that harvests from walking-induced vibrations is studied. It was estimated that in an ideal case up to 160 mW can be harvested from the vertical head movement with a 5 cm³ device [4]. As hearing aids typically require 1-2 mW [5] they fall within the scope of possibilities. However, in practice ambient vibrations are not perfect sinusoids, have varying frequencies and may

have components along multiple orthogonal directions [6]–[8]. Moreover, the SDoF devices that are considered by the majority of EH literature have the fundamental flaw that the driving magnitude of the acceleration will be reduced by the sine of the misalignment angle between the vibration component and the DoF of the device [9]. Therefore, two problems emerge: firstly, only a single vibration direction can be harvested, essentially wasting the energy in orthogonal directions. Secondly, in situations where the directions of the vibrations are unknown or change over time, the large misalignment angle with respect to the vibration source will severely reduce the performance of the EH.

To assess these problems a wealth of recent research involved the development of MDoF VDRGs [9]–[21] and CDRGs [22]–[36]. These MDoF generators allow simultaneous energy harvesting in multiple orthogonal directions. As a result they are capable of providing output power regardless of their orientation with respect to the vibration source. Moreover, it has been shown that by using a MDoF design a broader bandwidth [37]–[39] and a higher power output [40], [41] can be realized.

On-chip MEMS generators with surface areas of 1 mm^2 have recently been demonstrated to harvest power from vibrations in 2-D [23] and 3-D [31] by means of an electrostatic transduction mechanism. Larger scale devices have shown to be capable of harvesting power in the mW range [16], [20]. An overview of the specifications of recently published MDoF designs can be found in table I.

Despite these recent advances there is still a lack of in-depth knowledge on how MDoF EH will perform relative to their SDoF counterparts. Moreover, to the best of the author’s knowledge, no general guidelines have been published that aid the designer in identifying situations where MDoF harvesting can be beneficial. This lack of knowledge can result in the inability of the designer to see the benefit of a MDoF system in the given situations, or the application of MDoF systems

in situations where they are highly inefficient.

Therefore, the objective of this research is to present a novel design metric for vibration energy harvesting from a multi-directional translational source. With this metric and corresponding flowchart the designer can be able to identify and quantify the situations where MDoF systems are expected to outperform SDoF systems in terms of power density, and therefore design the proper system for their particular case.

Part II will present a general method for the assessment of energy harvesting from a multi-directional translational source by means of three strategies, and a theoretical maximum for the relative power density (RPD) of a 2DoF system compared to a SDoF system will be derived. This method will be applied to a planar case study in part III. Part IV will discuss the found results, the design of a suspension, non resonance applications and the challenges that may arise upon implementation. Lastly, the most important conclusions will be summarized in part V.

II. METHODS

A. Calculation of output Power for a SDoF VDRG

A single DoF energy harvester device can be modeled by a mass-spring-damper system consisting of a proof mass, m , and a housing that are connected by a spring, k , and a damper, c , in parallel as shown in Fig. 1.

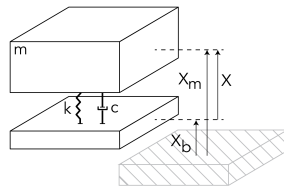


Fig. 1: The harvesting of energy from movement can be modeled by a mass-spring-damper system.

In this model the proof mass oscillates due to excitation of the housing and the energy harvesting transduction process is modeled by

TABLE I: Overview of recent publications in the field of MDoF energy harvesting; TD = transduction mechanism, M = electromagnetic, S = electrostatic and P = piezoelectric.

| Source | Year | TD | DoF | Frequency [Hz] | Acceleration [g] | Area [mm ²] | Volume [cm ³] | Power output [W] |
|-----------------------|------|----|-----|----------------|------------------|-------------------------|---------------------------|------------------|
| Crovetto et al. [23] | 2013 | S | 2 | 179 | 0.03 | 1.0 | | 3.3E-08 |
| Tao et al. [31] | 2014 | S | 3 | 66 | 0.05 | 1.2 | | 4.8E-09 |
| Wu et al. [16] | 2014 | P | 2 | 37 | 0.2 | | 260 | 2.9E-03 |
| Aktakka et al. [10] | 2015 | P | 3 | 387 | 0.05 | | 2.5 | 5.3E-05 |
| Gutierrez et al. [11] | 2015 | M | 2 | 8.2 | 0.2 | | 1.2 | 1.0E-04 |
| Tao et al. [32] | 2015 | S | 2 | 125 | 0.2 | 3.6 | | 1.2E-07 |
| Zhao et al. [20] | 2016 | P | 3 | 16 | 0.5 | | 13 | 3.3E-04 |

the damper. The dynamics of the system are described by the following equation of motion [42].

$$m\ddot{x} + c\dot{x} + kx = -m\ddot{x}_b. \quad (1)$$

Where c is the damping coefficient, k the spring stiffness and $x = x_m - x_b$ the relative displacement which is defined as the difference between the displacement of the mass, x_m , and the displacement of the housing, x_b . During periodic movements such as walking, the vibration of the housing, which is connected to the head, can be modeled by a sinusoid with amplitude, X , and frequency, ω . Following the derivation of Goll et al. the power output of a VDRG at resonance can be found by the following equation [4].

$$P = \frac{\omega^3 m X^2}{4\zeta}, \quad (2)$$

Where ζ is the damping ratio of the system. Under the assumption of no parasitic damping the power output is limited by the maximal stroke, S_x , of the proof mass [3]. The corresponding damping factor is given by Eq. 3.

$$\zeta = \frac{X}{2S_x}. \quad (3)$$

With this damping factor the maximal power can be found for an input vibration with a frequency and amplitude for a given stroke and mass. Since frequency and RMS accelerations, $A_{x,\text{RMS}}$, are often measured to classify the power in the ambient vibrations, the formulation can be rewritten using the relation $X\omega^2 = \sqrt{2}A_{x,\text{RMS}}$. Therefore, the following formulation can be used:

$$P = \frac{\sqrt{2}}{2} \omega A_{x,\text{RMS}} m S_x. \quad (4)$$

B. Expansion to multi-directional translational sources

Ambient vibrations may occur in up to three orthogonal directions and can be modeled as vectors, \vec{v}_i .

$$|\vec{v}_i| = \omega_i A_{i,\text{RMS}}. \quad (5)$$

The frequencies and accelerations that determine the magnitudes of the vectors \vec{v}_i are unique for every environment and can be found from literature or experimentally as discussed in section III-A. The vectors are ranked based on their magnitudes such that $|\vec{v}_1| > |\vec{v}_2| > |\vec{v}_3|$. Likewise, up to three orthogonal DoF of the EH can also be modeled as vectors, \vec{e}_j .

$$|\vec{e}_j| = m S_j. \quad (6)$$

The orientations and magnitudes of \vec{e}_j are dependent of the material and geometry of the device and are primarily limited by the design space. Under the assumption that spring-damper systems do not have a volume claim the design space can be used for either more mass or longer strokes. For the general case of a design space with dimensions $l_1 \times l_2 \times l_3$ and a system with strokes of S_1, S_2, S_3 the inertia of a proof mass with a density of ρ can be found.

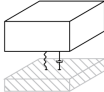
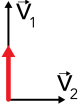
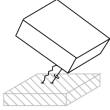
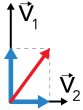
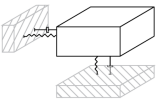
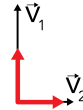
$$m = \rho(l_1 - 2S_1)(l_2 - 2S_2)(l_3 - 2S_3). \quad (7)$$

Therefore, the vectors \vec{e}_j

$$|\vec{e}_j| = \rho(l_1 - S_1)(l_2 - 2S_2)(l_3 - 2S_3) S_j. \quad (8)$$

This results in a general expression for the power output of an arbitrary energy harvester with N DoF exposed to ambient vibrations in three directions:

TABLE II: Systems can be categorized in three categories depending on the strategies they use to harvest ambient vibrations. The first category systems harvest only from the vibration direction that is aligned with their DoF. The second category and third categories contain systems that can harvest from a multi-directional source. This is done by employing an orientation strategy or using a MDoF system, respectively.

| Category | Harvester DoF $\vec{\epsilon}_j$ | Harvest able directions \vec{v}_i | Schematic representation | Vector representation |
|----------------------|--|-------------------------------------|---|--|
| Reference | Single, $\vec{\epsilon}_1$ | Single, \vec{v}_1 |  |  |
| Orientation strategy | Single, $\vec{\epsilon}_1$ | Multiple, \vec{v}_1, \vec{v}_2 |  |  |
| MDoF systems | Multiple, $\vec{\epsilon}_1, \vec{\epsilon}_2$ | Multiple, \vec{v}_1, \vec{v}_2 |  |  |

$$P_{\text{general}} = \frac{\sqrt{2}}{2} \sum_{j=1}^N \sum_{i=1}^3 \vec{\epsilon}_j \cdot \vec{v}_i. \quad (9)$$

C. Performance assessment of strategies for harvesting from vibrations in multiple directions

When considering harvesting from multi directional motion sources the systems can be categorized based on the strategy that is used to harvest energy from the ambient vibrations. Three categories are identified: a reference, SDoF systems using an orientation strategy and the MDoF systems.

1) *Reference category*: This category contains the systems with a single DoF , $\vec{\epsilon}_1$, that harvest power from a single-directional vibration source , \vec{v}_1 . Hence, the system has only one nonzero stroke, S_1 , and Eq. 8 can be simplified.

$$|\vec{\epsilon}_1| = \rho l_2 l_3 (l_1 S_1 - 2S_1^2). \quad (10)$$

The maximum for $|\vec{\epsilon}_1|$ can be found for $S_1 = \frac{l_1}{4}$. Furthermore, the DoF is aligned with a single vibration source and as a result the maximal harvested power can be found.

$$P_{\text{reference}} = \frac{\sqrt{2}}{2} |\vec{\epsilon}_1| |\vec{v}_1| = \frac{\sqrt{2}}{16} \rho l_1^2 l_2 l_3 |\vec{v}_1|. \quad (11)$$

2) *Orientation strategy*: In this category the SDoF systems, $\vec{\epsilon}_1$, are found that harvest energy from a multi-directional vibration source, \vec{v}_i . Similar to the first category, these system have only one nonzero stroke, S_1 , and Eq. 10 can be used to find $\vec{\epsilon}_1$. The difference with the reference category is that the DoF may be oriented arbitrary. Therefore, the power output can be found by the sum of the projections of all vibrations on the DoF of the system:

$$P_{\text{orientation}} = \frac{\sqrt{2}}{2} \sum_{i=1}^3 \vec{v}_i \cdot \vec{\epsilon}_1. \quad (12)$$

For these systems the orientation of the DoF is a design variable, which means that it can be optimized for maximum power output. This optimal direction is found through means of a principle component analysis (PCA) on the data of ambient vibrations. From the PCA a set of orthogonal vectors is found, called principle components, that describe the original data. The first principle component contains most variance and the last principle component contains least. For maximum power output the DoF of the system should be oriented in the direction of the first principle component. Furthermore, it is assumed the design space as a whole can be rotated in the direction of the DoF such that the same method as described

under the reference category can be used without violating the geometrical constraints.

3) *MDoF systems*: This category contains systems with multiple DoF, $\vec{\epsilon}_j$ that harvest energy from a multi-directional vibration source, \vec{v}_i . The general formula for the power that can be harvested with a N DoF system was given in Eq. 9. Simplifying to a planar case with two translational DoF, $\vec{\epsilon}_1, \vec{\epsilon}_2$, leaves two nonzero strokes, S_1, S_2 . Therefore, the following equations are obtained from Eq. 8.

$$\begin{aligned} |\vec{\epsilon}_1| &= \rho l_3 (l_2 - 2S_2)(l_1 S_1 - 2S_1^2), \\ |\vec{\epsilon}_2| &= \rho l_3 (l_1 - 2S_1)(l_2 S_2 - 2S_2^2). \end{aligned} \quad (13)$$

For a bi-directional vibration source with 2 components, \vec{v}_1, \vec{v}_2 , that are aligned with the harvester DoF the output power of the system can be found.

$$\begin{aligned} P_{2\text{DoF}} &= \frac{\sqrt{2}}{2} (|\vec{\epsilon}_1||\vec{v}_1| + |\vec{\epsilon}_2||\vec{v}_2|), \\ &= \frac{\sqrt{2}}{2} \rho l_3 (l_1 - 2S_1)(l_2 - 2S_2) (S_1|\vec{v}_1| + S_2|\vec{v}_2|). \end{aligned} \quad (14)$$

Stationary points can be found for S_1 and S_2 resulting in the following expressions.

$$\begin{aligned} S_1 &= \frac{1}{4}l_1 - \frac{1}{2}S_2 \frac{|\vec{v}_2|}{|\vec{v}_1|}, \\ S_2 &= \frac{1}{4}l_2 - \frac{1}{2}S_1 \frac{|\vec{v}_1|}{|\vec{v}_2|}. \end{aligned} \quad (15)$$

Substituting finds the optimum values for S_1 and S_2 for the given design space dimensions, l_1, l_2 , and ambient vibration strengths, $|\vec{v}_1|, |\vec{v}_2|$.

$$\begin{aligned} S_1 &= \frac{1}{3}l_1 - \frac{1}{6} \frac{|\vec{v}_2|}{|\vec{v}_1|} l_2, \\ S_2 &= \frac{1}{3}l_2 - \frac{1}{6} \frac{|\vec{v}_1|}{|\vec{v}_2|} l_1. \end{aligned} \quad (16)$$

The result of Eq. 16 is accurate as long as $S_1 > 0$ and $S_2 > 0$. Effectively, this does not apply to scenarios where one of the dimensions is considerably larger or one of the vibrations is considerably stronger. In these scenarios one

of the strokes becomes zero and a system of the first category is obtained. However, when nonzero values are found for both S_1 and S_2 the maximal harvest able power of the system can be found by the following equation.

$$P_{2\text{DoF}} = \frac{\sqrt{2}}{108} \rho l_3 \frac{(l_1|\vec{v}_1| + l_2|\vec{v}_2|)^3}{|\vec{v}_1||\vec{v}_2|}. \quad (17)$$

D. Relative power density as a general design metric for comparison of strategies when harvesting from a multi-directional vibration source

A general design metric is developed for 2DoF case to help the designer select a strategy for harvesting from a bi-directional vibration source. First, two dimensionless parameters are introduced: the relative vibration strength, $p_v = \frac{|\vec{v}_2|}{|\vec{v}_1|}$, and the relative design space dimensions, $p_l = \frac{l_2}{l_1}$. Using the product of these parameters, $p^* = p_v p_l$, the output power of a 2DoF system, given by Eq. 17, can be compared to the output power of a SDoF system, given by Eq. 11. As a result, the relative power density (RPD) can be found.

$$\text{RPD} = \frac{P_{2\text{DoF}}}{P_{\text{reference}}} = \begin{cases} \frac{4}{27} \frac{(p^*+1)^3}{p^*} & \text{if } 0 \leq p^* \leq 1, \\ \frac{4}{27} \frac{(p^*+1)^3}{(p^*)^2} & \text{if } 1 \leq p^* \leq 2. \end{cases} \quad (18)$$

This metric is visualized in the Fig. 2. In the top plot, a surface of the parameters p_v and p_l is shown such that contours of equal p^* are obtained. The numbers on the contour lines, and the vertical axis of the bottom plot, represent the RPD.

E. Flowchart for designers

According to this metric the flowchart shown in Fig. 3 can be developed to provide a simple guideline for the designer. First, effort should be made to classify the vibration source in terms of the vectors \vec{v}_i . If it is found that $|\vec{v}_1|$ is significantly larger than $|\vec{v}_2|$ the source can be considered as a single-directional vibration source. Therefore, a SDoF system should be

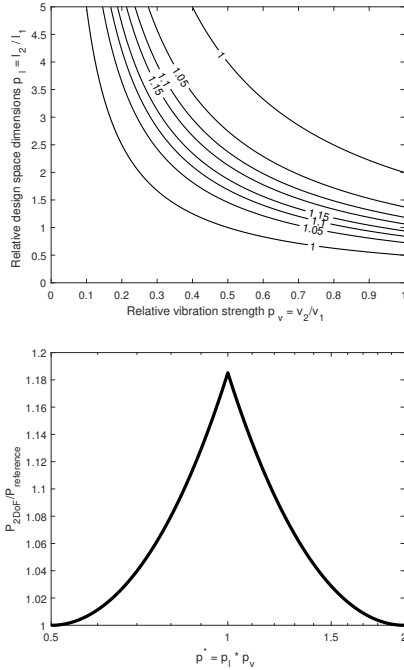


Fig. 2: Any design problem can be quantified by the two dimensionless parameters, p_v and p_l , and their product p^* . The RPD as calculated by Eq. 18 can be shown as a surface of p_v and p_l (top), or function of p^* (bottom). It can be seen that Eq. 18 has a maximum of 1.185 for $p^* = 1$.

designed with its DoF aligned with \vec{v}_1 . However, if it is found that a relevant amount of power is available in both directions the source must be considered as multi-directional. Next, the design space should be assessed. If the design space can be rotated in arbitrary directions, the orientation strategy is favored. In the other case the condition formulated in Eq. 19 should be evaluated. If this condition is satisfied, a 2DoF system should be designed since $RPD > 1$.

$$\frac{1}{2} < p^* < 2. \quad (19)$$

III. RESULTS

A. Obtaining ambient vibration data

For the case study of this research vibrations in the area of the human head during walking are studied. Scientific publications were

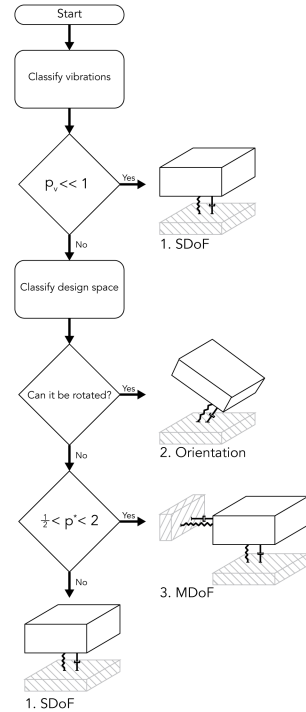


Fig. 3: Flowchart developed to aid the designer in selecting a strategy to harvest from ambient vibrations.

searched in the databases of Google Scholar, Scopus, Web of Science and PubMed using the terms human motion, walking, gait, head area, acceleration, energy harvesting. The following criteria were used to include publications in the dataset.

- The publication must contain measurements on frequency and RMS acceleration or frequency and vibration amplitude.
- Vibrations must be measured in three orthogonal directions under the same conditions.

Frequency and acceleration data was extracted from 11 publications [43]–[53] using the methods shown in table III for vibrations in anterior-posterior, *AP*, mediolateral, *ML*, and caudal-cranial, *CC*, directions. These directions are represented by the x , y and z axes, respectively.

From PSD diagrams of the vibrations recorded

TABLE III: Methods of data analysis used to generalize the information found in scientific publications. Quantities for the frequency, F , linear acceleration, A , and amplitude, d , are given in SI units; the step frequency, f , in $\frac{\text{steps}}{\text{s}}$ and the acceleration, a , in g .

| # | Formula | Applied to |
|-----|--|-----------------------|
| (1) | $F = 2\pi f$ | All |
| (2) | $F = \pi f$ | All |
| (3) | $A = 9.81 \cdot a$ | [44]–[47], [50], [52] |
| (4) | $A = \frac{1}{\sqrt{2}} \cdot (F)^2 \cdot d$ | [43] |

during walking was found that AP and CC directions show their largest peak at the step frequency and ML direction shows its largest peak at half the step frequency [43], [54]–[56]. Therefore, methods (1) and (2) are used to find the predominant signal frequency. Since accelerations are usually presented in g , method (3) is used to convert to SI units. Lastly, the vibrations are assumed to be of sinusoidal nature, consequently the acceleration can be calculated by multiplying the amplitude by the frequency squared as shown in method (4).

The frequencies and accelerations in the vibration signals are shown in the scatter plot in Fig. 4. The frequencies in AP and CC direction have a mean and standard deviation of 1.84 ± 0.33 Hz and in ML direction the frequencies are half of these 0.92 ± 0.16 Hz. The accelerations were found to be $1.28 \pm 1.08 \text{ m s}^{-2}$ in the AP direction, $0.88 \pm 0.49 \text{ m s}^{-2}$ in the ML direction, and $2.46 \pm 1.39 \text{ m s}^{-2}$ in the CC direction.

B. Harvesting strategy selection

From the results of the literature search \vec{v}_i can be determined. Mean values of 15.9 m s^{-3} , 5.3 m s^{-3} and 30.4 m s^{-3} were found for \vec{v}_x , \vec{v}_y and \vec{v}_z , respectively. It was found that the vibrations in z and x direction contain relevant harvest able power. Therefore, these directions are selected as \vec{v}_1 and \vec{v}_2 and relative vibration ratios ranging from $p_v = 0.36$ to $p_v = 0.63$ were found.

The metric described in the previous section can be applied to this case study. Fig. 5 shows the contours of the RPD for the two

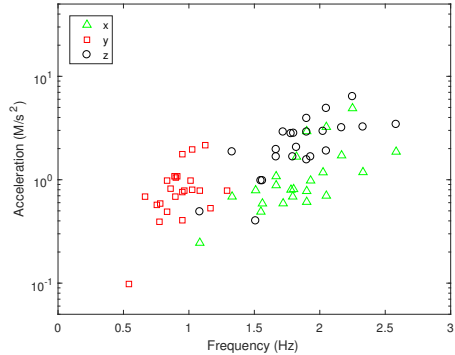


Fig. 4: Scatter plot of the frequencies and RMS accelerations found in the vibrations of the head during walking. Vibrations in z and x directions are identified as \vec{v}_1 and \vec{v}_2 , respectively.

dimensionless parameters p_v and p_l . The area that includes the values for p_v representative for this case study is marked with blue. We consider three cases with a value of $p_v = .55$ and values for the other dimensionless parameter of $p_l = .5$, $p_l = 2$ and $p_l = 4.5$.

For a device with a proof mass made out of steel with a density of $\rho = 8.05 \times 10^3 \text{ kg m}^{-3}$, a total device volume of 10 cm^3 and a thickness of $l_3 = 5 \text{ mm}$ the resulting dimensions and power outputs are given in table IV. It can be seen that in the case of $p_v = 2$ an RPD of 1.16 was found.

TABLE IV: Power assessment for the three considered design spaces for a 10 cm^3 generator. It can be seen that in the second scenario a 16% increase in output power can be achieved by using a 2DoF system.

| Case | Dimensions $l_1 \times l_2 \times l_3$ | Harvester type | Mass | Power output |
|-------------|--|----------------|--------|--------------|
| $p_l = .5$ | 44.7 x 22.4 x 10 mm | SDoF (z) | 40.3 g | 9.68 mW |
| $p_l = 2$ | 22.4 x 44.7 x 10 mm | SDoF (z) | 40.3 g | 5.06 mW |
| | 22.4 x 44.7 x 5 mm | 2DoF | 35.8 g | 5.88 mW |
| $p_l = 4.5$ | 14.9 x 67.1 x 10 mm | SDoF (x) | 40.2 g | 7.59 mW |

When the orientation strategy is considered the DoF of the harvester should be oriented in the direction of the first principle component, $P\vec{C}_1$.

$$P\vec{C}_1 = \begin{bmatrix} 0.5891 \\ 0.8081 \end{bmatrix}. \quad (20)$$

Under the assumption that the design space may be rotated such that the largest direction is aligned with $P\vec{C}_1$ the power output in the

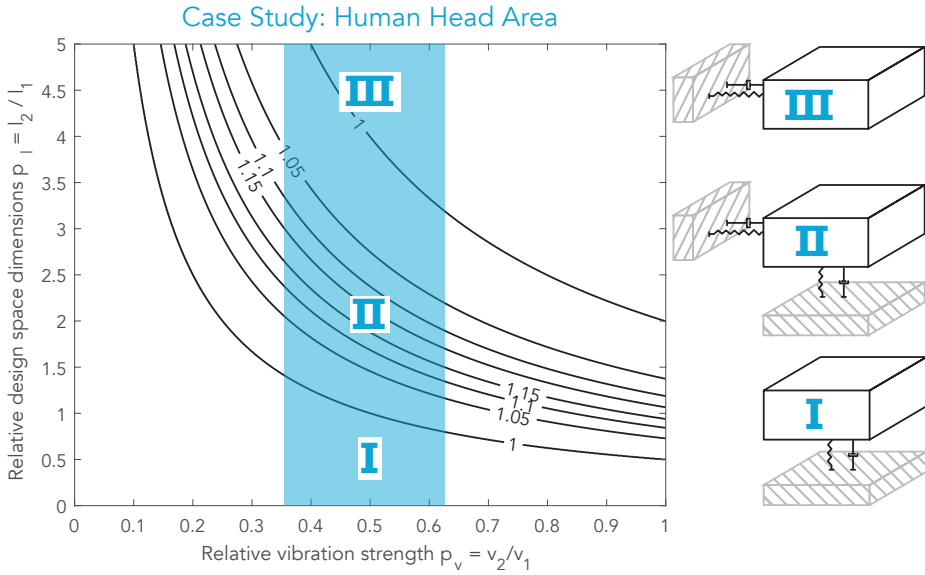


Fig. 5: Case study of vibrations in the area of the human head during walking are indicated with the blue area. Three embodiments of harvesting systems are suggested and their power outputs are assessed in table IV. It can be seen that in scenario II a 2DoF system outperforms a SDoF system in terms of power output.

cases $p_l = .5$ and $p_l = 2$ are equal and found to be $10.92 \times 10^{-3} \text{ W}$.

IV. DISCUSSION

In the method section it was found that the situations where a 2DoF system outperforms a reference SDoF system can be identified by Eq. 19, and quantified by the RPD. In the results section this was confirmed for a situation of $p^* = 1.10$ when a 16% increased power output was found for the 2DoF system compared to the reference SDoF. Furthermore, it was found that in any situation that allows rotation of the design space an orientation strategy would provide the most power output. The values that are presented here, however, are theoretical maximum assuming perfect operating conditions. In this section, the practical validity of these assumptions will be assessed. Furthermore, the design metric will be used to evaluate the prior art and the results of the case study will be discussed.

A. Resonance operation

In the analysis the power output was calculated at the resonance condition of a VDRG. Depending on the application and the vibration source, operation at resonance may not always be guaranteed and could result in reduced power output. In the case studied in this research the human walking motion acts as the vibration source. It was found that this particular source is characterized by low frequencies and large amplitudes relative to the internal stroke of a miniaturized generator. As a result, the system is of an over-damped nature and is characterized by a low and wide frequency response compared to the high and thin resonance peaks found in most industrial applications. Therefore, slight deviations of the source frequency will not result in large drops of output power.

B. Orientation strategy implementation

Using an MDoF generator allows energy harvesting in multiple axes such that multi-directional sources can be harvested more efficiently, and the system becomes more robust

to a misalignment between the source and the DoF. However, a MDoF system requires nonzero strokes in multiple directions which reduces the total mass of the system. Since mass is proportional to the available maximum power, this will reduce the power output. Therefore, a generator using the orientation strategy may perform better since it has only a single DoF and harvests the projected power of the vibration signals upon this DoF. However, this projection treats the vibration as a vector and does not take into account the frequencies and phases of the real signals. For two vibrations signals of equal frequency but with a shift in phase a trajectory, known as a Lissajous figure, can be found. Within this trajectory a line can be drawn that resembles the DoF of the harvester. The power output for such a harvester is proportional to the length of the line. In Fig. 6 the trajectories and corresponding harvester axis are plotted for the case of $p_v = .55$, corresponding to the case study of vibrations in the area of the human head, for phase shifts of 0, 45 and 90 degrees. It can be observed that most power can be harvested from vibrations that are in phase, and that a phase shift results in an overall lower power output. In the special case of a 90 degrees phase shift between the vibration signals, the orientation strategy provides no benefit over the regular SDoF system.

When the vibration signals are of a different frequency their combined signal cannot be harvested efficiently since the suspension can only have one natural frequency. Therefore, an auxiliary frequency up-conversion mechanism could be used to increase the frequency of the lower vibration signal by a certain factor. However, the practical feasibility of such a solution will generally be inferior to using a MDoF system.

C. MDoF complexity and suspension design

Inevitably, a MDoF system requires the design of a more complex transducer and suspension structure, thereby sacrificing mass. During the analysis the simplification has been made of a zero volume claim transducer and suspension structure. Although the volume claim of the

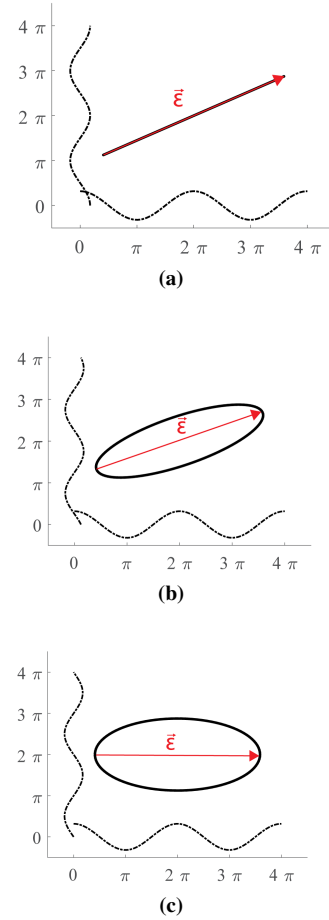


Fig. 6: Different trajectories designed to harvest from 2 vibrations with a phase shifts. The arrow indicates the optimal alignment of the DoF for phase shifts equal to (a) 0 degrees, (b) 45 degrees and (c) 90 degrees

suspension is completely dependent on the design, some general remarks can be made to assess the validity of this simplification for the SDoF and MDoF systems. For any resonant generator to operate efficiently the resonance frequency of the suspension must match the frequency of the target ambient vibration. For smaller devices this means that the suspension must have a very low stiffness, due to the smaller masses. For instance to obtain a resonance frequency of 2 Hz for a device mass of 40 g a stiffness of 6.3 N m^{-1} is required.

Fulfilling these requirements in a minimal volume can be achieved by a compliant design, where flexures facilitate the stiffness. The stiffness of these flexures can be found from the Euler - Bernoulli beam theory.

$$k = \frac{Ebh^3}{4L^3}, \quad (21)$$

Examples of suspension designs for a SDoF are a planar system with two parallel flexures [57] and an out of plane system with a cantilever beam [58] as shown in Fig. 7a and b, respectively. In both cases, only a small portion of the design space is required for the suspension which justifies the assumption of a zero volume claim suspension. A MDoF suspension can be obtained by combining multiple SDoF systems in series. In this particular case, the base of the cantilever can be placed within the planar system, creating a 2 DoF generator that can harvest from both in-plane and out-of-plane vibrations without sacrificing a large portion of the volume for the suspension.

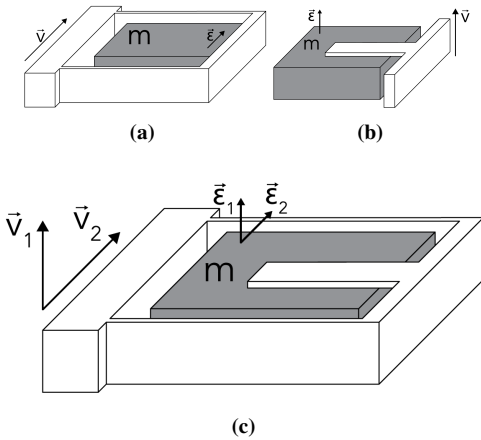


Fig. 7: Proposed designs for the suspension for 1 DoF energy harvesting system; Planar system with parallel flexures (a) and out of plane system with a cantilever beam (b). Combining these designs can result in a 2 DoF system (c). Choosing the right flexure dimensions these suspensions can facilitate the stiffness required for a 2 Hz resonance frequency.

D. Other applications of orientation and MDoF strategies

In the design metric presented in this paper the strategies of orientation and MDoF strategies are assessed for the power density of a VDRG. However, also CDRGs and CFIGs may benefit from these strategies in terms of power density. For example, a bistable generator may overcome a higher potential barrier when a higher accelerations is achieved by combining multiple vibration directions, resulting in more power output. Furthermore, apart from an increased power density, other motivations can be found for employing these strategies such as insensitivity to the direction of vibrations [9], increased robustness [59] and a wider bandwidth [35].

E. Evaluation of prior art

In a previous study by Smilek et al. (2015) [54] a SDoF harvester was developed to harvest from human walking motion for a design space with equal dimensions in both the vibration directions ($p_v = 1$). The 2 cm^3 device was able to harvest up to $225 \mu\text{W}$. Assuming the vibration data presented in this research, a 2DoF device of the same dimensions is expected to harvest about equal power. Therefore, selecting the simpler SDoF design is a good choice.

Another situation occurs when the cantilever based designs, such as shown in Fig. 7 are evaluated. Since these designs generally involve long and slender cantilever beams they commonly have high values for p_l . Therefore, inefficient designs can be obtained very easily according to the metric presented in this paper. In these situations, it may be beneficial for the designer to design a MDoF system, or look into other options for the suspension.

Zhao et al. (2016) [20] present a harvester that uses the MDoF strategy to harvest from human walking motion. The 12.8 cm^3 cylindrical harvester with relative dimensions of $p_v = .57$ was estimated to harvest in the order of magnitude of $100 \mu\text{W}$. Again, assuming the vibration data

presented in this research, it can be seen that in this case the MDoF strategy resulted in an inefficient system. In both cases a better power density could be obtained if the design metric presented in this research was applied.

F. Powering a hearing aid

The results show that in the first considered design space scenario a maximum of 10 mW can be harvested during walking. Therefore, to power a 1 mW hearing aid for 16 hours a day, the person has to walk for 1.6 hours every day under the assumption that the remaining energy can be stored.

V. CONCLUSION

Vibration energy harvesting from human motion can be used as a sustainable power source for biomedical sensors. Despite these recent advances there is still a lack of in-depth knowledge on what strategies the designer should use to obtain maximum power density when harvesting from multi-directional motion sources.

Therefore, this research has presented a novel design metric by which the designer can classify a 2D situation by evaluating two dimensionless parameters: the relative vibration power, p_v , and the relative design space dimensions, p_l . It was shown that the RPD of a 2DoF system compared to a SDoF system only depends on the product $p^* = p_v p_l$, and has a maximum of 1.185 for $p^* = 1$. Moreover, designers can use this metric and corresponding flowchart to identify and quantify the situations where 2DoF systems are expected to outperform SDoF systems in terms of power density, and as a result design the proper system for their particular case.

A case study on the vibrations in the area of the human head while walking is conducted and the application of powering a hearing aid for children is investigated. Classically, only the direction with the largest vibration power is harvested, effectively wasting the energy of

ambient vibrations in orthogonal directions. In this research it was found that vibrations in both CC and AP can be harvested and their relative power was found to be $p_v \approx .55$. Three cases of p_l are assessed for a 10 cm³ generator and three different optimal embodiments can be found. It was found that in the considered situation where $p^* = 1.1$, a 2DoF systems may provide up to 16% more output power compared to a SDoF system.

REFERENCES

- [1] CB Williams and Rob B Yates. Analysis of a micro-electric generator for microsystems. *sensors and actuators A: Physical*, 52(1):8–11, 1996.
- [2] WHO. Deafness and hearing loss, 2015.
- [3] Paul D Mitcheson, Tim C Green, Eric M Yeatman, and Andrew S Holmes. Architectures for vibration-driven micropower generators. *Journal of microelectromechanical systems*, 13(3):429–440, 2004.
- [4] Erich Goll, Hans-Peter Zenner, and Ernst Dalhoff. Upper bounds for energy harvesting in the region of the human head. *IEEE transactions on bio-medical engineering*, 58(11):3097, 2011.
- [5] Phonak AG. Phonak sky v, product information, 2016.
- [6] Elizabeth K Reilly, Lindsay M Miller, Romy Fain, and Paul Wright. A study of ambient vibrations for piezoelectric energy conversion. *Proc. PowerMEMS 2009*, pages 312–315, 2009.
- [7] Ryoichi Tashiro, Nobuyuki Kabei, Kunimasa Katayama, Yoshizo Ishizuka, Fuminori Tsuboi, and Kiichi Tsuchiya. Development of an electrostatic generator that harnesses the motion of a living body. use of a resonant phenomenon. *JSME International Journal Series C Mechanical Systems, Machine Elements and Manufacturing*, 43(4):916–922, 2000.
- [8] Shad Roundy, Paul K Wright, and Jan Rabaey. A study of low level vibrations as a power source for wireless sensor nodes. *Computer communications*, 26(11):1131–1144, 2003.
- [9] Jin Yang, Xihai Yue, Yumei Wen, Ping Li, Qiangmo Yu, and Xiaoling Bai. Design and analysis of a 2d broadband vibration energy harvester for wireless sensors. *Sensors and Actuators A: Physical*, 205:47–52, 2013.
- [10] Ethem Erkan Aktakka and Khalil Najafi. Three-axis piezoelectric vibration energy harvester. In *2015 28th IEEE International Conference on Micro Electro Mechanical Systems (MEMS)*, pages 1141–1144. IEEE, 2015.
- [11] Manuel Gutierrez, Amir Shahidi, David Berdy, and Dimitrios Peroulis. Design and characterization of a low frequency 2-dimensional magnetic levitation kinetic energy harvester. *Sensors and Actuators A: Physical*, 236:1–10, 2015.
- [12] Chiao-Fang Hung, Tien-Kan Chung, Po-Chen Yeh, Chin-Chung Chen, Chieh-Min Wang, and Shin-Hung Lin. A miniature mechanical-piezoelectric-configured three-axis vibrational energy harvester. *IEEE Sensors Journal*, 15(10):5601–5615, 2015.

- [13] Huicong Liu, Bo Woon Soon, Nan Wang, CJ Tay, Chenggen Quan, and Chengkuo Lee. Feasibility study of a 3d vibration-driven electromagnetic mems energy harvester with multiple vibration modes. *Journal of Micromechanics and Microengineering*, 22(12):125020, 2012.
- [14] Jong C Park and Jae Y Park. Asymmetric pzt bimorph cantilever for multi-dimensional ambient vibration harvesting. *Ceramics International*, 39:S653–S657, 2013.
- [15] Ravi Teja Purra Reddy, Xingguo Xiong, and Junling Hu. Design and analysis of three dof piezoelectric vibration energy harvester. In *2015 COMSOL Conference*, 2015.
- [16] Hao Wu, Lihua Tang, Yaowen Yang, and Chee Kiong Soh. Feasibility study of multi-directional vibration energy harvesting with a frame harvester. In *SPIE Smart Structures and Materials+ Nondestructive Evaluation and Health Monitoring*, pages 905703–905703. International Society for Optics and Photonics, 2014.
- [17] J Xu and J Tang. Multi-directional energy harvesting by piezoelectric cantilever-pendulum with internal resonance. *Applied Physics Letters*, 107(21):213902, 2015.
- [18] Yaowen Yang, Hao Wu, and Chee Kiong Soh. Experiment and modeling of a two-dimensional piezoelectric energy harvester. *Smart Materials and Structures*, 24(12):125011, 2015.
- [19] Zhengbao Yang and Jean Zu. Toward harvesting vibration energy from multiple directions by a nonlinear compressive-mode piezoelectric transducer. *IEEE/ASME Transactions on Mechatronics*, 21(3):1787–1791, 2016.
- [20] Nian Zhao, Jin Yang, Qiangmo Yu, Jiangxin Zhao, Jun Liu, Yumei Wen, and Ping Li. Three-dimensional piezoelectric vibration energy harvester using spiral-shaped beam with triple operating frequencies. *Review of Scientific Instruments*, 87(1):015003, 2016.
- [21] Shengxi Zhou, Weijia Chen, Mohammad H Malakooti, Junyi Cao, and Daniel J Inman. Design and modeling of a flexible longitudinal zigzag structure for enhanced vibration energy harvesting. *Journal of Intelligent Material Systems and Structures*, page 1045389X16645862, 2016.
- [22] U Bartsch, J Gaspar, and O Paul. Low-frequency two-dimensional resonators for vibrational micro energy harvesting. *Journal of Micromechanics and Microengineering*, 20(3):035016, 2010.
- [23] Andrea Crovetto, Fei Wang, and Ole Hansen. An electret-based energy harvesting device with a wafer-level fabrication process. *Journal of Micromechanics and Microengineering*, 23(11):114010, 2013.
- [24] Anthony G Fowler, SO Reza Moheimani, and Sam Behrens. An omnidirectional mems ultrasonic energy harvester for implanted devices. *Journal of Microelectromechanical Systems*, 23(6):1454–1462, 2014.
- [25] Anthony G Fowler, SO Reza Moheimani, and Sam Behrens. Design and characterization of a 2-dof mems ultrasonic energy harvester with triangular electrostatic electrodes. *IEEE Electron Device Letters*, 34(11):1421–1423, 2013.
- [26] Jacopo Iannacci, Guido Sordo, Massimo Gottardi, Thomas Kuenzig, Gabriele Schrag, and Gerhard Wachutka. An energy harvester concept for electrostatic conversion manufactured in mems surface micromachining technology. In *Semiconductor Conference Dresden-Grenoble (ISCDG), 2013 International*, pages 1–4. IEEE, 2013.
- [27] V Janicek and M Husak. Designing the 3d electrostatic microgenerator. *Journal of Electrostatics*, 71(3):214–219, 2013.
- [28] Sehwan Kim and Kukjin Chun. 2d vibration based mems energy harvester. In *Int. Conf. on Renewable Energies and Power Quality*, 2012.
- [29] Ulrich Mescheder, Antwi Nimo, Bernhard Müller, and Awad Saad Abou Elkeir. Micro harvester using isotropic charging of electrets deposited on vertical sidewalls for conversion of 3d vibrational energy. *Microsystem technologies*, 18(7-8):931–943, 2012.
- [30] A Mahmood Paracha, P Basset, D Galayko, A Dudka, F Marty, and T Bourouina. Mems dc/dc converter for 1d and 2d vibration-to-electricity power conversion. In *TRANSDUCERS 2009-2009 International Solid-State Sensors, Actuators and Microsystems Conference*, pages 2098–2101. IEEE, 2009.
- [31] Kai Tao, Shuwei Liu, Sun Woh Lye, Jianmin Miao, and Xiao Hu. A three-dimensional electret-based micro power generator for low-level ambient vibrational energy harvesting. *Journal of Micromechanics and Microengineering*, 24(6):065022, 2014.
- [32] K Tao, SW Lye, N Wang, X Hu, and JM Miao. A sandwich-structured mems electret power generator for multi-directional vibration energy harvesting. In *2015 Transducers-2015 18th International Conference on Solid-State Sensors, Actuators and Microsystems (TRANSDUCERS)*, pages 51–54. IEEE, 2015.
- [33] Kai Tao, Jianmin Miao, Sun Woh Lye, and Xiao Hu. Sandwich-structured two-dimensional mems electret power generator for low-level ambient vibrational energy harvesting. *Sensors and Actuators A: Physical*, 228:95–103, 2015.
- [34] Bin Yang, Chengkuo Lee, Rama Krishna Kotlanka, Jin Xie, and Siak Piang Lim. A mems rotary comb mechanism for harvesting the kinetic energy of planar vibrations. *Journal of Micromechanics and Microengineering*, 20(6):065017, 2010.
- [35] Yong Zhu, SO Moheimani, and MR Yuce. A 2-dof wideband electrostatic transducer for energy harvesting and implantable applications. In *Sensors, 2009 IEEE*, pages 1542–1545. IEEE, 2009.
- [36] Yong Zhu, SO Reza Moheimani, and Mehmet Rasit Yuce. A 2-dof mems ultrasonic energy harvester. *IEEE Sensors journal*, 11(1):155–161, 2011.
- [37] Shad Roundy, Eli S Leland, Jessy Baker, Eric Carleton, Elizabeth Reilly, Elaine Lai, Brian Otis, Jan M Rabaey, Paul K Wright, and V Sundararajan. Improving power output for vibration-based energy scavengers. *IEEE Pervasive computing*, 4(1):28–36, 2005.
- [38] B Andò, S Baglio, F Maiorca, and C Trigona. Analysis of two dimensional, wide-band, bistable vibration energy harvester. *Sensors and Actuators A: Physical*, 202:176–182, 2013.
- [39] Salar Chamanian, Reza Pakdaman Zangabad, Payam Zarbakhsh, Manouchehr Bahrami, and Mohamad Khodaei. Wideband capacitive energy harvester based on mechanical frequency-up conversion. In *Sensors Applications Symposium (SAS), 2012 IEEE*, pages 1–4. IEEE, 2012.

- [40] Xiudong Tang and Lei Zuo. Enhanced vibration energy harvesting using dual-mass systems. *Journal of sound and vibration*, 330(21):5199–5209, 2011.
- [41] J Lin, JX Zhu, M Sonje, Y Chang, ZC Feng, and M Almasri. Two-cavity mems variable capacitor for power harvesting. *Journal of Micromechanics and Microengineering*, 22(6):065003, 2012.
- [42] R Munnig Schmidt, Georg Schitter, and Adrian Rankers. *The Design of High Performance Mechatronics-: High-Tech Functionality by Multidisciplinary System Integration*. IOS Press, 2014.
- [43] Matthew AD Brodie, Tim R Beijer, Colleen G Canning, and Stephen R Lord. Head and pelvis stride-to-stride oscillations in gait: validation and interpretation of measurements from wearable accelerometers. *Physiological measurement*, 36(5):857, 2015.
- [44] Justin Kavanagh, Rod Barrett, and Steven Morrison. The role of the neck and trunk in facilitating head stability during walking. *Experimental brain research*, 172(4):454–463, 2006.
- [45] Justin J Kavanagh, RS Barrett, and Steven Morrison. Upper body accelerations during walking in healthy young and elderly men. *Gait & posture*, 20(3):291–298, 2004.
- [46] Mark D Latt, Hylton B Menz, Victor S Fung, and Stephen R Lord. Walking speed, cadence and step length are selected to optimize the stability of head and pelvis accelerations. *Experimental Brain Research*, 184(2):201–209, 2008.
- [47] Mark D Latt, Hylton B Menz, Victor S Fung, and Stephen R Lord. Acceleration patterns of the head and pelvis during gait in older people with parkinson’s disease: a comparison of fallers and nonfallers. *The Journals of Gerontology Series A: Biological Sciences and Medical Sciences*, page glp009, 2009.
- [48] Claudia Mazzà, Marco Iosa, Pietro Picerno, and Aurelio Cappozzo. Gender differences in the control of the upper body accelerations during level walking. *Gait & posture*, 29(2):300–303, 2009.
- [49] Claudia Mazzà, Mounir Zok, and Aurelio Cappozzo. Head stabilization in children of both genders during level walking. *Gait & posture*, 31(4):429–432, 2010.
- [50] Hylton B Menz, Stephen R Lord, and Richard C Fitzpatrick. Acceleration patterns of the head and pelvis when walking on level and irregular surfaces. *Gait & posture*, 18(1):35–46, 2003.
- [51] Steven Morrison, Daniel M Russell, Kyle Kelleran, and Martha L Walker. Bracing of the trunk and neck has a differential effect on head control during gait. *Journal of neurophysiology*, 114(3):1773–1783, 2015.
- [52] Edwar Romero, Robert O Warrington, and Michael R Neuman. Powering biomedical devices with body motion. In *2010 Annual International Conference of the IEEE Engineering in Medicine and Biology*, pages 3747–3750. IEEE, 2010.
- [53] Aurora Summa, Giuseppe Vannozi, Elena Bergamini, Marco Iosa, Daniela Morelli, and Aurelio Cappozzo. Multilevel upper body movement control during gait in children with cerebral palsy. *PLoS one*, 11(3):e0151792, 2016.
- [54] Jan Smilek and Zdenek Hadas. A study of kinetic energy harvesting for biomedical application in the head area. *Microsystem Technologies*, pages 1–13, 2015.
- [55] Hamish G MacDougall and Steven T Moore. Marching to the beat of the same drummer: the spontaneous tempo of human locomotion. *Journal of applied physiology*, 99(3):1164–1173, 2005.
- [56] JJ Kavanagh, Steven Morrison, and RS Barrett. Coordination of head and trunk accelerations during walking. *European journal of applied physiology*, 94(4):468–475, 2005.
- [57] Reinier Alberda. Parameter study of velocity-damped vibration energy harvesters, 2017.
- [58] Shad Roundy and Paul K Wright. A piezoelectric vibration based generator for wireless electronics. *Smart Materials and structures*, 13(5):1131, 2004.
- [59] Shad Roundy, Paul K Wright, and Kristofer SJ Pister. Micro-electrostatic vibration-to-electricity converters. In *ASME 2002 International Mechanical Engineering Congress and Exposition*, pages 487–496. American Society of Mechanical Engineers, 2002.

Chapter 3

Mechanical analysis and design process

Thijs BLAD

"Everything is theoretically impossible, until it is done."

Robert A. Heinlein

In this chapter, a mechanical analysis of the vibration energy harvester is presented based on three functions. The case study of a miniaturized generator for human motion is considered, and the relevant design considerations for the parts fulfilling the functions are discussed. The parts were integrated in a system concept called the parametric frequency up-converter generator (PFupCG).

3.1 Introduction

Ultimately, vibration energy harvesters are devices that convert mechanical energy of a driving vibration to an electrical output power. The intermediate steps in this process, however, may be realized in many different ways. For instance, two examples of energy harvesters from literature are the electromechanical resonant generator and the shoe-mounted piezoelectric devices shown in Fig. 3.1. These generators use completely different ways to facilitate the energy harvesting process, but both end up generating electrical energy from a mechanical vibration.

In this chapter, a detailed mechanical analysis of the energy harvesting process will be presented. The approach for this analysis is based on the energy flow through the generator. The points where this energy flow is manipulated will be identified as the functions of the energy harvester system. The solution space of possibilities to fulfill these functions will be categorized as a system of strategies and sub-strategies. From this classification a strategy will be chosen based on the boundary conditions of the case study.

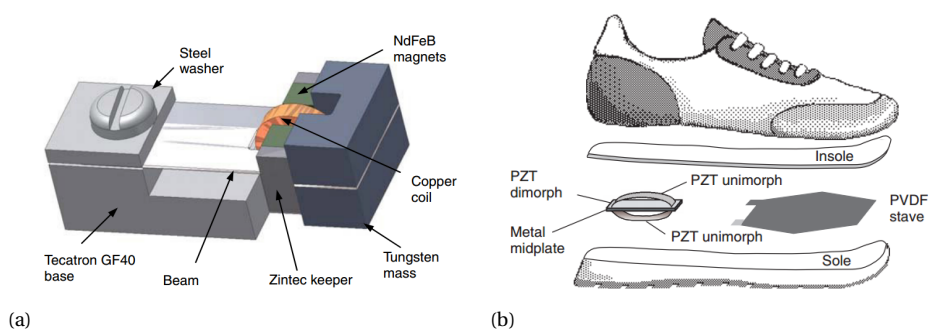


Figure 3.1: Examples of vibration energy harvesters from literature; (a) micro electromechanical resonant generator [9], (b) piezoelectric patches in shoe sole [10].

3.2 Mechanical analysis of the vibration energy harvester

The working principle of a vibration energy harvester can be described by analyzing the energy flow through the device. In this method, the energy flow can be pictured as a block diagram where the blocks resemble manipulations of the energy flow. For example, the electromechanical resonant generator of Fig. 3.1 uses the inertial effects of a mass to obtain relative motion within the device (kinetic energy) from the driving vibration. As a result, the device begins to resonate, a process where the energy is constantly exchanged between kinetic and elastic energy. This process acts as a storage of energy within the device, where energy is added due to the vibration, and extracted due to the transducer. The magnet and coil transducer executes the last part in the energy flow: the transduction from kinetic energy to electrical energy. In the shoe mounted generator a

piece of piezoelectric material is deformed (elastic energy) due to the driving vibration. Electrical energy is generated from the time varying deformation as a result of the *piezoelectric effect*.

Although these generators are vastly different, they exhibit similarities in their energy flow and points at which this flow is manipulated. These similarities can be generalized, and by doing so the energy flow model shown in Fig. 3.2 was constructed. This block scheme model consists of three blocks and can be used to describe the energy flow through an arbitrary vibration energy harvester. In this model an arrow represents an energy flow and a block represents a manipulation of the energy flow. In all cases of vibration energy harvesters, energy enters the system from the vibration source and leaves the system as either electrical output power or losses. In this model, the manipulations of every infinitesimal amount of energy in the total energy flow are lumped in three manipulations.

The first manipulation occurs when energy is extracted from the vibration source (i.e. energy from the vibration enters the system). Once inside the system the energy is manipulated for a second time, which can be understood as the transmission of energy to the transducer inside the system. Finally, in the third manipulation the energy is the transduction process where energy leaves the system. These three manipulations of energy can be seen as the functions of the vibration energy harvester. Therefore, three functions are identified and numbered F1, F2 and F3 and named *transfer*, *transmit* and *transduce*, respectively.

F1: Transfer of energy from the vibration source *in to the system*.

F2: Transmit energy *inside the system*.

F3: Transduce energy *out of the system* to useful output power.

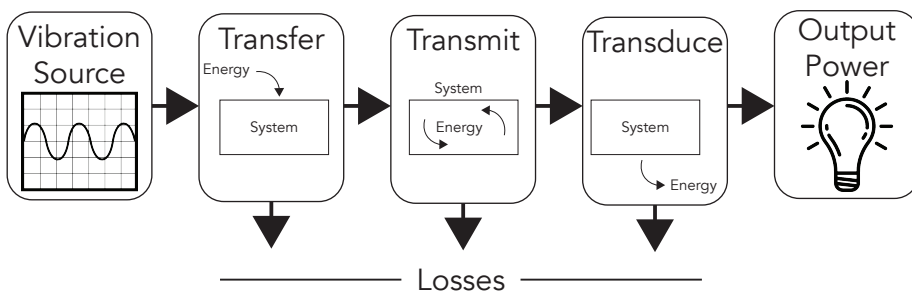


Figure 3.2: Energy flow model of the vibration energy harvester.

3.2.1 Transfer

The first block in the energy flow model governs the extraction of energy from the driving vibration to induce relative motion within the generator. In general, the energy that goes into the system as a result of this block can always be calculated using the force-distance integral.

$$W = \int \vec{F} d\vec{s} \quad (3.1)$$

Where $d\vec{s}$ is the relative motion within the system, and \vec{F} is the force that acts on the point where relative motion is induced. The relative motion can be obtained by directly driving one point of the system and fixing another (*direct-force generators*), or by driving the entire system and using inertial forces to obtain relative motion (*inertial generators*). In the direct-force generators, the relative motion is equal to the amplitude of the vibration and the force results from the deformation of the material between the attachment points. In the inertial generators the force that is generated depends on the mass of the inertial element, m , and the acceleration of the driving vibration. Assuming that the driving vibration can be expressed as $y = Y_0 \sin(\omega t)$ where Y_0 is the amplitude and ω is the frequency, the acceleration can be found by deriving twice.

$$\ddot{y} = Y_0 \omega^2 \sin(\omega t) \quad (3.2)$$

The relative motion of the inertial generator can be found by solving the differential equation corresponding to the physical system. This process will be demonstrated using the mass-spring-damper model of Fig. 3.3. In this model, the energy harvester consists of a proof mass, m , and a housing that are connected by a spring, k , and a viscous damper, c , in parallel. The relative motion of the device, $z = x - y$, is found by subtracting the motion of the housing, y , from the motion of the proof-mass, x .

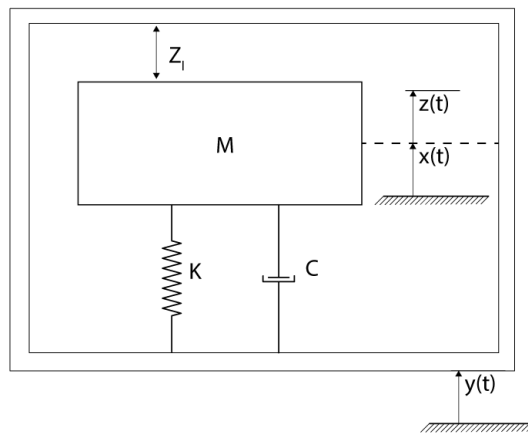


Figure 3.3: Mass-spring-damper model of the vibration energy harvester

The differential equation for the motion of the mass with respect to the frame is given by the following equation. This equation is normalized by substituting $\omega_n = \sqrt{\frac{k}{m}}$ and $\zeta = \frac{c}{2m\omega_n}$. These variables are the natural frequency and the damping factor, respectively.

$$\ddot{z}(t) + 2\zeta\omega_n\dot{z}(t) + \omega_n^2 z(t) = Y_0\omega^2 \sin(\omega t). \quad (3.3)$$

By using the Laplace transform, the transfer function from the base motion, $Y(s)$ to the relative motion, $\mathcal{Z}(s)$, is found.

$$\frac{\mathcal{Z}(s)}{Y(s)} = \frac{-s^2}{s^2 + 2\zeta\omega_n s + \omega_n^2} \quad (3.4)$$

The amplitude, $Z_0 = Y_0 \left| \frac{\mathcal{Z}(i\omega)}{Y(i\omega)} \right|$, and the phase shift, $\phi = \angle \frac{\mathcal{Z}(i\omega)}{Y(i\omega)}$, of the relative motion can be found from the magnitude and the phase of the transfer function at $s = i\omega$. In Fig. 3.4 a magnitude plot is shown for a number of transfer functions with various levels of ζ .

$$z(t) = Z_0 \sin(\omega t + \phi) \quad (3.5)$$

From the figure can be seen that the relative motion is greatly dependent on the frequency of the driving vibration. When the frequency of the driving motion approaches the natural frequency of the generator the relative motion is amplified as a result of resonance. Generators that aim to utilize the resonance phenomenon are the *resonant generators*. The non-resonant *parametric generators* do not use this phenomenon. The energy that is supplied to the inertial generator over a period, T , as a result of the driving vibration is given by the following equation.

$$dW = m\dot{y}dz$$

$$W = \int_{-\frac{T}{2}}^{\frac{T}{2}} m \left[-\omega^2 Y_0 \sin(\omega t) \right] \left[\omega Z_0 \cos(\omega t + \phi) \right] dt \quad (3.6)$$

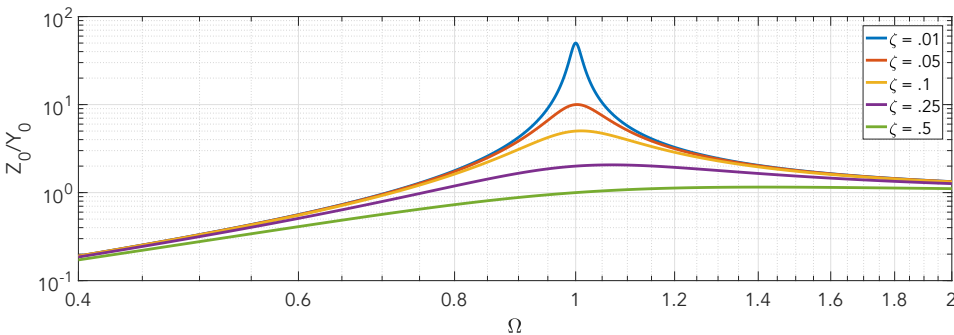


Figure 3.4: Magnitude plot of transfer function for various damping ratios.

3.2.2 Transmit

The second block in the energy flow model governs the transmission of energy within the system. The input of this block is the energy contained in the relative motion of the system, and the output of this block is the energy flowing to the transducer. The solution space for this function can be split in two categories: the *coupled generators* and the *non-coupled generators*. The non-coupled generators have their transducers connected directly to the part of the system where relative motion is induced by the driving vibration, such as the case in the mass-spring-damper system of Fig. 3.3. The coupled generators are characterized by a coupling which separates the transduce function from the transfer function. In these types of devices, energy must be transmitted from the parts where relative motion is induced to the parts where the transduction mechanisms are located.

One key aspect of the coupled generators is that they allow for a strategy called *frequency up-conversion* (FupC). In this strategy a low-frequency input motion is converted in a high-frequency output motion. The key benefit of the high-frequency motion is that the amplitude is much smaller compared to the low-frequency motion, which makes efficient transduction much simpler [11].

3.2.3 Transduce

The final block in the energy flow model is the transduction process that converts mechanical energy in the device to electrical output power. The three most commonly used transduction processes are the electromechanical, piezoelectric and electrostatic processes. A concise analysis that captures the most important fundamental aspects of those processes will be presented, but for a more elaborate analysis the reader is referred to the accompanying sources. The electromechanical transduction process is governed by Faraday's law, which states that the generated voltage of is proportional to the rate of change in the magnetic flux. Typically, a permanent magnet and coil are used in this transducer such that the voltage is proportional to the relative velocity between the magnet and the coil [12, 13]. The induced voltage, V , and the damping force, F , are therefore given by the following equations, where l is the average length of the winding, N the number of windings and R the resistance of the coil.

$$V = NlB\dot{z} \quad (3.7)$$

$$F = \frac{(NlB)^2}{R} \dot{z} \quad (3.8)$$

The electrostatic transduction process has two different modes of operation: Constant charge mode, where the relative motion changes the distance between two parallel plates and constant voltage mode, where the relative motion changes the area of overlap between the parallel plates. The latter mode is most commonly used in miniaturized generators and known as the comb drive. The following set of equations governs this mode, [14, 15] where Q is the charge difference on the capacitor plates, ϵ the permittivity of the medium between the plates, l the overlap length and w the gap between the plates.

$$V = \frac{lQ}{\epsilon wz} \quad (3.9)$$

$$F = \frac{-lQ^2}{2\epsilon wz^2} \quad (3.10)$$

The electromechanical coupling of the piezoelectric material can be described by the two constitutive equations for linear piezoelectric material [16]. The equations Eq. 3.11 and Eq. 3.12 are known as the piezoelectric actuator and sensor equations, respectively. Where S is mechanical strain, T applied stress, E electric field, D electric displacement, S^E the matrix of elasticity under conditions of constant electric field, d piezoelectric coefficient matrix, ϵ^T permittivity matrix at constant mechanical strain.

$$S = S^E T + D_t E \quad (3.11)$$

$$D = d_t T + \epsilon^T E \quad (3.12)$$

3.2.4 Categorization of solution space by strategies

As demonstrated by the two examples, the functions of an energy harvester can be fulfilled in different ways. In Table 3.1 a categorization of the solution space is presented where the generators are categorized in types and sub-types in accordance with the previous analysis. Furthermore, an objective is formulated for every group, to indicate the most important aspects of every strategy. This categorization is not unique, and many other categorizations can be found. However, the presented case was proposed because it demonstrates an intuitive grouping of approaches from a mechanical perspective. Effort was made to make sure the categorization is complete (i.e. no solutions can exist outside the groups) and may contain relevant embodiments in every group. The following strategies and sub-strategies were found per function.

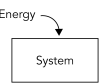
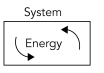
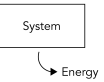
| Function | Strategy | Sub-strategy |
|--|---|--|
| I: Transfer  | Ia. Direct-force Ib. Inertial | Ib1. Resonant Ib2. Parametric |
| II: Transmit  | IIa. Non-coupled IIb. Coupled | IIb1. Frequency up-converters IIb2. Non-frequency up-converters |
| III. Transduce  | IIIa. Electromechanical IIIb. Piezoelectric IIIc. Electrostatic IIId. Other transduction mechanism | |

Table 3.1: Classification of vibration energy harvesters based on the strategies and sub strategies used to fulfill the transfer, transmit and transduce functions.

3.3 Design problem formulation

Before a selection can be made of the appropriate generator type and employed strategies, the boundary conditions of the design problem should be assessed. The presented case study has two main boundary conditions that must be considered in the mechanical design. Firstly, the vibration environment of human motion features large amplitudes and low frequencies. From the results of the literature search for human motion can be found that human walking motion measured in the head area could be simulated by a 2 Hz vibration with an amplitude of 25 mm, which corresponds to an acceleration of 0.4g.

$$y(t) = 25 \times 10^{-3} \sin(2 \cdot 2\pi t) \quad (3.13)$$

Secondly, the application of the vibration energy harvester introduces a set of constraints on the dimensions and weight of the device. The applications aspired in the case study are miniaturized biomedical devices such as sensors, pacemakers and hearing aids, which should be as small as possible to fulfill their functions with minimal user discomfort. Therefore, an energy harvester for such an application should not dramatically increase the dimensions or weight of the system. An order of magnitude of cm^3 is projected as the upper limit for the volume of the energy harvester, and therefore a maximum internal displacement limit of $Z_l = 5 \text{ mm}$ is used.

Lastly, boundary conditions are introduced by the transducer. The most important boundary condition is the upper limit for the amount of damping that can be generated. Considering the viscous damper model, this means the damping coefficient is limited by the transduction process and the dimensions of the transducer. Other boundary conditions can be introduced by using materials such as piezoceramics that are very brittle and prone to failure under tensile stresses. Combining all these boundary conditions formulates the design problem that is faced in this case study.

"Efficiently harvest energy from a large amplitude low-frequency motion, using a small device with limited damping."

Quantified:

"Efficiently harvest energy from a 25 mm, 2 Hz motion, using a device with a stroke of 5 mm and limited ($\zeta \ll 1$) damping."

3.3.1 Strategy selection

The strategies classified in Table 3.1 can be evaluated using the boundary conditions identified in the previous section. For the first function the inertial generators require only one attachment point to a moving structure, where the direct force strategy require two. As a result, they allow for more flexibility and greater degree of miniaturization [5] and are therefore selected as the preferred strategy. The selected sub-strategy is the parametric generators, since resonant amplification of internal motion is simply impossible when the dimensions of the device are smaller than the amplitude of the driving motion.

For the second function the coupled generators are favored over the uncoupled generators because they allow for the frequency up-conversion sub-strategy. Frequency up-conversion is favored over coupled generators because the high-frequency vibration can be harvested much more efficiently by a transducer with limited damping capabilities, due to the decrease in amplitude [11, 17, 18]. Therefore, frequency up-conversion is selected to fulfill the transmit function.

Of all the commonly used transduction processes, piezoelectricity is considered to be the most promising transduction process for miniaturized vibration energy harvesting devices. The main reasons for this are the large power densities, ease of application and miniaturization capabilities [8, 15]. For example, the fabrication of micro-scale electromechanical generators requires planar micro-coils and deposited magnetic films, which have a reduced efficiency compared to wound coils and bulk magnets [19]. Moreover, electrostatic transducers require a voltage to be maintained across the electrodes, which provides a practical problem [20]. Therefore, the piezoelectric strategy is selected to fulfill the transduce function.

3.4 Mechanical design

The working principle of a frequency up-converter (FupC) can be divided in three parts. The first part is the suspension of the low-frequency oscillator (LFO), that generates relative motion from the inertial forces induced by the low-frequency driving motion. The second part is the high-frequency oscillator (HFO) and the transducer, which generates the output power of the device. The last part is the coupling that facilitates the FupC behavior. An example of a FupC system is shown in Fig. 3.5.

In this chapter, the mechanical design of the functional parts of the FupC will be discussed. First, the functional requirements of the parts will be identified. Next, concepts will be generated for every part and analyzed to assess their performance. Finally, the concept solutions will be integrated in a conceptual design.

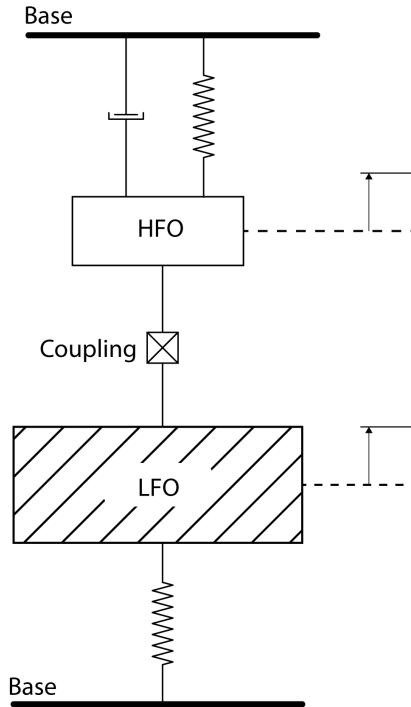


Figure 3.5: Schematic representation and components of a coupled generator where the frequency up-conversion strategy is applied.

3.4.1 Coupling

The coupling is the part that fulfills the transmit function of the energy harvester. Upon excitation, the relative motion of the LFO is must be converted by the coupling to a high-frequency vibration in the HFO.

FR 1 The coupling must allow relative motion of the LFO.

FR 2 The coupling must convert the low-frequency motion of the LFO to a high-frequency motion in the HFO.

The FupC coupling can be realized using three different types of couplings: Impact, Stick or Transmission. In impact type couplings, kinetic energy is exchanged between two mechanical elements upon contact in a short amount of time and can be seen as a very stiff compression spring connecting the two mechanical elements during the time of contact. Stick type couplings are a temporarily connection between two mechanical elements. During the time of connection, strain energy builds up in an elastic element until a force or displacement threshold is reached, and the connection is broken. Lastly,

the transmission type couplings are a permanent connection between the mechanical elements and couple their motions into a single DoF.

Since the motion of the driving vibration is larger than the internal displacement limit, the motion of the LFO must be restricted. This can be done by adding a lot of mechanical damping or by a choosing a stiffer suspension, but that would result in a large loss of energy, or a very inefficient execution of the transfer function. The other option is to restrict the movement of the LFO by a mechanical stop. The mechanical stop can at the same time function as an impact type coupling by using the impact energy of the LFO to excite the HFO. This intuitive combination of functions led to the selection of the impact type coupling.

With the impact type coupling, the two most feasible¹ embodiments are shown in Fig. 3.6. The coupling could be placed between the HFO and the LFO, such that upon impact kinetic energy is transferred from the LFO to the HFO [21–24]. Alternatively, the coupling could be placed between the LFO and the base, such that upon impact the position of the LFO is fixed and the HFO continues to oscillate in its natural frequency [25, 26]. The latter embodiment is preferred because there is no risk of a secondary impact between the LFO and the HFO that could result in a reduced power output.

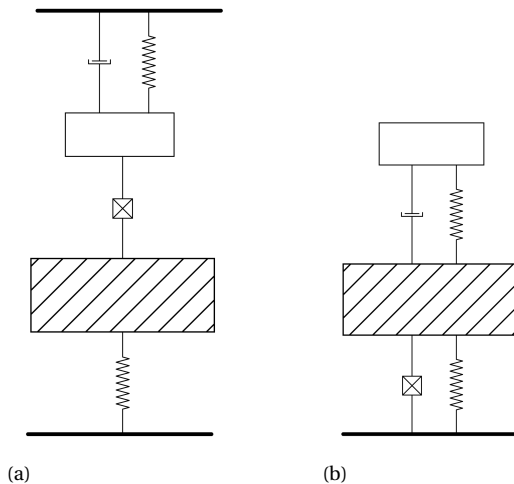


Figure 3.6: **Two possible embodiments for a FupC generator with an impact type coupling.**

The last design choice w.r.t. the coupling is the method at which the displacement constraint of the mechanical stops are enforced. It was chosen to do this with by changing the load case of a flexible element from bending to tension (much like straightening a rope) instead of using collision of two bodies against each other. The intuitive reasoning for this is that collision is expected to have negative effects on the robustness by intro-

¹A more detailed explanation and categorization of all the FupC embodiments are presented in the next chapter.

ducing wear and friction. Another advantage of this method is that it can be integrated as another functional requirement of the suspension. Due to this integration, the mechanical design of the coupling is found in the suspension subsection. Concluding, a flowchart of the design choices of the transmit function is presented in Fig. 3.7.

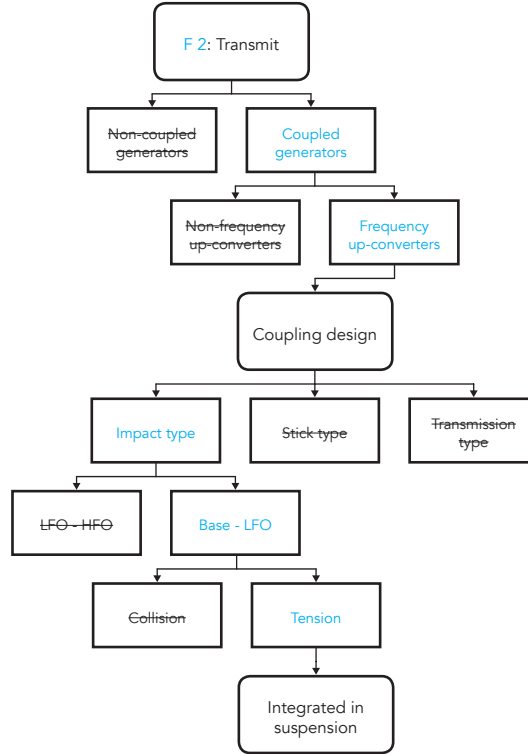


Figure 3.7: Flowchart indicating the design choices made in for the transmit function and the coupling design.

3.4.2 Suspension

The suspension is the part that connects the LFO to base of the device. Upon excitation, the suspension is responsible for execution of the transfer function of the generator. Since the boundary conditions of the case study prescribe relatively low accelerations and relatively small masses, the suspension must have a low stiffness to allow relative motion upon excitation. On the other hand, the suspension must carry the weight of the system and must therefore be strong enough to cope with gravity. The maximum displacement limit is also prescribed by the boundary conditions at 5 mm, and the impact type coupling must be integrated in the suspension. In conclusion, the following functional requirements are identified for the suspension.

FR 1 The suspension must allow relative motion between the base and the LFO under excitation of a (2 Hz, 25 mm) vibration.

FR 2 The suspension has a maximum relative displacement of 5 mm.

FR 3 The suspension must be able to carry the mass of the device.

FR 4 A impact type coupling must be integrated in the suspension.

It is desirable to maximize the impact of the LFO on the mechanical stop since this energy directly used in the FupC coupling. Therefore, the stiffness of the suspension must be tuned such that the work done by the vibration, as given by Eq. 3.6, is maximized. To find the optimal value for the stiffness, the model of Fig. 3.8 is evaluated for different stiffness values while recording the maximum impact velocity. The model is excited by the target excitation of 2 Hz, 25 mm and has a displacement limit of 5 mm.

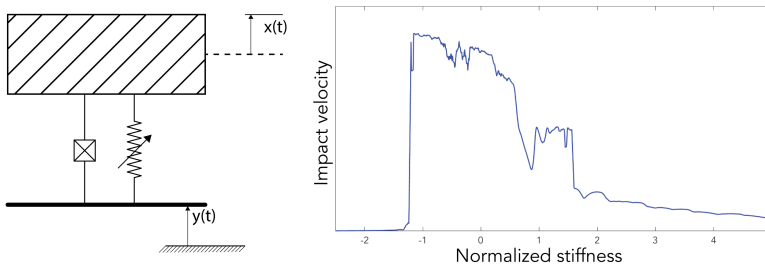


Figure 3.8: **Model and results of the suspension stiffness analysis.**

Numerical evaluation with MATLAB's ode45 of the differential equation corresponding to the model resulted in the plot on the right of the figure. It can be seen that when normalizing the stiffness value to $K = K^* \frac{Ma}{Z_l}$, the highest impact velocity is obtained for $K^* \approx -1$. This result can be explained by realizing that the internal displacement limit of the generator is much smaller than the amplitude of the driving vibration. Therefore, the LFO may reach the mechanical stop at the stroke limit before the sinusoidal acceleration profile reaches its maximum point. As a result, only a fraction of the available energy is extracted from the vibration. The negative stiffness prevents movement of the LFO until the inertial force becomes greater than the spring force. By tuning this stiffness such that this happens exactly at maximum acceleration, it can be ensured that maximum energy is collected from the vibration. Therefore, a stiffness should be chosen according to the following expression, where β is a factor smaller than 1 that can be used to ensure motion at every cycle.

$$K = -\beta \frac{aM}{Z_l} \quad (3.14)$$

The desired stiffness profile results in a bi-stable system with stable positions located at the mechanical stops at $z = Z_l$ and $z = -Z_l$. Such a bi-stable system can be created using magnets or exclusively mechanical elements [27]. It was chosen to exclude concepts

using magnets because this imposes limitations for fabrication at a miniaturized scale [28]. An additional advantage of the mechanical bi-stability is that the mechanical stops can be integrated in a single part. The field of compliant mechanisms is investigated for concepts of bi-stable systems. Compared to the alternative rigid-link mechanisms they offer inherent advantages w.r.t. miniaturization, friction and backlash [29, 30] and are therefore very suitable options. The feasible embodiments in the field of compliant mechanisms can either be beam based, or plate based. Of those two groups the beam-based embodiments are preferred because they can be constructed in a 2D design, while the plate-based embodiments requires a 3D design. Moreover, the inertial forces in this case study will be relatively low, and therefore a beam-based suspension with the appropriate force-deflection characteristic would require significantly less space compared to a much stiffer plate-based suspension of equal thickness. This resulted in the three beam-based embodiments shown in Fig. 3.9. These embodiments will be called the post-buckled beam, the bridge and the pre-curved beam.

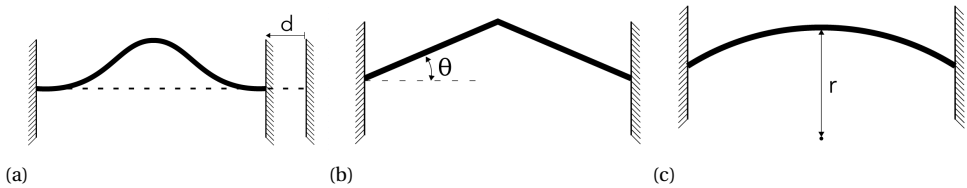


Figure 3.9: Three feasible embodiments for a bi-stable suspension: post-buckled beam (a) bridge (b) pre-curved beam (c).

It was attempted to model the force-deflection profiles of these embodiments using an approach based on the pseudo-rigid-body-model [29]. A detailed description of this work is given in Appendix E. Although this led to interesting results, the models were over-simplified and could not be accurately generalized. The force-deflection profiles of these embodiments are analyzed using ANSYS. For all embodiments, over-span lengths of 70 mm, widths of $b = 5$ mm, thicknesses of $t = 0.05$ mm were used. The beams were designed such that they had a stable equilibrium at a center point displacement of $z = 5$ mm. For the bridge embodiment, this resulted in an angle of $\theta = 8.13$ deg and for the pre-curved embodiment this resulted in a curvature radius of $r = 125$ mm. For the post-buckled bridge, the center-point offset can be estimated at $d = 0.44$ mm using the following formula. Where w_0 is the center-point offset; l is the original length of the bridge and d the clamped length of the bridge [31].

$$w_0 = 2 \frac{\sqrt{(l-d)d}}{\pi} \quad (3.15)$$

The central point was first moved slightly upwards from the equilibrium such that a tensile load case arises, and the force-displacement characteristic at this mechanical stop point could be analyzed. Next, the center point is moved downwards over a displacement of $2Z_l = 10$ mm to evaluate the force-displacement characteristic over the range of motion. The results of this analysis are shown in Fig. 3.10.

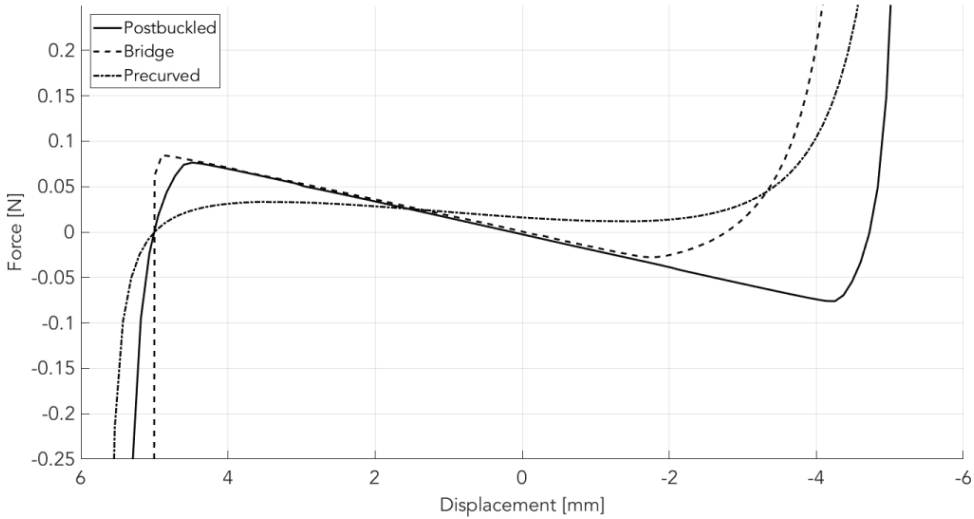


Figure 3.10: Force-deflection analysis of the three beam-based suspension embodiments.

From the figure, the following conclusions can be drawn. Firstly, it can be observed that an asymmetric force-deflection behavior is obtained for the bridge and pre-curved embodiments, this is undesired because it prevents the LFO snapping back at maximum acceleration. This results in a lower impact velocity and thus less energy generated. Moreover, this resulted in a second stable position placed much closer to the instable equilibrium at $z = 0$ for the bridge, and no second stable position for the pre-curved beams. Secondly, it can be seen that the stiffnesses over the linear range are different. The post-buckled and bridge embodiments have almost equal negative stiffnesses of -18.1 N m^{-1} and -17.8 N m^{-1} , respectively. The pre-curved beam has a much lower negative stiffness of -6.1 N m^{-1} . A lower linear stiffness is favorable because it reduces the required over-span length. Thirdly, it can be noted that the mechanical stop behavior is different for all embodiments. The pre-curved beam has a rather soft mechanical stop as the force slowly increases when pushing the center point beyond its stable equilibrium. The mechanical stop of the post-buckled beam is stiffer, but still allows a fair bit of motion after passing the equilibrium. The stiffest mechanical stop is found for the bridge embodiment. This result can be explained by identifying that there is some room for bending in the post-buckled and pre-curved embodiments that will be exploited first, before the much stiffer tensile load case is forced. A stiff mechanical stop is desirable as this increases the impulse generated upon impact.

In order to overcome the problems regarding asymmetry of the bridge and pre-curved beam, these embodiments must be paired with an equal counterpart mirrored horizontally with a gap of $2Z_l = 10 \text{ mm}$ between their central points at their stable equilibrium positions shown in Fig. 3.11.

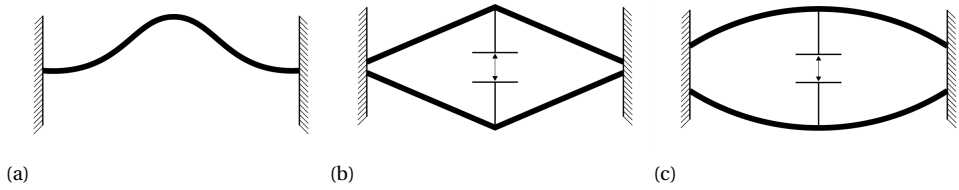


Figure 3.11: Post-buckled beam and symmetric versions of the other two embodiments.

3

These central points can now be connected such that a symmetric bistable device is formed with an internal displacement limit of $Z_l = 5$ mm. An added benefit of this method is that the angle of the bridge, θ , and the radius of the pre-curved beam, r , are no longer necessary to enforce the displacement limit and therefore become tuning parameters of the device. With these parameters the trade-off between the linear stiffness (lower is better) and the mechanical stop stiffness (higher is better) can be tuned which offers advantages in terms of flexibility over the post-buckled beam. Furthermore, manufacturing is simpler because the assembly takes place in the direction of motion, where the forces are much lower compared to the axial directions. Lastly, the doubled embodiments facilitate a guiding with increased robustness. This does not only aid towards FR 3, but also greatly reduces parasitic rotations. The resulting force-deflection behavior can be seen in Fig. 3.12 for a selected bridge angle of $\theta = 10$ deg and for the pre-curved embodiment this resulted in a curvature radius of $r = 120$ mm.

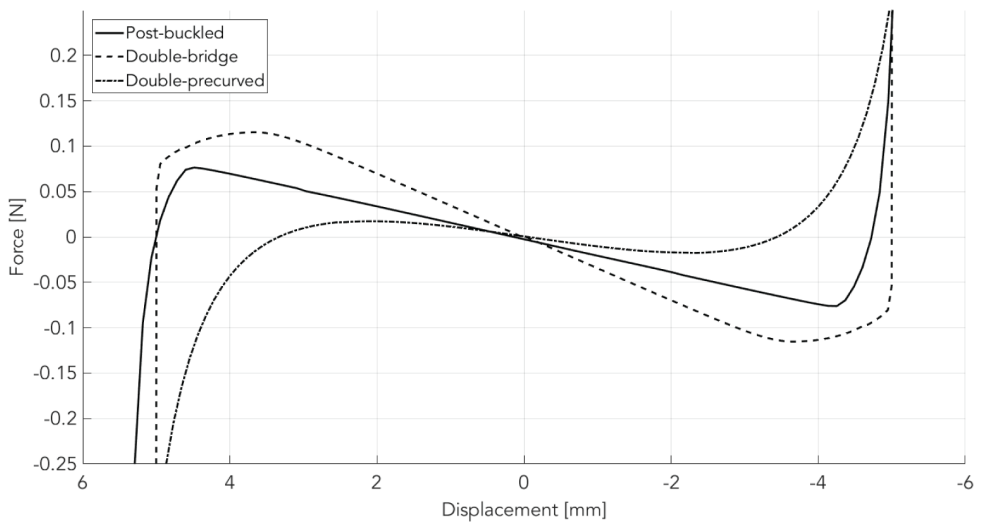


Figure 3.12: Force-deflection analysis of the three post-buckled embodiment and the symmetric versions of the other two embodiments.

The three concepts were ranked regarding their performances on linear stiffness, control over the positioning of stable positions, mechanical stop stiffness, manufacturability, and robustness. The results of this ranking are shown in Table 3.2.


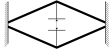
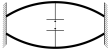
| |  |  |  |
|--------------------------------------|---|---|--|
| Linear stiffness | + | - | ++ |
| Control over stable positions | + | ++ | -- |
| Mechanical stop stiffness | +/- | ++ | -- |
| Manufacturing | - | + | + |
| Robustness | - | + | + |

Table 3.2: Ranking of the concepts for the suspension.

Based on the ranking of the concepts, it was chosen to use the double-bridge concept for the suspension. Concluding, a flowchart is presented in Fig. 3.13 that summarizes all the design choices that were made during the design of the transfer function and suspension.

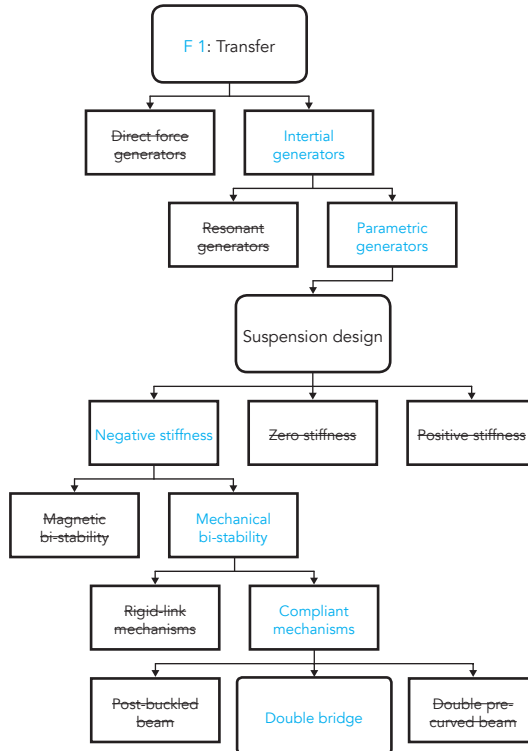


Figure 3.13: Flowchart summarizing all the design choices made for the transfer function and the suspension with the integrated impact type coupling.

3.4.3 High-frequency oscillator

The HFO is the part that oscillates with an increased frequency fulfills the transduce function of the energy harvester. In this part, the mechanical energy must be transduced into electrical output power.

FR 1 The HFO must be excited by the impact coupling and oscillate with an increased frequency.

FR 2 The oscillations of the HFO must be damped out by a transducer, generating electrical power.

For the mechanical design of the oscillator itself the three concepts shown in Fig. 3.14 were generated from the field of compliant mechanisms and will be called the cantilever, double flexure and intermediate body.

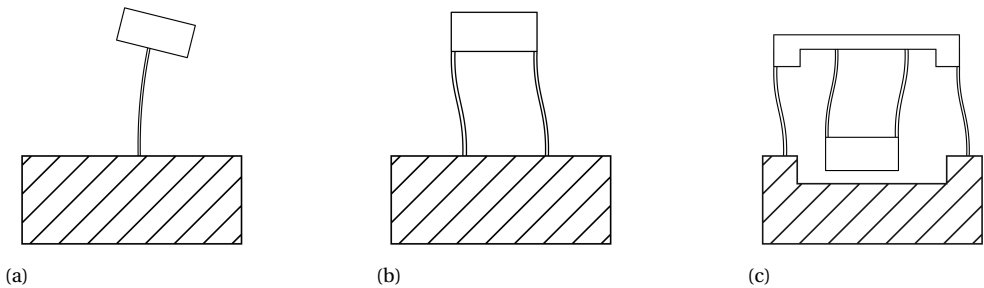


Figure 3.14: **Three concepts for the high frequency oscillator.**

Differences between these concepts are the stiffnesses and the robustness w.r.t. reaction forces and parasitic motions. If all flexures are assumed to have a stiffness K , the cantilever and intermediate body concept have a total stiffness of K , while the double flexure concept has a total stiffness of $2K$. A lower stiffness is preferred as this enables a greater degree of miniaturization while achieving the same resonance frequency. In terms of robustness both the cantilever concept and the double flexure concept induce a reaction moment on the LFO as a result of their motion. The reaction moment of the intermediate body concept can be limited by placing the HFO inside the LFO such that it is in line with the flexures that connect the LFO to the intermediate body such as shown in Fig. 3.14c. The higher robustness is preferred, as the reaction moment is transferred to the relatively compliant flexures that support the LFO. Furthermore, it should be considered that the intermediate body concept may change the dynamics by the adding of the additional inertial body, and these should therefore be examined carefully. The design choice was made to select the intermediate body concept because the robustness was deemed the most important characteristic.

The transducer consists of a piezoelectric element mounted on the flexures suspending the HFO. For this purpose, the concepts shown in Fig. 3.15 were identified as possible candidates. These concepts are the out-of-plane cantilever, the in-plane cantilever [32, 33] and the cantilever with interdigitated electrodes [34].

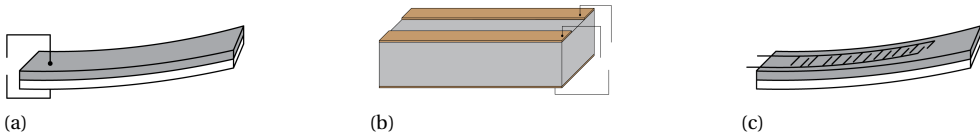


Figure 3.15: Three concepts for the piezoelectric transducer element.

The main differences between the concepts are their mode of operation, their DoF and their manufacturability. Both the in-plane and out-of plane cantilevers work in the '31-mode', where the generated voltage is perpendicular to the applied stress. The cantilever with interdigitated electrodes utilizes the '33-mode', where the direction of generated voltage is equal to the direction of the applied stress. Generally, the piezoelectric coefficient is higher for the '33-mode', but stress can be more easily induced in systems using the '31-mode'. The DoF of the in-plane cantilever makes this system unfit for application on flexures with a large width but small thickness, as this would result in relatively low transducer area and a high spacing between the electrodes compared to the other concepts. However, if the width of the flexure approaches its thickness, as is often the case in micro-fabricated devices, this concept can be an attractive option. Because the electrodes are placed on the top and bottom instead of the sides, this concept allows much easier micro-fabrication. Based on this reasoning, prototyping methods were explored for this concept in Appendix A. For the macro-scale prototype, the mechanical design of the suspension was the main research topic, and therefore it was chosen to build the transducer using the out-of-plane cantilever because of its simplicity.

Combining these two choices resulted in the transducer concept shown in Fig. 3.16. The transducer assembly consists of the flexure, two layers of electrodes and a layer of piezoelectric material. In the middle of the assembly, the top electrode is removed over the width of the transducer. The whole assembly is clamped between the base and a clamp through bolts. Because the HFO is connected to the intermediate body by two parallel flexures, the transducer assembly behaves as a fixed-guided beam. As a result of the HFO motion, compressive strains are induced in one half of the piezoelectric material and tensile strains in the other half. Therefore, opposite charges are induced on the topside electrodes with respect to the bottom side electrode. Because the electrodes are not separated on the bottom side this effectively creates a series arrangement of the piezoelectric transducer with itself.

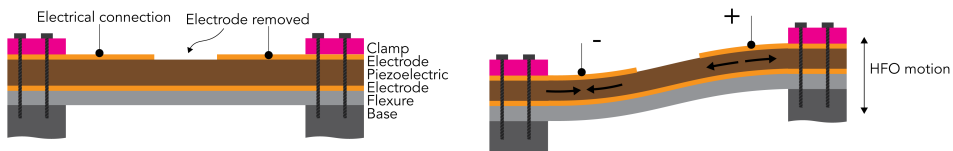


Figure 3.16: Components (a) and working principle (b) of the piezoelectric transducer mounted between the intermediate body and the HFO.

Concluding, a flowchart summarizing the design choices that were made during the design of the transduce function and the HFO and the resulting concept are presented in Fig. 3.17.

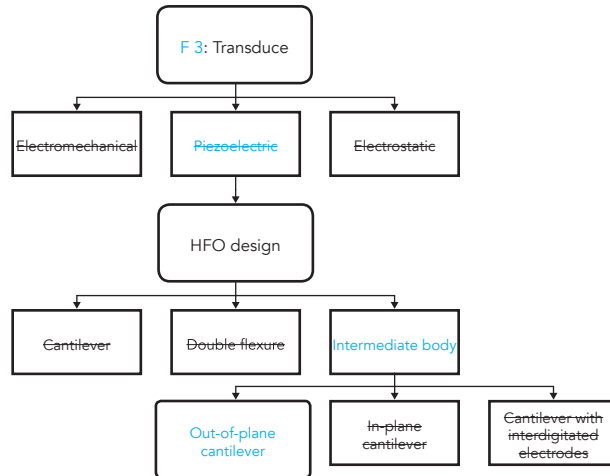


Figure 3.17: Flowchart summarizing all the design choices made for the transduce function.

3.5 Integration

The parts discussed in the previous section were integrated in and a prototype energy harvester called the parametric frequency up-converter generator (PFupCG) was developed. The PFupCG concept is specifically designed for the type of motion where the amplitude of the driving motion is larger than the internal displacement limit of the generator. Therefore, the stroke limit of the generator, Z_l , was selected to be 5 mm. Compared to the 25 mm amplitude of the target driving vibration, this results in a device with a Q -factor of 0.2 for the target operation conditions. A rendering of the PFupCG prototype is shown in Fig. 3.18.

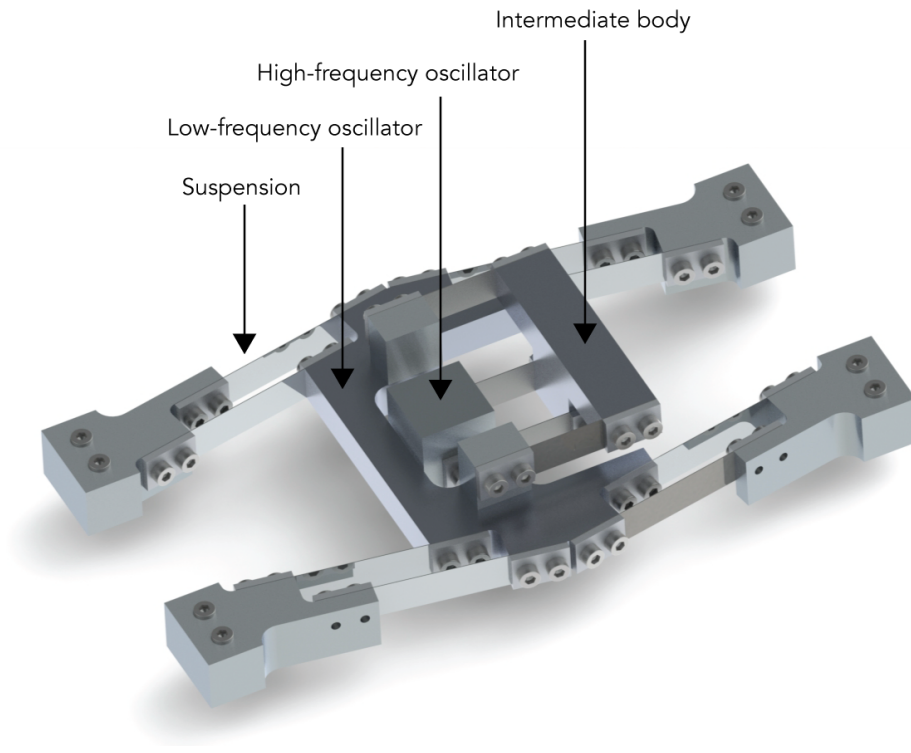


Figure 3.18: Render of the piezoelectric PFupCG for human motion.

A dynamic model and corresponding set of differential equations was constructed to model the behavior of the total system. This model, the design parameters and the performance is discussed in the next chapter. Additionally, a prototype and experimental setup were manufactured to experimentally validate the modeled behavior. The manufacturing of the final and intermediate prototypes is discussed in appendix C, and the results of the experiment are discussed in the next chapter.

3.6 Conclusions

Three functions of a vibration energy harvesting system can be identified: **Transfer** of energy from the vibration source in to the system, **Transmit** energy inside the system and **Transduce** energy out of the system to useful output power. The solution space of those functions was categorized and led to the classification of strategies and sub-strategies in Table 3.1. The design problem formulated for the case study of human motion was to "Efficiently harvest energy from a 25 mm, 2 Hz motion, using a device with a stroke of 5 mm and limited ($\zeta \ll 1$) damping.". For this case study, the piezoelectric, parametric, and frequency up-conversion strategies were chosen, which resulted in the mechanical design of three parts: the coupling, the suspension of the low-frequency oscillator (LFO) and the high-frequency oscillator (HFO). The most important design choices during this process are summarized next.

In the mechanical design of the coupling it was chosen for the design of an impact type coupling between the base and the LFO because the coupling function intuitively combines with the mechanical stop function for the LFO motion. A tension loaded embodiment was selected because it allows for integrated in the suspension, and is more robust to wear and friction compared to a collision embodiment. In the design of the suspension it was chosen to design a system with a negative stiffness, because this resulted in the highest impact velocity between the base and the LFO, and therefore the highest impact energy transmitted to the HFO. The bi-stability was obtained using a double-bridge embodiment from the domain of compliant mechanisms because it exhibited the stiffest mechanical stop behavior, the pre-loading could be added relatively easy, was robust to reaction moments and had excellent control over the position of the stable positions. The HFO was designed with an intermediate body, due to its robustness to parasitic motions, and good stiffness characteristic. For the transducer, a out-of-plane cantilever embodiment was chosen because of its simplicity, but an other option was explored and prototyped in Appendix A.

Ultimately, the functions were integrated in a vibration energy harvester system concept called the parametric frequency up-converter generator (PFupCG). The new PFupCG concept is expected to outperform existing vibration energy harvesters for the given case study. In the next section, the modeling, prototyping and results will be discussed.

Chapter 4

The Parametric frequency up-converter generator

Thijs BLAD

*"The walls between art and engineering exist only in our minds,
and few go beyond them."*

Theo Jansen

In this paper, the theoretical framework, modeling, design and experiment of the parametric frequency up-converter generator concept are presented in the form of a research article. Simulation of the model with a Q-factor of 0.2 for the vibration conditions of the case study showed that the PFupCG can have a significantly higher power output compared to the classical models when the scaling problem of the damping is considered in the analysis. Moreover, the dynamical properties of the PFupCG were validated using a prototype and experiment.

Originally appeared as: "Towards the Design of a Miniaturized Frequency Up-converter for Energy Harvesting from Human Motion" by T.W.A. Blad, D. Farhadi Machekposhti, J.L. Herder and N. Tolou which is awaiting submission. The article was reformatted to fit the style of the thesis.

Towards the Design of a Miniaturized Frequency Up-converter for Energy Harvesting from Human Motion

T.W.A. Blad, D. Farhadi Machekposhti, J.L. Herder, and N. Tolou

4

Abstract—This work presents a novel design, model and prototype of a vibration energy harvester based on frequency up-conversion by impact. The general theoretical framework of frequency up-conversion methods is discussed and a new classification of those methods is proposed. This led to the development of a new embodiment of a frequency up-converter based on impact: the Parametric Frequency up-converter Generator (PFupCG). The PFupCG was designed to harvest energy under conditions where the amplitude of the driving motion is larger than the internal displacement limit. A suspension was developed for the PFupCG based on compliant mechanisms that combines a bi-stable behavior with a strong stiffening effect at the desired displacement limits. This resulted in a prototype of the PFupCG with a Q -factor of 0.2. A case study was carried out where the PFupCG was analyzed by simulation and experiment for vibration conditions similar to human motion (2 Hz, 25 mm).

Index Terms—Vibration energy harvesting, Human motion, Frequency up-conversion, Impact, Low-frequency, Low Q -factor, Compliant mechanisms, Bi-stable.

I. INTRODUCTION

VIBRATION energy harvesting has been investigated for over 20 years since the early work of Williams and Yates in 1996 [1] which investigated the piezoelectric, electromagnetic, and electrostatic transduction mechanisms for the purpose of vibration-to-electric energy conversion. Devices that incorporating such a transduction mechanisms are called vibration energy harvesters (VEH) and have received much interest as they may provide an alternative to batteries in powering microelectronic devices such as wireless

sensor networks. Moreover, using miniaturized VEHs to power biomedical devices such as hearing aids or pacemakers would offer significant advantages such as reduced costs and/or risks over replacing the batteries and therefore makes these applications excellent candidates. These body worn applications could collect their energy from human motion, analogue to the kinetic wristwatches.

Although there is a wealth of energy available in human motion, is not a particularly pleasant vibration source for a VEH to collect power from. The frequencies are extremely low (< 10 Hz), and often inconsistent. Furthermore the amplitudes of the motions are large (> 10 mm) and rarely follow specified paths with a single degree of freedom (DoF). The ultimate goal of designing efficient VEHs at the scale of microelectronics that harvest from human motion is therefore an incredibly difficult challenge.

Nevertheless, great advances have been made towards this goal in prior art. Three general theoretical models for VEHs were constructed and analyzed thoroughly, which offered great insights in their performances under various operation conditions [2], [3]. Simulations of those models with real human motion data was done in [4] and contributed to further clarification of the challenges. A prototype of an electromagnetic generator with the size of an AA battery was developed in [5]. The device was attached to the upper arm where it could generate an average power of 4.96 mW from a person running at 8 km h^{-1} . The

magnetic levitation harvester developed in [6] was tested on 10 subjects running 9.6 km h^{-1} and resulted in an average output of $342 \mu\text{W}$. In [7], a micro-electromagnetic VEH consists of a magnetic ball rolling through a tube wrapped by a coil was constructed. The power output was measured during three common activities at various locations on the body, and a maximum of $445 \mu\text{W}$ was observed. Also piezoelectric VEHs were developed such as the generator with a rotating proof mass demonstrated by [8] and tested in a real world environment during a running race. It was shown that for frequencies from $0.5 - 4 \text{ Hz}$ power outputs in the range of tens of micro watts were achieved. Another device where the impact of a metal ball excited a PZT cantilever could generate up to $175 \mu\text{W}$ when excited by a vibration of 4.96 Hz with an acceleration of 2 g [9].

However, the established generalized models are limited because they only consider a single DoF and are built from only mass, spring, damper and coulomb friction elements. The works cited earlier, and many other VEHs harvesting from human motion utilize different strategies such as impact on mechanical stops or the latching and release of magnets, and are often multi-DoF systems that cannot be described by those general models. Naturally, models have been constructed for some of those embodiments, but are rarely generalized to describe the strategy as a whole. This makes it difficult to judge and compare the performances of different strategies.

The research objective of this work is to propose a classification of the strategies that can be used to harvest energy from human motion. From this classification a strategy will be chosen for which a general model will be constructed, and a case study will be conducted where a device is designed, fabricated and tested for vibration that resemble human motion.

Section II will present the background and scaling problem and introduce the fundamental

problems of harvesting from human motion with a miniaturized device. In section III, a classification of strategies for harvesting from human motion will be proposed and a general model will be constructed for the Frequency up-conversion strategy. Section IV discusses the case study of harvesting from human motion and presents the design, fabrication and testing of a new embodiment with a suspension based on compliant mechanisms. The results of this experiment are presented in section V and discussed in section VI. Lastly, the conclusions will be summarized in section VII.

II. BACKGROUND AND SCALING PROBLEM

Most reported literature on energy harvesters consider systems where the dimensions of the generator are much larger than the amplitude of the driving motion. Therefore, these systems allow themselves to be designed as resonant systems which is a beneficial mode of operation. When the dimensions of the generator approach, or shrink below the amplitude of the driving motion, however, efficiencies for those types of generators are decreased dramatically [3], [10]. A summary of the background and the problem analysis of energy harvesting in those situations, often encountered at low-frequencies, is addressed here. For this purpose, the Velocity-damped-resonant-generator (VDRG) is introduced.

A. The velocity-damped resonant generator

The simple mechanical model developed by Mitcheson [2] can be used to analyze the behavior of a typical energy harvester and is shown in Fig. 1. In this model, the energy harvester consists of a proof mass, M , and a housing that are connected by a spring, K , and a viscous damper, C , in parallel. The driving motion is modeled as a harmonic displacement of $y = Y_0 \sin(\omega t)$. The relative motion of the device, $z = x - y$, is found by subtracting the motion of the housing, y , from the motion of the proof-mass, x .

The differential equation for the motion of the mass with respect to the frame is given by the Eq. 1. This equation is normalized by

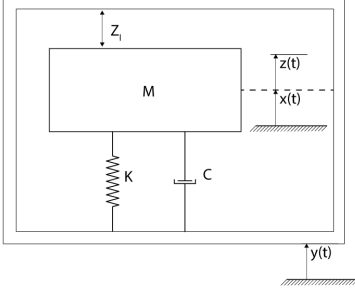


Fig. 1: Generic model of the VDRG.

4

substituting $\omega_n = \sqrt{\frac{K}{M}}$ and $\zeta = \frac{C}{2M\omega_n}$. These variables are the natural frequency and the damping factor, respectively.

$$\ddot{z}(t) + 2\zeta\omega_n\dot{z}(t) + \omega_n^2z(t) = Y_0\omega^2 \sin(\omega t). \quad (1)$$

In this model, the transducer characteristics are modeled by the dissipation of energy in a viscous damper which issues a damping force proportional to the velocity times a coefficient, C . This method is often used to provide a good approximation for the electromagnetic and to some extent piezoelectric transducers. The damper always exerts a force against the direction of motion equal to $F_d = -C\dot{z}$. Therefore, the damper always does negative work on the system, as a result of the transduction process. The power, P , is equal to the force-distance integral over a full cycle of period T .

$$P = -\frac{1}{T}C \int_{-\frac{T}{2}}^{\frac{T}{2}} \dot{z}^2 dt. \quad (2)$$

Combining Eq. 1 and 2, and following the thorough analysis finds a statement for the maximum power output of the generator [2]. This power reaches its maximum at resonance and is limited by the internal displacement limit, Z_l . Assuming an optimal damping ratio, the following statement is obtained.

$$P = \frac{1}{2}\omega^3 MY_0 Z_l \quad (3)$$

Since no parasitic losses are considered in this analysis, it provides an upper limit for the power output of the resonant generator. In

reality, mechanical damping may contribute to the total damping coefficient such that $C = C_m + C_e$, where C_m is the mechanical damping coefficient and C_e the electrical damping coefficient from the transducer. As a result, the output power of the system may be considerably lower than indicated by Eq. 3.

To make a fair comparison between different types, shapes and sizes of generators a very useful metric was introduced in [2]. The *volume figure of merit* (FoM_v) compares the useful power output of a generator to the power output of an imaginary, optimal generator of the same volume, V , driven by the same vibration. As a baseline, the proof-mass of this optimal generator is assumed to be made from gold such that the following expression is obtained.

$$\text{FoM}_v = \frac{\text{Useful power output}}{\frac{1}{2}Y_0\rho_{\text{Au}}V^{\frac{1}{3}}\omega^3} \quad (4)$$

Sometimes, it is useful to account for the bandwidth when identifying the performance of a generator. For this purpose, a modified version of the FoM_v, called the bandwidth figure of merit FoM_{BW} was proposed in [3].

$$\text{FoM}_{\text{BW}} = \text{FoM}_v \frac{\text{BW}_{3\text{dB}}}{\omega} \quad (5)$$

B. Scaling problem

From Eq. 3 can be seen that the Q -factor ($Q = \frac{Z_l}{Y_0}$) is directly proportional to the power output of the device under optimal damping conditions at resonance. Therefore, it is desirable to design generators with a high Q -factor. However, there are two practical properties that limit the Q -factor. Firstly, the internal displacement limit, Z_l is limited by the dimensions of the device for obvious reasons. As a result, the desire to miniaturize generators to the micro-scale with dimensions of typically 1–100 μm is inevitably linked to a lower Q -factor. Secondly, the amplitude of the driving vibration, Y_0 , is inversely proportional to the frequency squared when keeping a constant acceleration, i.e. $Y_0 \propto \frac{1}{\omega^2}$. In conclusion, miniaturized generators harvesting

from low-frequency vibrations are destined to operate with small Q -factors. Here, a generator will be considered "miniaturized" when it is operating with a $Q < 1$. Therefore, not the absolute dimensions of the generator, but its stroke relative to the amplitude of the driving vibration is considered.

When considering Eq. 3 as the denominator of 4 there is no obvious indication of a reduced efficiency of miniaturized generators. Moreover, when considering a length scale, l , both the numerator and the denominator scale with $\propto l^4$. However, the problem with miniaturized generators is that the optimal damping factor considered in Eq. 3 scales with $\propto \frac{2}{Q}$ and becomes greater than 1. In practice, this damping has to be supplied by the transducer, which relies on physical processes and their embodiments and are limited in the damping they can provide [11]. Moreover, most generators reported to date have a $\zeta < 1$, which is incompatible with the miniaturized definition used here. Therefore, new strategies are required to design efficient miniaturized generators.

III. CLASSIFICATION OF FREQUENCY UP-CONVERSION STRATEGIES

To address the low Q -factor problem outlined in the previous section, different approaches have been attempted in prior art. Many of these approaches use the strategy of *frequency up-conversion* (FupC) as first described in [12], to couple a driving vibration with a low-frequency to an oscillator with a higher frequency, and therefore a higher Q -factor. In this work, a classification of these FupC systems is proposed based on their coupling, and generalized mechanical diagrams are identified for each type. An example of such a mechanical diagram is shown in Fig. 2. In all cases, the FupC systems consist of the following parts: a low-frequency oscillator (LFO) that generates relative motion from the inertial forces induced by the low-frequency driving motion, a high-frequency oscillator (HFO) connected to a dissipative element where energy is transduced into output electrical power, a stationary base and the

coupling that facilitates the FupC behavior.

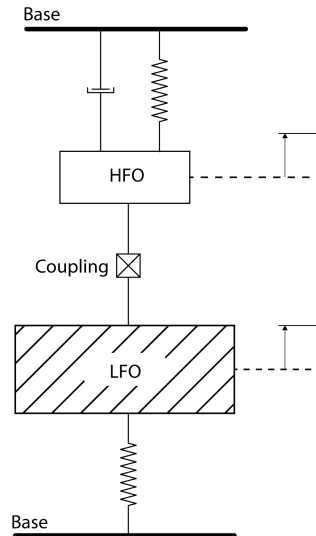


Fig. 2: Example of a mechanical diagram of a frequency up-converter;

The proposed classification is shown in Table 3 and makes a distinction between where the coupling is located in a system. Three possible locations for the coupling are between the base and the LFO, between the base and the HFO and between the LFO and the HFO. Next, the FupC generators are classified based on the type of coupling that is used. The three types of couplings that lead to FupC behavior are impact type, stick type and transmission type couplings. In impact type couplings, kinetic energy is exchanged between two mechanical elements upon contact in a short amount of time and can be seen as a very stiff compression spring connecting the two mechanical elements during the time of contact. Impact type couplings can be divided in two groups: the direct group and indirect group. In couplings of the direct group the two mechanical elements make direct contact upon impact. In the indirect group, contact is between one of the elements and an intermediate body which is connected to the second element. Stick type couplings are a temporary connection between two

mechanical elements. During the time of connection, strain energy builds up in an elastic element until a force or displacement threshold is reached, and the connection is broken. The stick type couplings are divided in groups of mechanical and non-mechanical stick couplings. Mechanical stick couplings deflect an elastic element due to contact forces, and non-mechanical stick couplings use non-mechanical forces such as magnetic attraction. Lastly, the transmission type couplings are a permanent connection between the mechanical elements and couple their motions into a single DoF. Transmissions can be between two translational elements or between translational and rotational elements.

Not all types of couplings are feasible at every location, and therefore there are only 11 combinations of coupling locations and types shown in the table. Transmission type couplings would not function when connected to the base because the base does not allow any motion. Moreover, direct impact between the base and HFO would greatly restrict HFO motion and stick type between the base and LFO would essentially make the LFO the HFO. Naturally, combining different types of couplings, adding more oscillators and/or degrees of freedom an infinite amount of options can be obtained. It was chosen to omit those compounded systems because they would become increasingly complex and most likely infeasible for practical applications. In prior art, the coupling was often placed between the LFO and the HFO. In this work, a general model is developed where the coupling is placed between the base and the LFO. Moreover, a prototype is designed and tested.

IV. METHODS

To address the problem outlined in the previous section, the *Parametric Frequency up-Conversion Generator* (PFupCG), shown in Fig. 4, is proposed. The PFupCG is classified as a Base-LFO direct impact-type (Ia1) generator using the classification introduced in the previous section. Moreover, the PFupCG

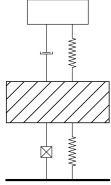
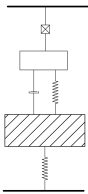
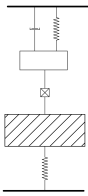
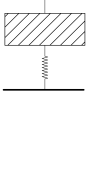
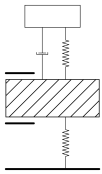
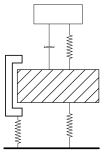
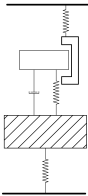
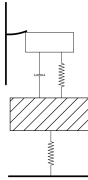
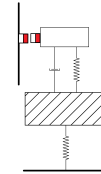
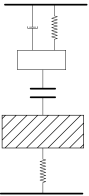
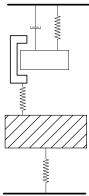
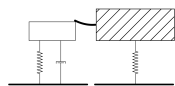
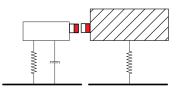
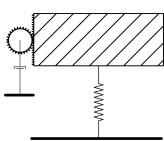
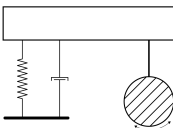
is a non-resonant generator designed to harvest from low-frequency vibrations with an amplitude larger than its internal displacement limit. In the PFupCG an inertial mass (LFO) is connected to the housing by a suspension with a bi-stable characteristic and a strong stiffening effect at the desired displacement limits. This stiffening effect acts as a mechanical stop and couples the motion of the LFO to the motion of a secondary oscillator (HFO) placed within the suspended structure. Energy is generated by a transducer harvesting from the relative motion between the inertial masses of the suspension system and the secondary oscillator.

The working principle of the generator is demonstrated in Fig. 5. Upon excitation by a driving motion with sufficient acceleration the inertial mass can snap out of one of its stable positions at $z = Z_l$ and $z = -Z_l$, pass its instable position at $z = 0$ and reach the displacement limit at the other side with considerable velocity. At the displacement limit the LFO will experience an impact-like behavior as a result of the strong stiffening effect of the suspension. This triggers an impulse response in the HFO such that it begins to vibrate in its own natural frequency, ω_2 . By designing $\omega_2 \gg \omega$ the designer can tune the Q -factor, and therefore the required damping factor of the HFO. Under optimal conditions, the LFO snaps back and forth between the two stable positions, exciting the HFO on every impact and generating power.

A. Suspension

For the PFupCG a suspension is proposed that combines the characteristics of a bistable system and those of mechanical stops, and can be modeled by a spring-damper system. Firstly, the force-deflection behavior of the suspension over the range of motion is modeled by spring with a negative stiffness. This negative stiffness is designed such that operation is possible at the target acceleration of a . Assuming a target total suspended mass of $M_t = M_1 + M_2$ the minimum stiffness of the suspension can be calculated. To ensure the suspended mass can break away from its stable positions at every

Fig. 3: Classification of frequency up-conversion strategies and corresponding mechanical diagrams based on coupling location and type for energy harvesting under low Q -factor constraints. LFO = low-frequency oscillator, HFO = high-frequency oscillator.

| Location of coupling | Type of coupling | Sub-type | Examples | | | |
|---|---|---|---|---|--|---|
| I: Base-LFO | | | | | | |
|  | Ia. Impact type | Ia1. Direct | [13], [14] , This work | | | |
| | | Ia2. Indirect | | | | |
| II: Base-HFO | | | | | | |
|  | IIa. Impact type | IIa1. Indirect | | | | |
| | IIb. Stick type | IIb1. Mechanical | | | | |
| | | IIb2. Non-mechanical | [15] | | | |
| III: LFO - HFO | | | | | | |
|  | IIIa. Impact type | IIIa1. Direct | [16]–[19] | | | |
| | | IIIa1. Indirect | [9] | | | |
|  | IIIb. Stick type | IIIb1. Mechanical | [20], [21] | | | |
| | | IIIb2. Non-mechanical | [8], [22]–[25] | | | |
| | IIIc. Transmission type | IIIc1. Rigid transmission | [26] | | | |
| | | IIIc2. Flexible transmission | | | | |
| Ia1 | Ia2 | IIa1 | IIb1 | IIb2 | IIIa1 | IIIa2 |
|  |  |  |  |  |  |  |
| IIIb1 | IIIb2 | IIIc1 | IIIc2 | | | |
|  |  |  |  | | | |

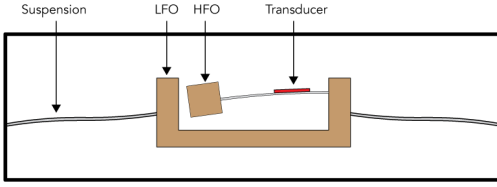


Fig. 4: Overview of the PFupCG architecture

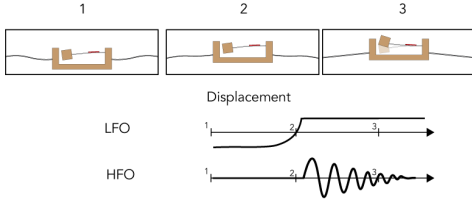


Fig. 5: Operating principle of the PFupCG; upon excitation the LFO snaps back and forth between its stable positions, exciting the HFO due to impact-like behavior as a result of the increased stiffness of the suspension at the displacement limits. Power is generated through a transducer placed between the LFO and the HFO.

cycle the calculated stiffness is multiplied by a factor $\beta < 1$.

$$K_1 = -\beta \frac{M_t a}{Z_l} \quad (6)$$

Secondly, the mechanical stop behavior can be modeled as a stiffness K_{end} and a damping coefficient of C_{end} that are added to the suspension when the proof-mass reaches one of its displacement limits. Very high values should be chosen for K_{end} and C_{end} to ensure the proof-mass loses all energy upon impact within a negligible distance, and generates a strong impact. The following expression was used to model the force-deflection behavior of the mechanical stops, F_{end} .

$$F_{\text{end}} = \left[K_{\text{end}}(|z| - Z_l) + C_{\text{end}}\dot{z} \right] \left(\frac{1}{2} + \frac{1}{2} \tanh(\gamma(|z| - Z_l)) \right) \quad (7)$$

where, γ is an arbitrary coefficient that controls how sudden the stiffness and damping coefficient will be implemented. Combining Eq.

6 and 7 results in a negative stiffness over the range of motion and a sudden increase in stiffness and damping coefficient at the displacement limits. The potential energy function and force-deflection profile of the suspension are shown in Fig. 6.

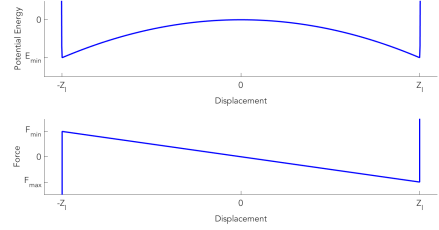


Fig. 6: Potential energy function and force-deflection characteristic of the suspension with a negative stiffness and a sudden increase in stiffness at the displacement limits.

B. High-frequency oscillator

The HFO is designed to have a natural frequency of $\omega_2 \gg \omega$. Due to the higher frequency, the oscillator has a high Q -factor and little damping has to be provided by the transducer. The design variables of the HFO are the *Up-conversion ratio* (UpR), and the *Oscillator mass ratio* (OmR). Those two variables determine the efficiency of the PFupCG for a given Q -factor and damping coefficient.

$$\text{UpR} = \frac{\omega_2}{\omega} \quad (8)$$

$$\text{OmR} = \frac{M_2}{M_t} \quad (9)$$

C. Modeling of the system dynamics

In the model shown in Fig. 7 two bodies can be identified, M_1 and M_2 . The lower body is the LFO, and is connected to the housing by a spring, K_1 , and a damper, C_1 , that represent the suspension model. The inner body is connected to the LFO by means of a spring, K_2 , and a damper, C_2 , and is called the HFO. The motions of the masses relative to the housing are $z_1 = x_1 - y$ and $z_2 = x_2 - y$, respectively. The motion of the LFO is limited to the internal displacement limit, Z_l , which is enforced by

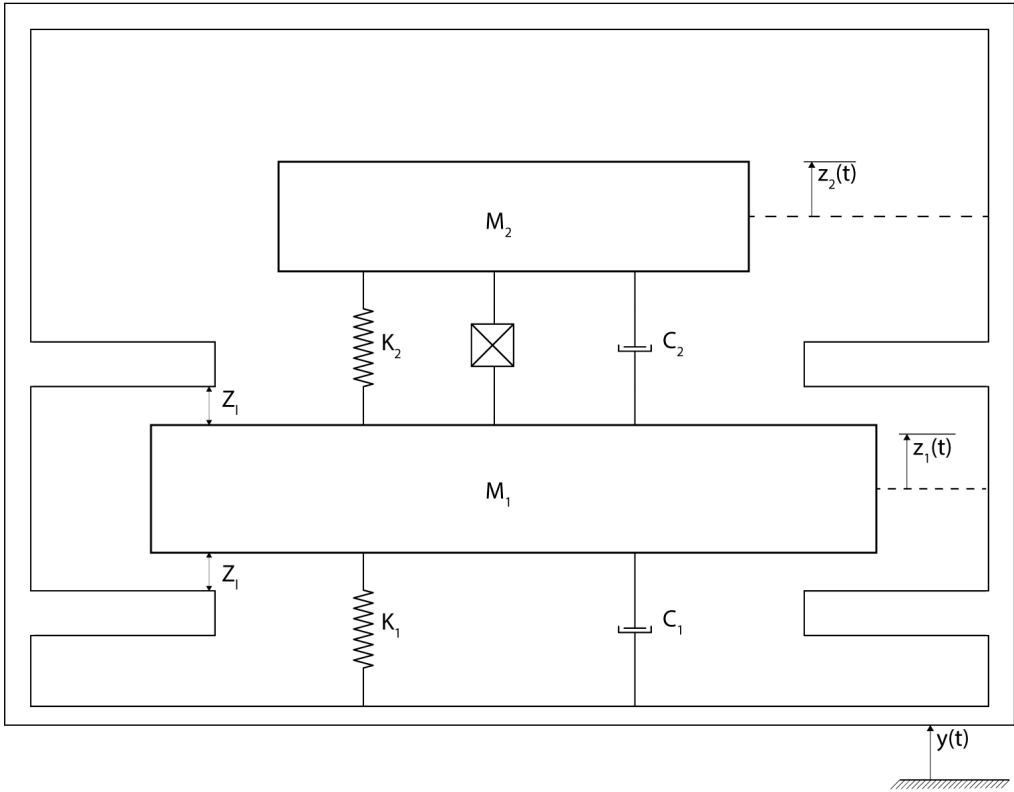


Fig. 7: General model of the system dynamics of the PFupCG

the suspension. This results in the following differential equations for the motion of the masses with respect to the frame for the two-mass model.

$$\begin{aligned}
 M_1 \ddot{z}_1(t) + C_1 \dot{z}_1(t) + C_2 (\dot{z}_2(t) - \dot{z}_1(t)) \\
 + K_1 z_1(t) + K_2 (z_2(t) - z_1(t)) \\
 + F_{\text{end}}(t) = -M_1 \ddot{y}(t). \quad (10) \\
 M_2 \ddot{z}_2(t) + C_2 (\dot{z}_1(t) - \dot{z}_2(t)) \\
 + K_2 (z_1(t) - z_2(t)) = -M_2 \ddot{y}(t).
 \end{aligned}$$

$$\frac{\partial z_1}{\partial t} = \dot{z}_1 \quad (11)$$

$$\begin{aligned}
 \frac{\partial^2 z_1}{\partial t^2} = & -\frac{C_1}{M_1} \dot{z}_1 + \frac{C_2}{M_1} (\dot{z}_2 - \dot{z}_1) \\
 & -\frac{K_1}{M_1} z_1 + \frac{K_2}{M_1} (z_2 - z_1) - F_{\text{end}} \\
 & -\omega^2 Y \sin(\omega t)
 \end{aligned}$$

$$\frac{\partial z_2}{\partial t} = \dot{z}_2$$

$$\begin{aligned}
 \frac{\partial^2 z_2}{\partial t^2} = & \frac{C_2}{M_2} \dot{z}_1 - \frac{C_2}{M_2} \dot{z}_2 \\
 & + \frac{K_2}{M_2} z_1 - \frac{K_2}{M_2} z_2 - \omega^2 Y \sin(\omega t)
 \end{aligned}$$

Since no closed form solution exists for the given equation, a numerical method is used. The equation was written as the following system of four first-order differential equations.

D. Efficiency and bandwidth comparison with the VDRG

The transducer in the PFupCG model is placed in between the two masses, and thus only the

power dissipated in c_2 harvested. This power is equal to the force-distance integral of the relative distance between the two masses over a full cycle of period T . Therefore, the following expression was found.

$$P_{\text{damper}} = -\frac{1}{T} c_2 \int_{-\frac{T}{2}}^{\frac{T}{2}} (\dot{z}_2 - \dot{z}_1)^2 dt \quad (12)$$

To make a fair comparison between the VDRG and PFupCG models, the models should be evaluated for equal Q -factors and transducer damping coefficients. Since the mass and frequency of the secondary oscillator are different than from the VDRG model, equal damping coefficients result in different damping ratios. Therefore, the damping ratio of the secondary oscillator in the PFupCG model is chosen according to the following expression.

$$\zeta_2 = \frac{C_e}{2M_2\omega_2} = \frac{M_t\omega}{M_2\omega_2} \zeta = \frac{\zeta}{\text{UpR OmR}} \quad (13)$$

Both models are evaluated for a range of Q -factors and ζ and their resulting power output was normalized by Eq. 4.

In real applications of vibration energy harvesting, the frequency of the vibration source may change over time and span a range of frequencies around the target frequency of the harvester. Therefore, the bandwidth of the generator is another important concept. Where high Q -factor generators are characterized by a narrow resonance peak, the low Q -factor devices may have a much broader spectrum of frequencies they can efficiently harvest. By evaluating the PFupCG and VDRG models over a range of driving frequencies and normalizing with Eq. 5 the bandwidth of the PFupCG strategy can be analyzed.

V. CASE STUDY PIEZOELECTRIC PFUPCG FOR HUMAN MOTION

A prototype of the PFupCG was developed based on the architecture discussed in the previous section. The target was to operate under a driving excitation of 2 Hz and 4 m s^{-2} , which is within the range of acceleration levels found

in the human head area during regular walking. The PFupCG concept is specifically designed for this type of motion where the amplitude of the driving motion is larger than the internal displacement limit of the generator. Therefore, the stroke limit of the generator, Z_l , was selected to be 5 mm. This resulted in a device with a Q -factor of 0.2 for the target operation conditions. A schematic representation of the PFupCG prototype is shown in Fig. 8.

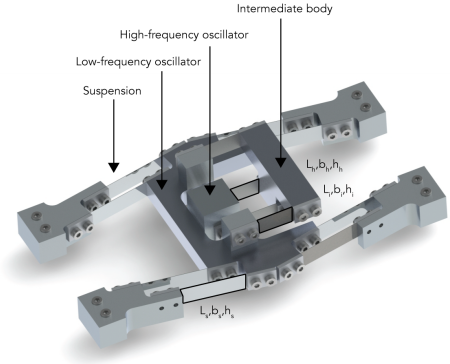


Fig. 8: Schematic representation of the piezoelectric PFupCG for human motion.

A. Mechanical design

The suspension of the PFupCG was designed using compliant mechanisms where the elastic elements are designed as spring steel flexures. The desired bi-stable behavior of the suspension was realized by mounting two flexures at angles of $\theta = 10 \text{ deg}$ such that a bridge structure is created, as shown in Fig. 9. Next to the schematic, the force-displacement graph is sketched.

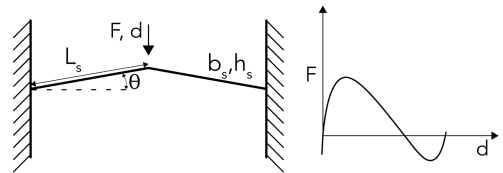


Fig. 9: Bridge structure using two flexures and corresponding force-displacement diagram.

In the prototype, two bridges facing upwards were combined with two bridges facing down-

wards, leaving a $2Z_l = 10$ mm gap in between. The assembly process is shown in Fig. 10, where part A is attached to part B such that a preload is induced that achieves two things simultaneously. First of all, the combination of the force-deflection graphs results in a bi-stable system with a symmetric force-deflection graph. Secondly, the target internal displacement limit is enforced by placing the stable points at $+Z_l$ and $-Z_l$. Moreover, if the system would be pushed further outwards from one of its equilibrium points, the beams would be loaded in tension which is much stiffer than their designed bending stiffness. Therefore, the beams function as end-stops with a greatly increased stiffness.

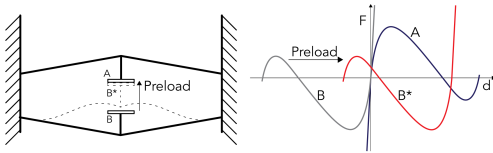


Fig. 10: Assembly of a bridge facing upwards with a bridge facing downwards induces a preload that shifts the force-deflection graph from B to B*; Summation of A and B* lead to the total symmetric force-deflection graph with stable points at the desired locations.

This suspension design offers the following advantages over the post-buckled flexure used in the state-of-the-art [13], [14]. In Fig. 11 the results of an ANSYS simulation of the force-deflection profiles of the two embodiments is shown for equal over-span lengths, widths and thicknesses. First of all, the robustness to parasitic rotations in the plane of the device is greatly increased due to the multitude of flexures. Secondly, the stiffness increases much faster at the displacement limit because the flexures are fully straightened at this point and loaded in tension only. This allows excellent control over the placement of the stable positions, and a more powerful impulse transmitted to the HFO. Lastly, the pre-loading process can be simpler because the reaction forces when pre-loading in the direction of motion are much smaller compared to the reaction forces when

pre-loading axially. As a downside, the break-away force of the double-bridge embodiment is slightly larger. Therefore, the flexures must be slightly longer to allow motion at the target acceleration compared to post-buckled beams of equal thickness.

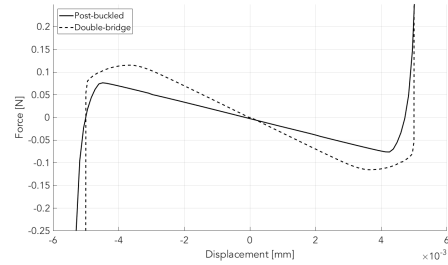


Fig. 11: Force-deflection analysis of the post-buckled beam and the double bridge embodiment.

For the suspension of the prototype, two double-bridge embodiments were built using spring steel ($E = 190$ GPa) flexures with a width of $b_s = 10$ mm, Thickness of $h_s = 0.05$ mm and an over-span length $L_s = 35$ mm made by laser micro-machining. A minimum break-away force of 0.465 N was found in simulation with ANSYS and the total suspended mass of the prototype was 140 g. Therefore, the prototype was expected to exhibit relative motion for accelerations greater than $a = 3.3 \text{ m s}^{-2}$.

The HFO is also suspended by spring steel flexures, and connected to the LFO through an intermediate body. The intermediate body limits parasitic rotations and translations and acts as a linear guiding mechanism for the LFO. Therefore, the effects of the reaction moments of the HFO on LFO and its relatively compliant suspension are limited. The stiffnesses of the fixed-guided flexures of HFO can be calculated using linear beam theory.

$$K = \frac{Ebh^3}{L^3} \quad (14)$$

Between the LFO and the intermediate body, spring steel ($E = 190$ GPa) flexures are used with a width of $b_i = 10$ mm, thickness of $h_i = 0.20$ mm and an over-span length of

$L_i = 20$ mm made by laser micro-machining. Using Eq. 14 the stiffness of these flexures was calculated to be $K_i = 1900 \text{ N m}^{-1}$. Between the intermediate body and the HFO, flexures with a thickness of $h_h = 0.10$ mm were used with a stiffness of $K_h = 237.5 \text{ N m}^{-1}$. The mass of the HFO was $M_h = 26$ g and the mass of the intermediate body was $M_i = 33$ g. As a result, following frequency response function was found for the HFO assembly.

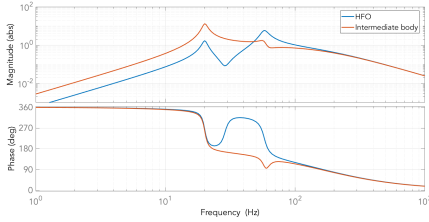


Fig. 12: Frequency response function of the HFO assembly.

From the figure it can be seen that the lowest eigenmode is around 20 Hz and has a much greater amplitude compared to the second eigenmode. Therefore, it can be concluded that the 2DoF lumped mass model presented in Fig. 7 provides a good approximation for the motion of the HFO. The body parts of the prototype were fabricated from aluminum by milling. The spring steel flexures were mounted by clamping them between the aluminum parts and a 2 mm aluminum plate by means of bolts. This resulted in the prototype shown in Fig. 13. The dimensions of the prototype were a length of 105 mm, width of 195 mm and a height of 30 mm. Therefore, the total volume of a box around the prototype would be 614 cm^3 . Concluding, a summary of the mechanical design parameters is given in Table I.

TABLE I: Summary of mechanical design parameters used in the PFupCG prototype.

| Parameter | Symbol | Value |
|-----------------------------|------------|--------------------|
| Q-factor | Q | 0.2 |
| Internal displacement limit | Z_l | 5 mm |
| Total volume | V_t | 614 cm^3 |
| Total suspended mass | M_t | 140 g |
| HFO mass | M_h | 26 g |
| Intermediate body mass | M_i | 33 g |
| HFO natural frequency | ω_2 | 20 Hz |
| Up-conversion ratio | UpR | 10 |
| Oscillator mass ratio | OmR | .19 |



Fig. 13: Prototype of the PFupCG.

B. Transducer Design

A piezoelectric transducer was placed on one of the 0.1 mm flexures between the intermediate body and the HFO. A sheet of PVDF from TE Connectivity (*Part No. 3-1003702-7*) with a thickness of $110 \mu\text{m}$ was attached on the topside of the flexure using epoxy (RS 553-614) and the middle part of the electrode on the top side of the PVDF was removed. The unimorph transducer was clamped using an insulating PLA clamp with a thickness of 2 mm. A side view of the transducer assembly and its working principle is shown in Fig. 14.

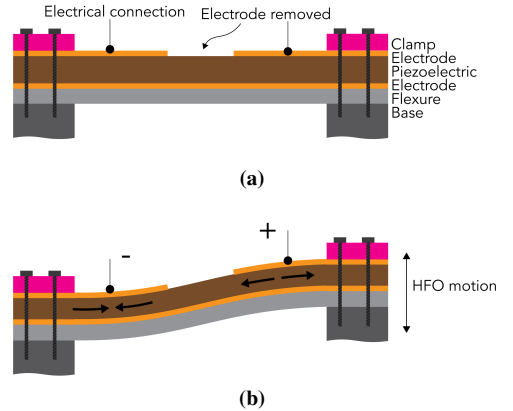


Fig. 14: (a) Components and (b) working principle of the piezoelectric transducer mounted between the intermediate body and the HFO.

Because the HFO is connected to the intermediate body by two parallel flexures, the transducer assembly behaves as a fixed-guided beam. As a result of the HFO motion, compressive strains are induced in one half of the PVDF and tensile strains in the other half.

Therefore, opposite charges are induced on the topside electrodes with respect to the bottom side electrode. Because the electrodes are not separated on the bottom side this effectively creates a series arrangement of the piezoelectric transducer with itself. As a result, wires are connected only to the two top electrodes.

C. Experimental Setup

The experimental setup consists of a frequency generator, a measurement system and the PFupCG prototype and is shown in Fig. 15. The frequency generator is custom-built and consists of a crank-slider mechanism driven by an electro-motor. The frequency of the driving vibration can be controlled by controlling the voltage fed to the motor, and the amplitude of the driving vibration is fixed at 25 mm by the kinematics of the crank. The measurement system consists of three laser interferometer position sensors from Micro-Epsilon (ILD 1420-200). Three positions are measured simultaneously. The slider position, y , the position of the LFO, x_1 , and the position of the HFO, x_2 . The relative positions of the oscillators can be found by subtracting the position of the slider such that $z_1 = x_1 - y$ and $z_2 = x_2 - y$ give the relative positions of the LFO and HFO, respectively.

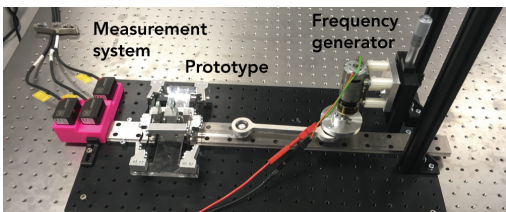


Fig. 15: Experimental setup consisting of crank-slider mechanism, laser position sensors and the PFupCG prototype.

VI. RESULTS

A. Design variable analysis

In Fig. 16 the results of changing the design variables of the PFupCG on the power output can be observed. In this analysis, a cubic type generator where exactly half of the available volume is taken up by the proof mass was

assumed such that $M_t = \frac{1}{2}(4Z_1)^3$. Moreover, the damping coefficient was fixed at $\zeta = 0.04$ and the Q -factor was fixed at 0.2. When fixed, the design variables of $UpF = 10$ and $OmR = 0.05$ were used. From the figure can be seen that the best results are obtained for $7 < UpR < 100$ and $0.04 < OmR < .2$.

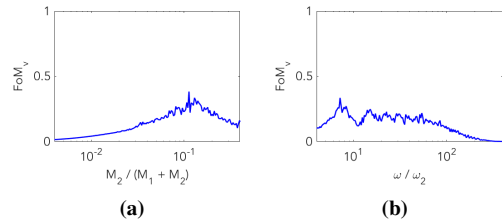


Fig. 16: Sensitivity analysis of design variables OmR (a) and UpR (b).

B. Efficiency comparison with the VDRG

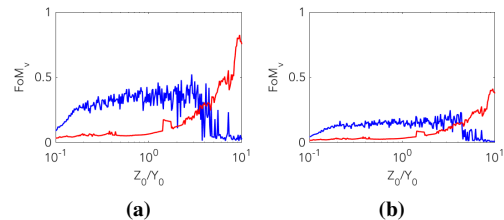


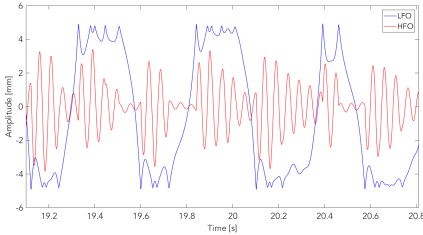
Fig. 17: Power output comparison of PFupCG (blue) and VDRG (red) models. Power output was normalized using Eq. 4.

The resulting power outputs of the simulated PFupCG model and VDRG model are plotted in Fig. 17 for varying Q -factors. For both models, a total damping factor of $\zeta = 0.04$ was used. In the first plot, the damping was modeled of fully electrical nature and in the second plot the damping was spread evenly over the electrical damping coefficient, C_e , and the mechanical (parasitic) damping coefficient, C_m . The PFupCG model was evaluated for $UpF = 10$ and $OmR = 0.05$ and the output powers were normalized using Eq. 4. It can be seen that the VDRG model has the highest power output when approaching the optimal damping condition of $\zeta = \frac{2}{Q}$. However, when

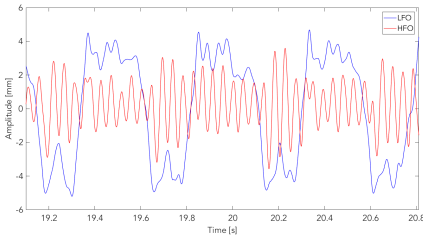
systems are considered with a damping much lower than the optimal conditions, the PFupCG architecture has a significantly better performance.

C. Dynamical testing

The model was simulated using parameters given in Table. I and a damping factor of $\zeta = 0.04$. The results of the simulation of the PFupCG model and the experimental measurements of the prototype are plotted in Fig. 18. The blue line shows the time response of the LFO w.r.t. the base, $z_1 = x_1 - y$, and the red line shows the relative motion of the HFO w.r.t. the LFO, $z_2 = x_2 - x_1$.



(a) Model



(b) Experiment

Fig. 18: Results of the relative motions of the LFO and the HFO in the PFupCG (a) model and (b) experiment.

These motions can also be plotted as the phase projections shown in Fig. 19 with the position z_1 and the velocity \dot{z}_1 on the horizontal and vertical axes, respectively. The spectral contents of the experimental results were analyzed and the results are shown in Fig. 20. From the figure it can be seen that input vibration signal was applied with the target frequency of 2 Hz. Moreover, the relative motion of the

HFO shows a large amount of spectral content around 20 Hz, which corresponds to the natural frequency of the HFO.

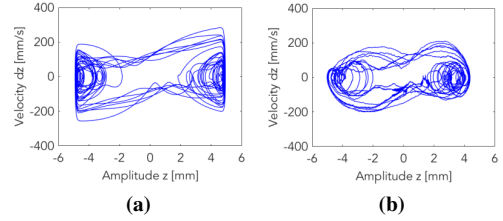


Fig. 19: Phase projections of motions of the LFO in the PFupCG (a) model and (b) experiment.

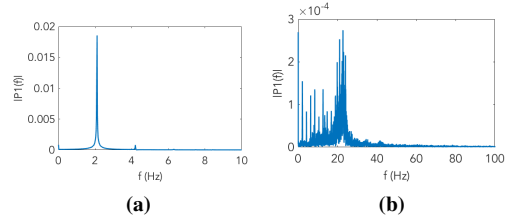
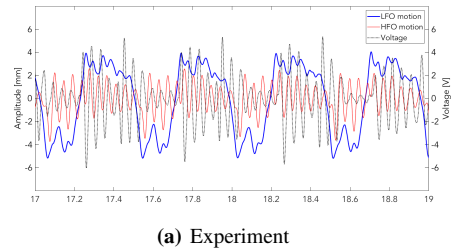


Fig. 20: Frequency spectra of input vibration, y , (a) and relative HFO motion, z_2 , (b). The frequency up-conversion with a factor of 10 can be clearly observed.

D. Power output

The transducer was connected to a $3.91 \text{ M}\Omega$ resistor is measured over the resistor. In Fig. 21 the resulting voltage is shown next to the recorded LFO and HFO motions. It can be seen that a maximum of $1.8 \mu\text{W}$ was measured over a frequency range of $2.2 - 3.1 \text{ Hz}$. When the driving frequency was increased above 3.1 Hz , the power output dropped to $1 \mu\text{W}$.



(a) Experiment

Fig. 21: Results of the relative motions of the LFO and the HFO, and transducer output voltage.

The output power of the transducer is shown in Fig. 22 for different operating frequencies. The frequency was varied between 0 and 3.7 Hz, while keeping the amplitude constant.

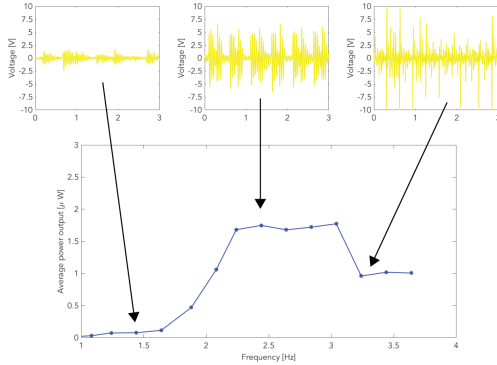


Fig. 22: Output power of the transducer for different operating frequencies.

VII. DISCUSSION

A. Results

In this work, an energy harvester concept was developed that aims to use the impact of an inertial mass on a mechanical stop to excite a high-frequency harvesting element. A model was developed that predicted the LFO snapping back and forth between the stable positions when driven by a harmonic input. Moreover, the modeled response clearly shows that the HFO was excited in its natural frequency as a result of the impact of the LFO on the mechanical stops. Furthermore, a prototype of the PFupCG was successfully fabricated and tested experimentally. The results of this experiment confirmed the behavior predicted by the model. Specifically, the results of the spectral analysis presented in Fig. 20 it can be clearly seen that the target frequency up-conversion with $UpF = 10$ was achieved in the HFO. Therefore, it was concluded that the working principle of the PFupCG was confirmed by model and experiment. Additionally, the results of the mathematical model, shown in Fig. 17 that the PFupCG can provide a significant performance increase over the existing VDRG architectures in situations where the amplitude of the

motion is large compared to the dimensions of the device.

B. Model validation

From the responses of the model and experiment the following observations can be made. In both the simulation and experiment of the phase projections of the LFO shown in Fig. 19 it can be seen that the LFO exhibits a chaotic motion which can be described by two competing point attractors located at the stable points at $z_1 = Z_l$ and $z_1 = -Z_l$. The most prominent differences in the behavior of the LFO can be observed near the mechanical stops in Fig. 18. In the model, the velocity of the LFO changes much faster upon hitting the mechanical stop. Furthermore, the LFO returns to the mechanical stop much faster, allowing for multiple secondary impacts. In the experimental results, the velocity change upon hitting the mechanical stop is more smooth and secondary impacts occur after a longer time, if at all. This difference can be explained by the differences in the force-deflection behavior of the suspension that was modeled (Fig. 6) and the one found with ANSYS (Fig. 9). Especially the small section with a positive stiffness next to the mechanical stops is believed to prevent the secondary impacts in the experiment. Furthermore, it can be seen that the experimental result has a very slight preference of the stable position at $z_1 = Z_l$. This can be explained by manufacturing tolerances or a slight offset of the setup from the horizontal such that gravity has a component in the DoF. This could explain why the HFO of the experiment is mainly excited when the LFO impacts the mechanical stop at $z_1 = -Z_l$. Lastly, the HFO motion damps out faster in the simulation compared to the experiment which indicates that the modeled damping factor was too high. In conclusion, a more accurate model of the suspension force-deflection curve would most likely result in a better correspondence of the model and experiment in those sections. However, the differences are not of major importance to the performance of the system, and therefore it is

concluded that the used model is valid.

C. Domains of operation

In theory, the impact of the LFO and resulting excitations of the HFO produce a decaying impulse response that can be observed in the voltage signal. In Fig. 21 this effect can be observed. Moreover, it is shown in the figure that the voltage signal follows the relative motion signal of the HFO. From the measured responses shown in Fig. 22 a clear insight can be obtained in the operation different frequencies. From the response at 1.4 Hz, the LFO impacts can be clearly observed but produce a low voltage due to the low impact energy. As a result, the power output is limited by the impact energy. At 2.5 Hz, the impacts have more energy resulting in higher voltages. It can be seen that at this frequency a clear pattern emerges where the HFO comes to rest right before excitation of the next impact occurs. Moreover, the secondary impacts can be observed from the voltage signal. This is the optimal region of operation for the FPupCG, and the highest power output is achieved. When the frequency is further increased beyond 3 Hz the HFO is not allowed to finish its ring-down before the next impact occurs. This results in an uncontrolled motion of the HFO and a reduced power output. In this sub-optimal region of operation the power output is limited by the time constant of the ring-down of the HFO motion.

D. Performance and miniaturization of the PFupCG

A maximum power output of $1.8 \mu\text{W}$ was measured over a frequency range of 2.2 – 3.1 Hz. With Eq. 4 the FoM_v of the PFupCG prototype was calculated to be 1.5522×10^{-10} . This extremely low value is mainly due to the efficiency of the transducer. The transducer in this prototype was merely a qualitative demonstrator and the performance of the PFupCG could be improved by orders of magnitude by designing a proper transducer. Specifically, improvements such as using

another piezoelectric material with a much higher coupling factor, such as PZT-5H, and manufacturing the transducer as a bi-morph can result in an increased power output.

Furthermore, the large dimensions and mass of the prototype contributed to the inefficient performance. In an optimal theoretical embodiment, the device with a stroke of $Z_l = 5 \text{ mm}$ could be manufactured within an 8 cm^3 volume. The total suspended mass of the device would be $M_t = 32 \text{ g}$ when manufactured from iron with a density of $\rho = 8 \text{ g cm}^{-3}$. For the up-scaled prototype the volume and mass were much larger, due to limitations on material, manufacturing processes and time. However, the displacement limit and dynamics of a miniature version would be equal to up-scaled prototype and therefore have the potential to reach much higher efficiencies. Development of a miniaturized PFupCG device will be the direction of further research.

VIII. CONCLUSION

The main novel contributions from this work are the classification of frequency up-conversion strategies, the PFupCG concept and analysis of the corresponding generalized model and the prototype with a compliant suspension embodiment that exhibits strong stiffening effects at the desired displacement limits. For operating conditions where the driving motion has a larger amplitude than the internal displacement limit of the generator, such as when harvesting from (low-frequency) human motion, the frequency up-conversion strategy can result in an increased power output. This was demonstrated by means of a simulation for a driving vibration with a frequency of 2 Hz and an amplitude of 25 mm using a generator with a Q -factor of 0.2. Moreover, the PFupCG prototype validated the dynamical properties of model, but was unable to achieve a relevant FoM_v as a result of its size and inefficient transducer design. It is expected that a miniaturized version of the PFupCG with a proper transducer can result in a competitive FoM_v w.r.t. the state-of-the-art.

REFERENCES

- [1] CB Williams and Rob B Yates. Analysis of a micro-electric generator for microsystems. *sensors and actuators A: Physical*, 52(1):8–11, 1996.
- [2] Paul D Mitcheson, Tim C Green, Eric M Yeatman, and Andrew S Holmes. Architectures for vibration-driven micropower generators. *Journal of microelectromechanical systems*, 13(3):429–440, 2004.
- [3] Paul D Mitcheson, Eric M Yeatman, G Kondala Rao, Andrew S Holmes, and Tim C Green. Energy harvesting from human and machine motion for wireless electronic devices. *Proceedings of the IEEE*, 96(9):1457–1486, 2008.
- [4] Thomas Von Buren, Paul D Mitcheson, Tim C Green, Eric M Yeatman, Andrew S Holmes, and Gerhard Troster. Optimization of inertial micropower generators for human walking motion. *IEEE Sensors Journal*, 6(1):28–38, 2006.
- [5] Matthias Geisler, Sebastien Boisseau, Matthias PEREZ, Pierre Gasnier, Jerome Willemin, Imene Ait-Ali, and Simon Perraud. Human-motion energy harvester for autonomous body area sensors. *Smart Materials and Structures*, 2016.
- [6] DF Berdy, DJ Valentino, and D Peroulis. Kinetic energy harvesting from human walking and running using a magnetic levitation energy harvester. *Sensors and Actuators A: Physical*, 222:262–271, 2015.
- [7] A Haroun, I Yamada, and S Warisawa. Investigation of kinetic energy harvesting from human body motion activities using free/impact based micro electromagnetic generator. *Diabetes Cholest metabol*, 1(104):13–16, 2016.
- [8] Pit Pillatsch, Eric M Yeatman, and Andrew S Holmes. A piezoelectric frequency up-converting energy harvester with rotating proof mass for human body applications. *Sensors and Actuators A: Physical*, 206:178–185, 2014.
- [9] Miah Abdul Halim and Jae Yeong Park. Piezoelectric energy harvester using impact-driven flexible side-walls for human-limb motion. *Microsystem Technologies*, pages 1–9, 2017.
- [10] SP Beeby, MJ Tudor, RN Torah, S Roberts, T O donnell, and S Roy. Experimental comparison of macro and micro scale electromagnetic vibration powered generators. *Microsystem Technologies*, 13(11-12):1647–1653, 2007.
- [11] Paul D Mitcheson, Elizabeth K Reilly, T Toh, Paul K Wright, and Eric M Yeatman. Performance limits of the three mems inertial energy generator transduction types. *Journal of Micromechanics and Microengineering*, 17(9):S211, 2007.
- [12] Haluk Kulah and Khalil Najafi. Energy scavenging from low-frequency vibrations by using frequency up-conversion for wireless sensor applications. *IEEE Sensors Journal*, 8(3):261–268, 2008.
- [13] Seok-Min Jung and Kwang-Seok Yun. Energy-harvesting device with mechanical frequency-up conversion mechanism for increased power efficiency and wideband operation. *Applied Physics Letters*, 96(11):111906, 2010.
- [14] Seok-Min Jung and Kwang-Seok Yun. A wideband energy harvesting device using snap-through buckling for mechanical frequency-up conversion. In *Micro Electro Mechanical Systems (MEMS), 2010 IEEE 23rd International Conference on*, pages 1207–1210. IEEE, 2010.
- [15] AM Wickenheiser and E Garcia. Broadband vibration-based energy harvesting improvement through frequency up-conversion by magnetic excitation. *Smart materials and Structures*, 19(6):065020, 2010.
- [16] D Alghisi, S Dalola, M Ferrari, and V Ferrari. Triaxial ball-impact piezoelectric converter for autonomous sensors exploiting energy harvesting from vibrations and human motion. *Sensors and Actuators A: Physical*, 233:569–581, 2015.
- [17] Miah A Halim, Hyunok Cho, Md Salauddin, and Jae Y Park. A miniaturized electromagnetic vibration energy harvester using flux-guided magnet stacks for human-body-induced motion. *Sensors and Actuators A: Physical*, 249:23–31, 2016.
- [18] Y Lu, F Cottone, S Boisseau, F Marty, D Galayko, and P Basset. A nonlinear mems electrostatic kinetic energy harvester for human-powered biomedical devices. *Applied Physics Letters*, 107(25):253902, 2015.
- [19] Lei Gu and Carol Livermore. Impact-driven, frequency up-converting coupled vibration energy harvesting device for low frequency operation. *Smart Materials and Structures*, 20(4):045004, 2011.
- [20] Bharat Kathpalia, David Tan, Ilan Stern, and Alper Erturk. Evaluation of human-scale motion energy harvesting for wearable electronics. In *SPIE Smart Structures and Materials+ Nondestructive Evaluation and Health Monitoring*, pages 101641H–101641H. International Society for Optics and Photonics, 2017.
- [21] Sheng Wei, Hong Hu, and Siyuan He. Modeling and experimental investigation of an impact-driven piezoelectric energy harvester from human motion. *Smart Materials and Structures*, 22(10):105020, 2013.
- [22] Tzeno Galchev, Hanseup Kim, and Khalil Najafi. Micro power generator for harvesting low-frequency and nonperiodic vibrations. *Journal of Microelectromechanical Systems*, 20(4):852–866, 2011.
- [23] Tzeno Galchev, Ethem Erkan Aktakka, and Khalil Najafi. A piezoelectric parametric frequency increased generator for harvesting low-frequency vibrations. *Journal of Microelectromechanical Systems*, 21(6):1311–1320, 2012.
- [24] Y Minami and E Nakamachi. Development of enhanced piezoelectric energy harvester induced by human motion. In *Engineering in Medicine and Biology Society (EMBC), 2012 Annual International Conference of the IEEE*, pages 1627–1630. IEEE, 2012.
- [25] QC Tang, YL Yang, and Xinxin Li. Bi-stable frequency up-conversion piezoelectric energy harvester driven by non-contact magnetic repulsion. *Smart Materials and Structures*, 20(12):125011, 2011.
- [26] Longhan Xie, Jiehong Li, Siqu Cai, and Xiaodong Li. Design and experiments of a self-charged power bank by harvesting sustainable human motion. *Advances in Mechanical Engineering*, 8(5):1687814016651371, 2016.

Chapter 5

Reflection, conclusions and recommendations

Thijs BLAD

*“The most important thing is to keep the most important thing
the most important thing.”*

Donald P. Coduto

This chapter reflects on the approach, process and execution of the graduation project. An overview of the research activities is presented schematically and some successful and unsuccessful activities are discussed in further detail. Finally, the most important conclusions are listed and recommendations are proposed for future research.

5.1 Overview of research activities

An overview of all the research activities and the corresponding achievements is shown schematically in Fig. 5.1. In total, the graduation project spanned a time-line of 14 months from September 1st 2016 to November 1st 2017. During this time, the research resulted in three papers, four prototypes and two experiments. Furthermore, a great deal of knowledge, insights and practical experiences were acquired in the field of vibration energy harvesting.

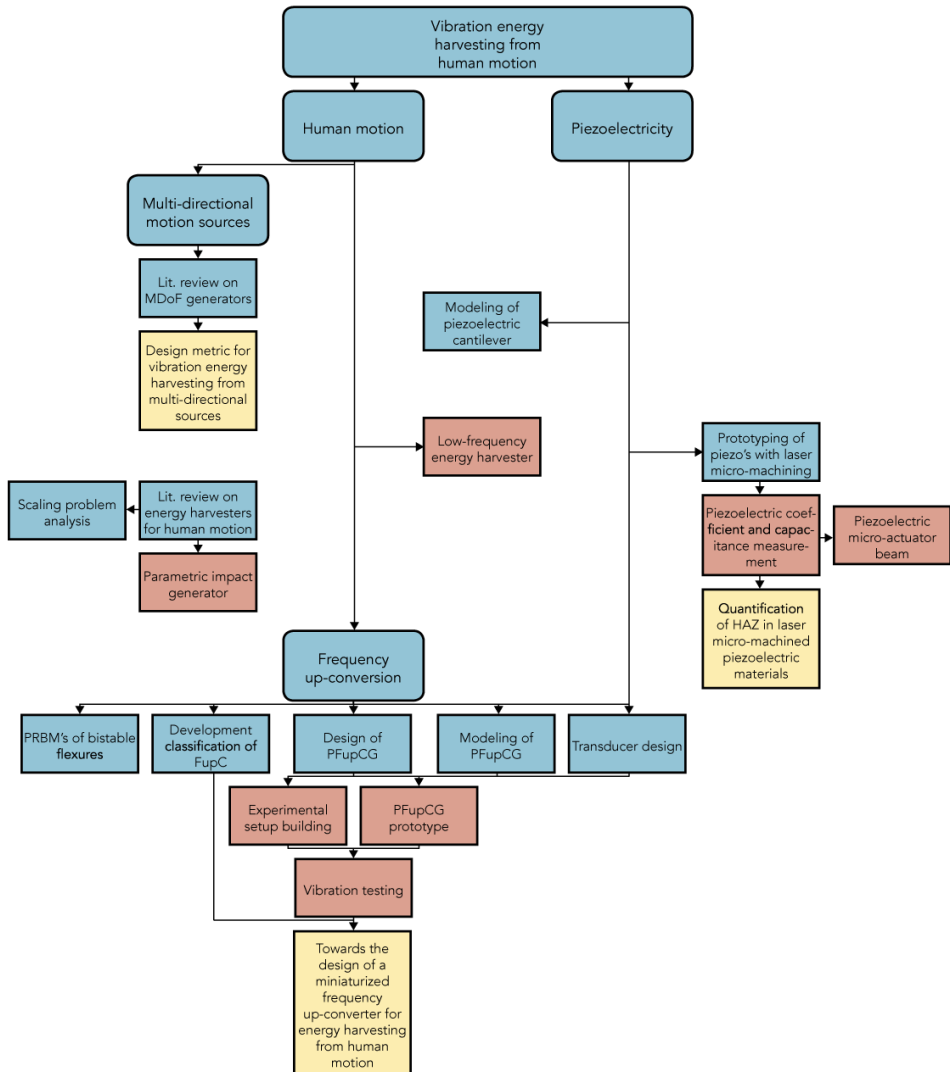


Figure 5.1: Overview of research activities and achievements over time of the project. Blue indicates a line of research and corresponding research activities, yellow indicates an article and red indicates practical or experimental work.

5.2 Successes

Over the course of the project, many things worked out well, were executed successfully or led to usable results. The greatest successes of this project are the learning process, the design process, and the practical work. These topics will be discussed in further detail.

5.2.1 Learning process

In view of the author, the greatest achievement was the learning process that was experienced during the graduation project. One of the most difficult challenges at the beginning of the project was to form a clear overview of the challenges in the field of vibration energy harvesting. This was especially hindered because the majority of publications had an electrical engineering point of view and sometimes disregarded basic mechanical engineering principles. In retrospect it took almost half a year to discover that the main challenge was the actual extraction of energy from the system by obtaining relevant amounts of damping. Throughout the project, a great amount of field-specific knowledge was learned which led to a thorough understanding of the fundamentals, challenges and concepts in the field of vibration energy harvesting.

Furthermore, general research related skills were acquired or improved upon during the project. These skills include academic writing, prototyping, planning, presenting, conducting a literature review, dealing with setbacks and the general management of your own research project.

5.2.2 Design process

The design process is considered a particularly strong point of this thesis due to the clear methodology that was used and maintained during multiple iterations. At the start, much thought was invested to result in the identification of the three functions of the generator. This effort repaid itself because the clear definition of functions greatly aided pattern recognition in later stages of the design process. The design process was set up to go from very general, such as assessing different options on a concept-strategy level, to very specific and detailed, such as comparing force-deflection graphs of flexure embodiments. This methodology worked out really well as it made sure no options were overlooked in the beginning, and a best concept could be selected in the end based on measurable quantities. Moreover, prior to every selection stage it was attempted to invest much effort in defining the selection criteria, such that the selection could be conducted without subjectivity. A couple of times, this resulted in new insights when underdog concepts came out on top of the author's favorites.

5.2.3 Practical work

The final success that will be discussed is the practical work done on the development of the prototypes and the experimental setup. It was learned quickly that there is a world of difference between simulation of a model and carrying out an actual experiment. The

most difficult task was to find a suitable way to test the prototype under the desired vibration conditions. Attempts with two different air-bearing stages took over 3 months and eventually concluded that the encoder in one of the stages was broken, and the other was unable to follow the desired velocities. Therefore, a crank-slider driving mechanism was fabricated which could fulfill the task and proved to be reliable.

Although it was not strictly necessary, the author decided to make the final prototype and crank-slider mechanism out of aluminum parts. The main reason for this decision was the desire to have a high-quality prototype that is worthy of a graduation project. Considering that prior to this project the only practical experience of the author with machining work were the first-year instructions on milling and turning, this was quite a challenge. Nevertheless, the result is a properly working prototype and experimental setup of great quality.

5.3 Unsuccessful attempts

5

“Failures, repeated failures, are finger posts on the road to achievement. One fails forward toward success.”

C. S. Lewis

For everything that succeeded, there are things that did not work out well or did not produce useful results. Upon some of those unsuccessful attempts will be reflected.

5.3.1 Piezoelectric models

Many of the models that were used in this project use the concept of viscous damping. With the intended application of a piezoelectric transducer in mind, it should be noted that the viscous damping model is an over-simplification of the dynamical processes in the transducer. Therefore, the dynamics should be carefully assessed to prevent inaccurate results and false conclusions. At the beginning of the project it was attempted to construct models for the piezoelectric transducer systems based on the approaches mentioned in [8]. Effort was made to construct constitutive equations for a beam with a piezoelectric layer and implement them in a Simulink model, as can be found in appendix F. However the process was extremely time consuming and no successful results had been acquired after weeks of work. Effectively, this pushed the project towards a more electrical engineering based transducer design project, which was not in line with the intended line of research. Therefore, it was decided to leave the exact modeling of the piezoelectric transducers, and use the much more simple viscous damper models instead.

5.3.2 Bistable flexure models

The desire to synthesize bistable flexures based on a force-deflection profile was the motivation behind the attempt described in appendix E. An approach based on pseudo-rigid-body models was chosen due to its simplicity and successful results in the domain

of compliant mechanisms [29, 30]. With this approach the results that can be found by linear beam theory could be successfully replicated. Various methods were used, and a new equation was found that could be used to synthesize the bistable preloaded fixed-guided flexure. However, the results from this equation were not in line with the results acquired through ANSYS and therefore the model was not deemed valid. This process also took a few weeks and started to take up too much time that could be better spent on the main line of research. Therefore, it was decided to no longer continue on this topic during the graduation project. Nevertheless, the PRBM approach is an interesting line of research and could very possibly result in a more accurate equation for the synthesis of bistable flexures, when investigated more thoroughly in future research.

5.3.3 PZT transducer

A transducer manufactured from PZT would have a greatly increased performance compared to a PVDF counterpart due to the much higher coupling factor of the material. However, due to the brittle nature of the PZT no successful transducer was developed with this material. Although the transducer is a fundamental part of the energy harvester, the main focus of this project was on the dynamics of the generator. Therefore, the absolute performance of the transducer was not considered of great importance.

5.4 Conclusions

Vibration energy harvesting from human motion can be used as a sustainable power source for miniaturized electronic devices in biomedical applications. A new classification of harvesting strategies from multi-directional motion sources was proposed and it was demonstrated that a multi-directional approach can increase the available power for the case study by up to 16%. However, the efficient generation of energy from such a low-frequency-large-amplitude motion with a miniaturized device is not possible using classical energy harvester concepts. The main reason for this is a scaling problem in the maximum amount of damping that can be generated by the transducer prevents getting energy out of the system.

A strategy based on frequency up-conversion by impact was explored and resulted in the parametric frequency up-converter generator (PFupCG) concept that can allow efficient harvesting in the considered case study. Alternative strategies of frequency up-conversion methods were also identified and a new classification was proposed. In the considered concept, a bi-stable suspension with a break-away force equal to the maximum inertial force results in the highest power output. Using compliant mechanisms, the bi-stable suspension could be equipped with a strong stiffening effect such that it could function as a mechanical stop and therefore, two functions could be integrated in a single part.

Simulation of the PFupCG model showed that when harvesting from low-frequency-large-amplitude motion, the PFupCG can greatly outperform the classical vibration energy harvester concepts in terms of power output. Moreover, the dynamical properties of the model were validated by experimental testing of a PFupCG prototype. Therefore, it can be concluded that the working principle of the PFupCG is validated and it is expected that a miniaturized version of the PFupCG with a proper transducer can result in a competitive FoM_v w.r.t. the state-of-the-art.

5.5 Recommendations

Firstly, the proposed classification of frequency up-conversion strategies is a recommended starting point for future research. It would be very interesting to develop basic figures by which the performance of the sub-types can be assessed and compared. Without a doubt, this could result in new insights in frequency up-conversion and be a good starting point for a future publication. Moreover, in the classification there are four sub-types where not examples could be found. Modeling, prototyping and testing of those embodiments could also be a great starting point for future work and possibly result in publications or patents.

Secondly, optimization and miniaturization of the PFupCG concept are a logical continuation of the work in this thesis. It is expected that especially the design of a proper transducer could result in a device with a competitive power output. Moreover, micro-fabrication methods and design could facilitate the miniaturization of the PFupCG to a

degree where it could be applied in wearable devices. Experiments where power generation is monitored with test subjects walking or performing other activities would make a good basis for future publications. Once this is achieved, the project could be raised to an integration and application level and possibly be applied in commercial products. Specifically, devices worn used during exercise are recommended.

Thirdly, the fields of chaos and nonlinear dynamics are recommended as interesting sources of insights for vibration energy harvesting from human motion. Most generators considered in literature follow predefined trajectories and have well-described motions. However, some examples were also reported where the motion of an inertial mass was essentially unconstrained within a given area. Although no models were developed to describe the motion of those devices, their performances in terms of power output were surprisingly good. Therefore, it is recommended to further investigate these types of generators.

Fourthly, it is recommended to pursue the development of a general overview of the field of energy harvesting. The sheer amount of problems, strategies, concepts and makes it incredibly hard for a newcomer to grasp the fundamental principles underlying ideas. Some great classifications exist of specific domains within the field, but are not yet integrated in an overview that allows the reader to see the full picture. This is probably a very difficult task, but it is believed that the identification of the functions of an energy harvester as done in this thesis can be a good starting point for such an overview.

Finally, some general recommendations are listed for future work.

- When exploring a new field, prefer reading books over review articles over papers.
- Just building something is often a more convenient way of testing than ANSYS.
- PVDF is a good prototyping replacement for the brittle PZT, but virtually no power output.
- Flexures of 0.05 mm can best be cut with a mechanical scissors, or by micro-laser machining.
- The act of gluing spring steel flexures in slots of PMMA parts is great for prototyping conceptual ideas. However, a huge variance is observed in the force-deflection behavior of preloaded flexures.

Acknowledgements

First of all, I would like to thank my supervisor and coach Just Herder and Nima Tolou for the opportunity to do this project under their supervision. Although I had the opportunity to manage the project in my own way, they always could provide me with proper critical feedback and guiding counsel despite their busy schedules. Furthermore, I am grateful for the effort they made to offer me the opportunity to continue my research as a PhD within the department.

Furthermore, I am greatly indebted to my mentor, future colleague and friend Davood Farhadi Machekposhti. Thank you for the numerous hours of discussion, guiding counsel, practical tips, supply of material and evergreen enthusiasm for my project.

Next, I thank my board members of Dispuut Taylor, the study association of the department, with whom I shared many great moments during the graduation project. Maarten, Menno, Miranda and Niek, I might sometimes have put my graduation project on the first place, which resulted in agenda's being completed minutes before our weekly meetings and me continuing to finish work while we were having beers in the office, but I'm sure you can all agree we did an amazing job together and had a great experience. A special thanks is due to Menno who was always willing to drop everything to discuss my crazy ideas, or debug my MATLAB scripts.

In the same category are my friends Jelmer, Stefhan and Elias, who contributed to the project and my social health alike through discussions, reviews, tips and counsel often paired with drinks at the Taylor receptions. Furthermore, I thank all my other friends not mentioned specifically here for their support and engagement throughout the year.

In particular I owe a thank you to Boran Jia, for the great collaboration we had working on laser micro-machining of my designs using your methods.

I would like to thank my family and particularly my parents for their emotional support and advice during this project, and the prior years.

Lastly, I owe the greatest expression of gratitude to Marit van de Kamp, for her patience, everlasting support and love. As a partner and running mate, she has been of great significance to the completion of this thesis.

APPENDICES

Appendix A

Collaboration paper

Thijs BLAD, Boran JIA

*"Projects we have completed demonstrate what we know
future projects decide what we will learn."*

Dr. Mohsin Tiwana

Originally appeared as: "Quantifying the Heat Affected Zone in Laser Micro-Machined Piezoelectric Structures" by B. Jia and T.W.A. Blad, D. Farhadi Machekeposhti, R.Kuppens and N. Tolou.

Quantifying the Heat Affected Zone in Laser Micro-Machined Piezoelectric Structures

B.Jia* and T.W.A. Blad*, D. Farhadi Machekposhti, P.R. Kuppens and N. Tolou

*Both authors contributed equally

Abstract—As a manufacturing method for fast prototyping of MEMS (Mechanical Electro Micro System), laser micro machining with fast pulsed laser source has drawn great attention. Yet the limited thermal damage has not been quantified precisely. A set of piezoelectric material has been processed under different sets of parameters from Taguchi process optimization. And the piezoelectric coefficient was measured for both laser cut and natural broken pieces as the indication of the piezoelectric property loss due to thermal damage, thus the Heat Affected Zone is quantified precisely. The lowest surface roughness of 755 nm was obtained and no obvious piezoelectric property loss was found after one Taguchi iteration. Furthermore, a beam micro-actuator was fabricated based on the optimal laser parameters found in this research.

Index Terms—Vibration energy harvesting, Piezoelectric materials, Heat affected zone, Laser micromachining.

I. INTRODUCTION

PIEZOELECTRIC materials exhibit a coupling between the mechanical and electrical domains which makes them well suited for sensing and actuation. One advantage of piezoelectric transducers is their retained efficiency when miniaturized [1]. On this scale, applications include micro-surgery, micro-positioning stages, wireless sensor networks and micro-energy harvesters. Moreover, piezoelectric materials make excellent candidates for distributed sensing and actuation applications in compliant mechanisms. Research in these fields is often of an experimental nature, which inevitably requires the design and fabrication of numerous prototypes.

Due to their high coupling factors, piezoelectric ceramics are the most commonly used. The brittle properties of the ceramics, however, limit the use of conventional cutting and grinding machining at the small scale. Traditionally, the manufacturing of miniaturized sensors and actuators from piezoelectric material is done with processes such as lithography and chemical vapor deposition. These processes usually have a very long cycle time, making each iteration during prototyping very time consuming. An alternative to these methods may be laser micro-machining, which has the potential to shift the prototyping time scale for miniaturized devices from months to minutes. Therefore, laser micro-machining may allow for rapid prototyping of miniaturized piezoelectric devices.

The material removal of laser micro-machining is achieved by ablation process which is thought to be a combination of main steps: energy absorption, energy transfer and material removal [2]. The chemical connections in the material are directly broken by the absorption of high energy photons which results in the detachment of micro particles [3]. During this process, heat that is generated as a result of ablation is diffused into

surrounding material through conduction. This results in a heat affected zone (HAZ) where material properties have been altered.

When laser micro-machining of piezoelectric material is considered, temperatures above the Curie temperature (typically 200 – 400 °C [4]) may be reached in the HAZ. As a result, the piezoelectric properties may be lost locally. When the length scales of the piezoelectric structures are in the order of the HAZ dimensions, the performance of the device may be severely reduced. Especially during the prototyping of miniaturized piezoelectric sensors and actuators this is a problem as it may lead to non-functional devices.

Prior art on the quantification of the dimensions and effects of the HAZ in laser micro-machining of piezoelectric structures is mostly limited to visual inspection of color changes of the material surface [5]–[7]. Reduced performance as a result of laser micro-machining with a 355 nm YAG laser were reported by Zeng et al. (2004) [8]. It was found that the piezoelectric properties were reduced as a result of the loss of Pb and the existence of a pyrochlore phase. The solution proposed in this paper was the annealing at 1150 °C under PbO-controlled environment for 1 h. Lam et al. (2013) [9] investigated the machining of PMN-PT single crystal with a 355 nm YAG laser. The main conclusion was that the piezoelectric properties were reduced in an area of about 50 μm from the cutting line. Furthermore, it was shown that a narrower cut can be obtained by using less power per pulse, and a higher amount of repetitions. In Nadig et al. (2013) [10], [11] it was observed that the piezoelectric properties of bulk PZT-5H were lost entirely after laser micromachining with a 355 nm UV laser. The smallest features in this design were 125 μm with a thickness of 500 μm. Another attempt resulted in successful fabrication of these features from PZT-4A, which was presumed to be a result of the higher curie temperature of the material. On the contrary, Kim et al. (2008) reports no significant loss of macroscopic performance after machining features of 500 μm with a 1064 nm YAG laser. This result was found to be consistent with a previous study [12] where the piezoelectric properties of PZT were found to be unaffected as a result of femtosecond laser-machining (FLM). In that study, however, it was argued that substantial HAZ effects were expected for lasers with pulse durations in the order of nanoseconds.

The objective of this research is to investigate the effects of

the laser parameters on the HAZ in laser micro-machined piezoelectric structures. This will lead to insights that could aid in the development of a novel design guidelines for the laser micro-machining of piezoelectric structures.

Part II will present the designs of the piezoelectric actuator and sensor test pieces and the methods used for the manufacturing. This will include the selection of the laser parameters, selection of the array, cleaning the piezoelectric material and testing the capacitance and d_{33} piezoelectric coefficients. The results of the experimental tests will be presented in chapter III and discussed in chapter IV. Furthermore, the discussion will include an example of how these results can be integrated in a micro-compliant mechanisms with distributed actuation. Lastly, the most important conclusions will be summarized in part V.

II. METHOD

Laser micromachining processes remove material through the ablation of the target material as a result of the laser energy. Associated with the laser-material interaction is the conduction of heat through the target material. This may result in a *heat affected zone* in which the material properties are altered. When the fabrication of miniaturized piezoelectric sensors or actuators is considered, temperatures above the Curie temperature of the material may be reached. As a result, the piezoelectric properties, and thereby the performance of the device, may be severely reduced. In this research, piezoelectric test structures will be manufactured using a laser micro-machining process to quantify the resulting HAZ. This is illustrated in Fig. 1.

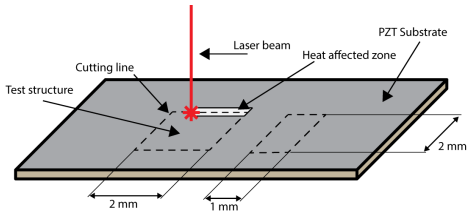


Fig. 1: Laser micro-machining of piezoelectric structures results in a HAZ. This research aims to quantify this HAZ through measurement of piezoelectric properties.

First, laser parameters will be selected using the method of orthogonal arrays. With these parameters, test structures will be manufactured from a plate of piezoelectric material by laser micro-machining. Each test structure will be manufactured individually and numbered. Next, the test structures are cleaned using an ultra-sonic cleaner while immersed in isopropyl alcohol. Finally, the capacitance, piezoelectric strain coefficient and the surface roughness of the side walls are measured. The measured piezoelectric strain coefficients are compared to theoretical values from datasheets to quantify the HAZ. Using these measurements, the effects of the laser parameters on the manufacturing of piezoelectric structures is quantified.

TABLE I: Overview of material and geometrical parameters used in the experiment. The resulting properties of the test structure were calculated using Eq. 1-3.

| | Parameter | Symbol | Value |
|----------|-----------------------|--------------|------------------------|
| Material | Type | | PIC252 |
| | Curie temperature | T_c | 350 °C |
| | Elastic modulus | E | 62 GPa |
| | Relative permittivity | ϵ_r | 1750 |
| | Density | ρ | 7.8 g cm ⁻³ |
| Geometry | Length | L | 10 mm |
| | Width | w | 1 mm |
| | Thickness | h | 100 μ m |
| | Capacitance (square) | C_p | 620 pF |
| | Capacitance (beam) | C_p | 310 pF |

A. Material and geometry

The piezoelectric structures are squares with the dimensions of 2 mm \times 2 mm and beams of 2 mm \times 1 mm. The test structures are expected to be sensitive to material degradation in the HAZ due to the small dimensions. The piezoelectric material that will be used are plates of PIC 252 from PI ceramics with a thickness of $t = 100 \mu\text{m}$. The Curie temperature of this material is 350 °C and the relative permittivity is $\epsilon_r = 1750$ [4]. The expected capacitances, C_p , of the test structures were calculated by the following equation.

$$C_p = \frac{\epsilon_r \epsilon_0 A}{t} \quad (1)$$

Where ϵ_r is the relative dielectric constant, ϵ_0 the permittivity of free space, A the electrode surface area and t the thickness of the piezoelectric material. The results are a capacitance of 620 pF for the squares and a capacitance of 310 pF for the beams. The material parameters and geometries are summarized in Table I.

B. Manufacturing procedure

The material is fixed on a ceramic substrate which is fixed by the vacuum extractor from beneath. A gap between substrate and sample is created by adding substrate material of 1 mm thickness at all edges, in order to prevent the accumulation of thermal energy at the bottom of the sample.

A Spectra-Physics Talon 355-15 diode pumped solid-state (DPSS) UV laser system with a wavelength of 355nm and maximum power of 15 watts at 50 kHz is adapted in this project. The maximum frequency is 500 kHz with pulse width 35ns. A BOFA extractor and filter is integrated in order to exhaust fumes. The laser beam delivery including energy attenuator, mirrors and steering mechanism. The optical steering is achieved by a Galvo head from Rhothor with a scan range of 46x46mm and focal length of 100mm. An overview of the setup is illustrated in Fig. 2.

The X-Y stage has a range of 80mm square with 1 μ m effective resolution. The laser beam scanning motion is done by a laser deflection systems based on the Lorentz force motors with internal active optical feedback in order of dramatically reducing sensitivity to external noise. Galvo head had the range of 46x46mm with local length of 100mm, the writing speed is 1300cm per second maximum.

All the test pieces were cleaned by using an ultra-sonic cleaner while immersed in isopropyl Alcohol [13].

C. Laser parameter selection

The three laser parameters that were controlled in this experiment were the diode current, A , laser pulse frequency, f , and the overlap, O . These parameters were selected because the diode current is directly related to laser power, and the pulse width varies depending on the frequency in the configuration of the laser system. The overlap is related to the scanning speed, v , by the following relation.

$$v = f \cdot r \cdot (1 - O) \quad (2)$$

Where r is the spot size of the laser. The method that will be used for the selection of the process parameters is the orthogonal array method, which finds its origin in the Taguchi method [14]–[16]. In this method, *orthogonal arrays* are used to study the relation between process parameters and an objective function. For each process parameter, a finite number of values is selected called the *level settings*. We adapt three variables with three levels for each variable. The combinations of the level settings of different parameters are arranged into orthogonal arrays, which ensure that every pair of parameter levels occurs an equal amount of times. Due to this pair-wise balancing of level settings, the effects of multiple process parameters can be studied simultaneously without distorting the effects of individual process parameters. As a result, the orthogonal array method allows the maximum amount of information to be derived by using the fewest experiments [17].

Initially, the applied energy of each shot was fixed as constant which is the maximum value of the laser, which will decrease the variant output from laser pulses, at the same time the trend between thermal damage and output power is more obvious to be observed. The lower boundary of the range of the controlled parameters was set such a reproducible cut-through would be achieved for every combination. These values were

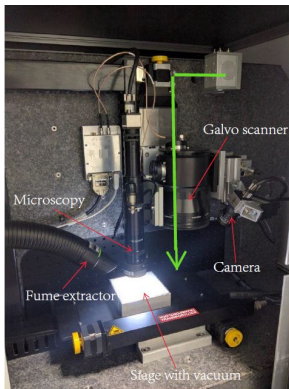


Fig. 2: Laser beam delivery setup

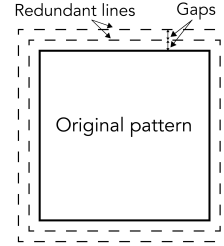


Fig. 3: Schematic representation of redundant lines and separating gaps used in laser micro-machining. These features are added to help the laser move into the workpiece.

empirically determined to be $A = 6A$, $A = 20\text{kHz}$ and $A = 70\%$. The upper boundary of the range was set at the maximum settings of the machine, which were $A = 7A$, $A = 30\text{kHz}$ and $A = 90\%$. This range is divided into three levels for every factor.

A second experiment was conducted variant energy pulses which is no long fixed as constant, meaning the pulse energy varies depending on frequency and using a narrower range of the controlled parameters. This will decrease the overall energy applied in order to find the optimal parameter sets in a lower energy regime. Again, the lower boundary was set to $A = 6A$, $A = 15\text{kHz}$ and $A = 60\%$, such that every experiment would result in cut-through. The upper boundary of the range was set at $A = 7A$, $A = 25\text{kHz}$ and $A = 80\%$, which was chosen because .

During both experiments, the other parameters were fixed as suggested by prior art [18]. They include the wavelength, pulse width, number of redundant lines and gap size between those lines. Redundant lines are often used in laser micro-machining in order to help the laser beam move into the work piece . In Fig. 3 the redundant lines and gaps are depicted schematically. Here, 3 redundant lines were used with a gap size of $20\mu\text{m}$ which was suggested in [19], which corresponds to the laser spot diameter of the laser beam. A complete overview of the level settings for the controlled parameters and the values of the fixed parameters is shown in Table II.

D. Measurement procedure

After cleaning, the capacitance and dielectric loss coefficient of the piezoelectric structures was measured using an Agilent 4263B LCR meter at 1 kHz. The piezoelectric charge constant, d_{33} was measured using a PiezoTest PM300 Berlincourt type d_{33} meter. The piezoelectric charge coefficient measurements were conducted twice for each test structure. Between the two measurements the sample was flipped such that both a positive and a negative value was obtained for the piezoelectric charge constant.

TABLE II: Overview of parameters used in this research

| Symbol | Factor name | Level 1 | Level 2 | Level 3 |
|--------|-------------------|---------|---------|---------|
| A | diode current [A] | 6.0 | 6.5 | 7.0 |
| B | frequency[KHz] | 20 | 25 | 30 |
| C | overlap [%] | 70 | 80 | 90 |

| Symbol | Factor name | Level 1 | Level 2 | Level 3 |
|--------|-------------------|---------|---------|---------|
| A | diode current [A] | 6.0 | 6.5 | 7.0 |
| B | frequency[KHz] | 15 | 20 | 25 |
| C | overlap [%] | 60 | 70 | 80 |

The surface roughness of the side walls of the samples were measured using a white light interferometer (Bruker Nano Surfaces Division), and was processed by integrated software of (Vision 64). For the measurement, the R_a value is measured over the whole side wall area. This value measures the deviations from the mean of the roughness profile and is corrected for tilt angle. The surface roughness measurements are conducted three times in order to limit random errors.

The surface is considered as non-periodic profile instead of conventional laser manufacturing profile as the result shows surfaces under specific settings are non-periodic where laser path is no longer obviously existed.

Finally, the samples were inspected using a Scanning Electron Microscope (SEM) from Jeol JSM-6010LA.

E. Data analysis

The controlled parameters were analyzed for each level setting by taking the average of the measured properties of all the test structures manufactured with that particular level setting. This resulted in 9 averages for the surface roughness and the piezoelectric charge constant. The effects of the individual controlled parameters is given by the variance between the three averages for that particular control parameter. For more information on this method we refer the reader to [17].

TABLE III: Application of the orthogonal array result

| Mean value of one parameter level |
|-----------------------------------|
| $A_1 = \text{Set}(1 + 2 + 3) / 3$ |
| $A_2 = \text{Set}(4 + 5 + 6) / 3$ |
| $A_3 = \text{Set}(7 + 8 + 9) / 3$ |
| $f_1 = \text{Set}(1 + 4 + 7) / 3$ |
| $f_2 = \text{Set}(2 + 5 + 8) / 3$ |
| $f_3 = \text{Set}(3 + 6 + 9) / 3$ |
| $O_1 = \text{Set}(1 + 6 + 8) / 3$ |
| $O_2 = \text{Set}(2 + 4 + 9) / 3$ |
| $O_3 = \text{Set}(3 + 5 + 7) / 3$ |

F. Fabrication of piezoelectric beam micro-actuator

Using the manufacturing procedure described in the previous section and the parameters that were found to result in a

minimal heat affected zone, a micro-scale piezoelectric actuator/sensor was fabricated. The device consists of a piezoelectric beam with a length of 5 mm and a width of 100 μm . The electrode layer on the top side of the beam was removed along a 30 μm wide line over the total length of the beam. A section of the design is illustrated in Fig. 4.

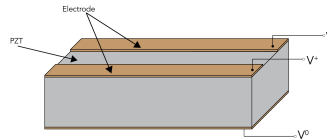


Fig. 4: Schematic indication of the design of an in-plane piezoelectric beam micro-actuator.

By applying a voltage across the terminals, the beam can be used as an in-plane micro-actuator. Alternatively, the device can be used as a sensor by measuring the voltage across the terminals to sense the deflection of the beam. The structure could also be used as a resonance energy harvester which would operate in the natural frequency of the beam, ω , that can be estimated by the following equation [20].

$$\omega = 2\pi f = \sqrt{\frac{k}{\frac{33}{140}m}}, \quad (3)$$

In this formula, m is the mass of the test structure and k is the stiffness which can be approximated by linear beam theory.

$$k = \frac{3EI}{L^3} = \frac{Ewt^3}{4L^3}, \quad (4)$$

Where E is the elastic modulus of the material, I is the moment of inertia, and L , w , t are the length, width and thickness, respectively. For the proposed beams, a mass of $m = 0.39 \text{ mg}$ and a stiffness of $k = 12.4 \text{ N m}^{-1}$ were estimated. As a result, the resonance frequency of the beam was estimated to be 5.64 kHz.

III. RESULTS

The results are listed in Table IV.

As can be seen in the table the smoothest surface had a value of $R_a = .755 \mu\text{m}$ and was obtained by parameters of set 4. And based on the parameters of set 4, a micro-beams were successfully manufactured and illustrated in Fig. 5a. The resulting beam had a tapered shape, where the width of the top side was measured at 79 μm and the bottom side at 109 μm . As shown in Fig5a the two sides of the beam are covered with different types of electrode materials. And the yellow side (left) of the beam, the electrode surface is separated by a line of laser engraving which was tested by a resistance measurement.

TABLE IV: Results of the measurements and orthogonal array method. Surface roughness measurements of a) experiment 1 and b) experiment 2, electrical properties of the test pieces from c) experiment 1 d) experiment 2, mean value of per parameter of surface roughness

| (a) surface roughness of experiment 1 | | | | | | | (b) surface roughness of experiment 2 | | | | | | | | |
|---------------------------------------|---|---|---|-----------|-------|-------|---------------------------------------|------------|---|---|---|-------|-------|-------|---------------------------|
| Set number | A | B | C | Power (W) | 2x1mm | 2x2mm | Average (μm) | Set number | A | B | C | 2x1mm | Power | 2x2mm | Average (μm) |
| 1 | 1 | 1 | 1 | 4.434 | 4.24 | 3.918 | 4.176 | 1 | 1 | 1 | 1 | 0.910 | 1.12 | 0.840 | 0.875 |
| 2 | 1 | 2 | 2 | 3.405 | 5.23 | 4.459 | 3.932 | 2 | 1 | 2 | 2 | 1.633 | 1.24 | 1.143 | 1.388 |
| 3 | 1 | 3 | 3 | 4.718 | 6.44 | 5.242 | 4.980 | 3 | 1 | 3 | 3 | 0.864 | 2.25 | 0.877 | 0.870 |
| 4 | 2 | 1 | 2 | 3.589 | 4.02 | 3.424 | 3.506 | 4 | 2 | 1 | 2 | 0.759 | 1.35 | 0.751 | 0.755 |
| 5 | 2 | 2 | 3 | 6.690 | 6.29 | 3.620 | 5.155 | 5 | 2 | 2 | 3 | 0.885 | 1.73 | 0.939 | 0.912 |
| 6 | 2 | 3 | 1 | 6.230 | 3.24 | 2.966 | 4.598 | 6 | 2 | 3 | 1 | 0.659 | 2.42 | 0.860 | 0.759 |
| 7 | 3 | 1 | 3 | 4.436 | 5.57 | 4.142 | 4.289 | 7 | 3 | 1 | 3 | 0.796 | 1.60 | 1.172 | 0.984 |
| 8 | 3 | 2 | 1 | 7.549 | 6.61 | 6.310 | 6.929 | 8 | 3 | 2 | 1 | 0.828 | 1.96 | 1.293 | 1.060 |
| 9 | 3 | 3 | 2 | 6.052 | 8.06 | 8.327 | 7.189 | 9 | 3 | 3 | 2 | 1.254 | 2.88 | 1.127 | 1.190 |

| (c) Electrical properties of experiment 1 | | | | | (d) Electrical properties of experiment 2 | | | | |
|---|------------|-------------|----------------------|------------------------|---|------------|-------------|-------------------------|-------------------------|
| Identification | Dimensions | Capacitance | δ coefficient | d_{33} value | L.d. | Dimensions | Capacitance | Positive d_{33} value | Negative d_{33} value |
| 1 | 2 x 2 mm | 510 pF | 0.0213 | 172 pC N ⁻¹ | 1 | 2 x 2 mm | 497 pF | 180 pC N ⁻¹ | -163 pC N ⁻¹ |
| 2 | 2 x 2 mm | 520 pF | 0.0213 | 176 pC N ⁻¹ | 2 | 2 x 2 mm | 500 pF | 170 pC N ⁻¹ | -170 pC N ⁻¹ |
| 3 | 2 x 2 mm | 544 pF | 0.0353 | 150 pC N ⁻¹ | 3 | 2 x 2 mm | 498 pF | 168 pC N ⁻¹ | -170 pC N ⁻¹ |
| 4 | 2 x 2 mm | 512 pF | 0.0217 | 166 pC N ⁻¹ | 4 | 2 x 2 mm | 491 pF | 185 pC N ⁻¹ | -162 pC N ⁻¹ |
| 5 | 2 x 2 mm | 501 pF | 0.0283 | 153 pC N ⁻¹ | 5 | 2 x 2 mm | 504 pF | 170 pC N ⁻¹ | -161 pC N ⁻¹ |
| 6 | 2 x 2 mm | 497 pF | 0.0300 | 131 pC N ⁻¹ | 6 | 2 x 2 mm | 497 pF | 156 pC N ⁻¹ | -175 pC N ⁻¹ |
| 7 | 2 x 2 mm | 523 pF | 0.0315 | 162 pC N ⁻¹ | 7 | 2 x 2 mm | 514 pF | 152 pC N ⁻¹ | -151 pC N ⁻¹ |
| 8 | 2 x 2 mm | 502 pF | 0.0215 | 143 pC N ⁻¹ | 8 | 2 x 2 mm | 502 pF | 175 pC N ⁻¹ | -174 pC N ⁻¹ |
| 9 | 2 x 2 mm | 487 pF | 0.0319 | 132 pC N ⁻¹ | 9 | 2 x 2 mm | 514 pF | 164 pC N ⁻¹ | -167 pC N ⁻¹ |
| 1 | 1 x 2 mm | 265 pF | 0.0242 | 161 pC N ⁻¹ | 1 | 1 x 2 mm | 250 pF | 136 pC N ⁻¹ | -123 pC N ⁻¹ |
| 2 | 1 x 2 mm | 254 pF | 0.0272 | 111 pC N ⁻¹ | 2 | 1 x 2 mm | 257 pF | 119 pC N ⁻¹ | -166 pC N ⁻¹ |
| 3 | 1 x 2 mm | 232 pF | 0.0386 | 102 pC N ⁻¹ | 3 | 1 x 2 mm | 249 pF | 140 pC N ⁻¹ | -142 pC N ⁻¹ |
| 4 | 1 x 2 mm | 240 pF | 0.0223 | 114 pC N ⁻¹ | 4 | 1 x 2 mm | 255 pF | 117 pC N ⁻¹ | -124 pC N ⁻¹ |
| 5 | 1 x 2 mm | 220 pF | 0.0346 | 40 pC N ⁻¹ | 5 | 1 x 2 mm | 243 pF | 158 pC N ⁻¹ | -135 pC N ⁻¹ |
| 6 | 1 x 2 mm | 217 pF | 0.0264 | 52 pC N ⁻¹ | 6 | 1 x 2 mm | 252 pF | 146 pC N ⁻¹ | -122 pC N ⁻¹ |
| 7 | 1 x 2 mm | 242 pF | 0.0249 | 111 pC N ⁻¹ | 7 | 1 x 2 mm | 250 pF | 128 pC N ⁻¹ | -105 pC N ⁻¹ |
| 8 | 1 x 2 mm | 237 pF | 0.0250 | 85 pC N ⁻¹ | 8 | 1 x 2 mm | 254 pF | 111 pC N ⁻¹ | -121 pC N ⁻¹ |
| 9 | 1 x 2 mm | 217 pF | 0.0344 | 19 pC N ⁻¹ | 9 | 1 x 2 mm | 248 pF | 159 pC N ⁻¹ | -133 pC N ⁻¹ |
| Ref.1 | - | 548 pF | - | 155 pC N ⁻¹ | Ref.1 | - | 548 pF | 155 pC N ⁻¹ | -160 pC N ⁻¹ |
| Ref.2 | - | 595 pF | - | 149 pC N ⁻¹ | Ref.2 | - | 595 pF | 149 pC N ⁻¹ | -165 pC N ⁻¹ |
| Ref.3 | - | 891 pF | - | 162 pC N ⁻¹ | Ref.3 | - | 891 pF | 162 pC N ⁻¹ | -178 pC N ⁻¹ |

| (e) Mean value of surface roughness of experiment 1 | | | (f) Mean value of surface roughness of experiment 2 | | |
|---|-----------------------------|-----------------|---|-------------------------|-----------------|
| Per parameter level | Roughness (μm) | Ra(Max)-Ra(Min) | Per parameter level | Roughness μm | Ra(Max)-Ra(Min) |
| A ₁ | 4.362 | | A ₁ | 1.044 | |
| A ₂ | 4.419 | 1.773 | A ₂ | 0.809 | 0.269 |
| A ₃ | 6.135 | | A ₃ | 1.078 | |
| f ₁ | 3.990 | | f ₁ | 0.871 | |
| f ₂ | 5.338 | 1.599 | f ₂ | 1.120 | 0.249 |
| f ₃ | 5.589 | | f ₃ | 0.940 | |
| O ₁ | 5.234 | | O ₁ | 0.898 | |
| O ₂ | 4.875 | 0.423 | O ₂ | 1.068 | 0.170 |
| O ₃ | 4.811 | | O ₃ | 0.922 | |



(a) Beam with separated electrode **(b)** A one euro coin beside as a reference

Fig. 5: Resulting micro-beam with electrode removed in the centre along the length; manufactured with the laser parameters from set 4

IV. DISCUSSION

A. Surface roughness

The findings of best surface roughness is found under parameters of set 4, and the worst is at set 2. The SEM images in Fig 6 provide a visual comparison between these surface qualities. In a) there is material irregularly accumulated at the bottom of the work piece while the rest part of the cross section area show smooth and clean cut. However in b) the cut shape is straight and uniform along all the cross section area. A potential explanation of this phenomenon is the interaction between substrate material and pzt ceramic. The ablation threshold of substrate material is higher than the fluence of set 4 while lower than the fluence of set 2, which huge amount of heat is accumulated at the bottom for set 4 and created melted material while in set 2 laser directly cut through the whole pzt material

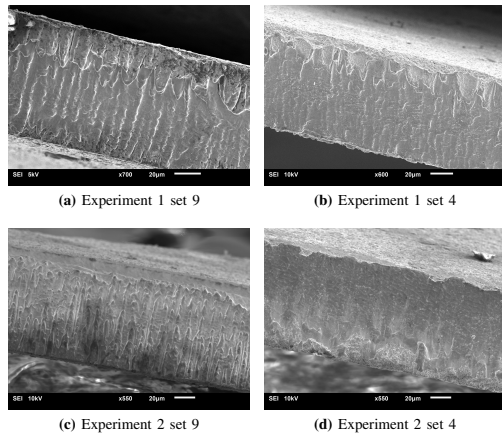


Fig. 6: SEM photomicro of side wall view for best and worst surface.

and into substrate material. Further experiment with variety of substrate materials can be conducted to further testify this reasoning.

It can be seen from the SEM images that the right image is obviously more clear and clean compared to the left figure, the laser foot path is less presented in the cross section area. From table IV e and f, it can be concluded from the results of experiment 1 that amongst the three controlled variables, the diode current (A) has the most severe effect on both the surface roughness and the piezoelectric coefficient loss. While the overlap has the least influence on the surface roughness. Furthermore, both sets of Taguchi optimization loops indicated the same trend in optimal setting, despite of the different levels of pulse energy.

B. HAZ

Generally, the HAZ is strictly related to the the amount of energy applied, specifically the energy introduced into per unit area material also known as fluence. From TabIV c, we can firstly conclude that the clear existence of thermal damage, because of the differences in d_{33} value of samples with different sizes under the same settings. Secondly, we can observe the clear trend of more piezoelectric property loss with more output power applied. However, the surface roughness is non-linearly affected by multiple factors of the process. The experiment prove can be found in measurements results. The set of minimum HAZ is not necessarily the same as the set with the smoothest surface. which means the optimal settings varies base on different criteria.

As the reference, there are also three sets of un-cut samples measured during the experiential. However, the results showed measured value is far lower than the theoretic value. This could be leaded by either limited accuracy of the piezo-measurement set-up, or the poor fabrication quality of the material. Yet this offset does not affect the outcome overall

trend obtained in this research.

It is needed to notice that for experiment sets with low energy applied, the d_{33} values are accidentally higher than the reference un-cut value, this could be leaded by the random error of measurement equipment. It could also be the instant temperature at the laser spot is near sintered temperature of PZT material while the laser beam acts as electromagnetic wave which change the piezoelectric coefficient of the samples [21], [22].

C. Methods

In a full set of typical Taguchi optimization, an outer ray is expected to be chosen, which is normally noise factors. However, for this particular project, noise factors are believed not controllable, nor cheap to control in other words. Thus there is no outer ray selected. Because noise factors are factors such as weather environment and humidity, which could be investigated by adding an outer array in further research.

Gas or water assistance are also considered not applicable in this research, but could be interesting in the further studies to eliminate the thermal damage.

V. CONCLUSION

In this research the influences by parameters of diode current, pulse frequency, overlap, along with the surface roughness and heat affected zone were investigated during the laser micro-machining of PZT material. The heat affected zone was quantified by comparing the measured values for the d_{33} coefficient to the theoretically predicted results. As shown in this study, the piezoelectric property of laser machined test structures can be reserved tremendously to 99% by using the optimized machining settings. And the by applying higher energy, the more piezoelectric property lost.

Side wall surface roughness can be significantly improved to reach 759 nm. While the setting for minimum HAZ is not subject to the setting for best surface roughness. Furthermore, it was demonstrated that a piezoelectric beam micro-actuator can be fabricated using the optimized machining settings.

REFERENCES

- [1] Takeshi Morita. Miniature piezoelectric motors. *Sensors and Actuators A: Physical*, 103(3):291–300, 2003.
- [2] S Karatodorov and M Grozeva. The effect of process parameters in femtosecond laser micromachining. *Bulg. J. Phys.*, 43:110–120, 2016.
- [3] Claas Willem Visser. *Fundamentals and applications of fast micro-drop impact*. Universiteit Twente, 2014.
- [4] Physik Instrumente. *Piezoelectric Ceramic Products*, 2016.
- [5] Dirk Herzog, Peter Jaeschke, Oliver Meier, and Heinz Haferkamp. Investigations on the thermal effect caused by laser cutting with respect to static strength of cfrp. *International journal of machine tools and manufacture*, 48(12):1464–1473, 2008.
- [6] Viboon Tangwarodomnukun, Jun Wang, and Philip Mathew. A comparison of dry and underwater laser micromachining of silicon substrates. In *Key Engineering Materials*, volume 443, pages 693–698. Trans Tech Publ, 2010.
- [7] V Tangwarodomnukun, J Wang, CZ Huang, and HT Zhu. An investigation of hybrid laser–waterjet ablation of silicon substrates. *International Journal of Machine Tools and Manufacture*, 56:39–49, 2012.
- [8] DW Zeng, K Li, KC Yung, HLW Chan, CL Choy, and CS Xie. Uv laser micromachining of piezoelectric ceramic using a pulsed nd: Yag laser. *Applied Physics A: Materials Science & Processing*, 78(3):415–421, 2004.

- [9] KH Lam, Y Chen, K Au, J Chen, JY Dai, and HS Luo. Kerf profile and piezoresponse study of the laser micro-machined pmn-pt single crystal using 355nm nd: Yag. *Materials Research Bulletin*, 48(9):3420–3423, 2013.
- [10] Sachin Nadig, Serhan Ardanuç, and Amit Lal. Planar laser-micro machined bulk pzt bimorph for in-plane actuation. In *Applications of Ferroelectric and Workshop on the Piezoresponse Force Microscopy (ISAF/PFM), 2013 IEEE International Symposium on the*, pages 152–155. IEEE, 2013.
- [11] Sachin Nadig, Serhan Ardanuç, and Amit Lal. Monolithic 2-axis in-plane pzt lateral bimorph energy harvester with differential output. In *Micro Electro Mechanical Systems (MEMS), 2015 28th IEEE International Conference on*, pages 1129–1132. IEEE, 2015.
- [12] Nitin Uppal, PANOS S SHIAKOLAS, and Shashank Priya. Micromachining of pzt using ultrafast femtosecond laser. *Ferroelectric Letters*, 32(3-4):67–77, 2005.
- [13] Lal A Nadig S, Ardanuç S. Planar laser-micro machined bulk pzt bimorph for in-plane actuation[c]//applications of ferroelectric and workshop on the piezoresponse force microscopy (isaf/pfm). *IEEE International symposium on the.*, 2013.
- [14] Kirby E D, Zhang J Z, Chen J C. Surface roughness optimization in an end-milling operation using the taguchi design method[j]. *Journal of Materials Processing Technology*, 2007.
- [15] Taguchi G. System of experimental design: engineering methods to optimize quality and minimize costs[m]. *UNIPUB/Kraus International Publications*, 1987.
- [16] J. Li and G. Ananthasuresh. A quality study on the excimer laser micromachining of electro-thermal-compliant micro devices. *J. Micromech. Microeng*, 2001.
- [17] Jun Li and GK Ananthasuresh. A quality study on the excimer laser micromachining of electro-thermal-compliant micro devices. *Journal of Micromechanics and microengineering*, 11(1):38, 2001.
- [18] M DAuria and N Tolou. Uv-laser cutting for silicon mems prototyping: Improving etching rate and quality. In *Proceedings of the 14th euspen International Conference, Dubrovnik, Croatia*, 2014.
- [19] N. Tolou M.D'Auria. Uv-laser cutting for silicon mems prototyping: Improving etching rate and quality. In *proceedings of the 14th euspen internation conference*, 2014.
- [20] Alper Erturk and Daniel J Inman. *Piezoelectric energy harvesting*. John Wiley & Sons, 2011.
- [21] Donny Wang, Yevgeniy Fotinich, and Greg P Carman. Influence of temperature on the electromechanical and fatigue behavior of piezoelectric ceramics. *Journal of applied physics*, 83(10):5342–5350, 1998.
- [22] Matthew W Hooker. Properties of pzt-based piezoelectric ceramics between-150 and 250 c. 1998.

Appendix B

Design process

"Design is not just what it looks like and feels like. Design is how it works"

Steve Jobs

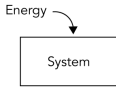
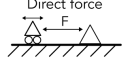
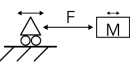
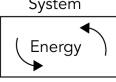

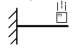
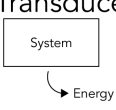
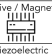
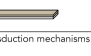

| Function | Approach | Strategy | Objective |
|---|--|--|---|
| Transfer  | Direct force  | Continuous contact | Maximize energy extraction through damping |
| | | Intermittent contact | Maximize energy storage and harvest upon release |
| | Inertial method  | Single stable position | Design for maximum potential energy at end positions |
| | | Multiple stable positions | Design energy barrier as high as possible that can be reached every cycle |
| | | Infinite stable positions | Achieve high velocities in free moving mass |
| Transmit  | Damping  | No storage Source → System → Transducer | Extract all energy every cycle: critically damped system |
| | | Storage Source → System → Transducer | Store energy in resonance Store energy in rotational components |
| | Impulse  | Frequency up-conversion | Achieve ringdown in secondary resonator between impulses |
| | | Snap deformation | Achieve high relative motion through large deformations |
| Transduce  | Commonly used transduction mechanisms | Electromechanical  Electrostrictive / Magnetostrictive  Piezoelectric  | Achieve high flux change Achieve large electric fields Achieve high active area |
| | Other transduction mechanisms | Other transduction mechanisms | |

Figure B.1: Categorization of solution space for the three functions of the vibration energy harvester by approach and strategy. For every strategy, an objective is formulated.

B

| Strategy | Embodiment | Solutions | | | | | | | | | | |
|----------------------------|---------------------------|-------------------------------|------------------------------|-------------------------------|--------------------------------|----------------------------------|-------------------------|-------------------------|--|--|--|--|
| Multiple stable positions | Bistable | Buckled plate | Buckled beam | Double beam with angle | Beam and magnetic attraction | Beam and magnetic repulsion | Ball and trajectory | Bridge of crossed beams | | | | |
| | Multi-stable | Trajectory | Magnetic attraction | Magnetic repulsion | Series stacking of bistability | Parallel stacking of bistability | | | | | | |
| Frequency up-conversion | Impact | Spring loaded impact | Mass hitting | Mass hitting elastic beam | Catch and release together | Mass hitting rotating structure | | | | | | |
| | Plucking / Scrape-through | Scrape through cantilever | Slide to side mass motion | Beam with magnetic attraction | Beam with magnetic repulsion | Rotational scrape through | Sliding over cantilever | Loaded pin | | | | |
| | Base-Impact | Mass hitting structure corner | Stable stop of base | Mass hitting base | Beam hitting end stop | | | | | | | |
| Piezoelectric transduction | d33 - mode | Interdigitated electrodes | Impact compression | | | | | | | | | |
| | d31 - mode | Clamped free out of plane | Clamped clamped out of plane | In plane cantilever | Bending pattern | Membrane | | | | | | |
| | d15 - mode | Shearing beam | | | | | | | | | | |

Figure B.2: Morphological chart of solutions within the selected strategies for the three functions of the vibration energy harvester. The solutions are categorized by embodiments.

Elimination of options

Magnets (X) (6)

Magnets are eliminated because their miniaturization is poor

Plucking (X) (5)

Plucking is unnecessary when combined with a multistable strategy and therefore removed.

Complex piezo patterns (X) (4)

Impact compression, clamped clamped bending, shearing and the bending line pattern are removed for complexity or infeasibility.

Other (X) (2)

Catch and resonate together and hitting a rotational structure are removed because they unnecessarily increase complexity.

Duplicates (X) (3)

The interdigitated electrodes and the multi-stable trajectory are slightly modified duplicates of the substrate cantilever and the bistable trajectory, and therefore not considered. The buckled plate is considered to be approximated by the bridge of crossed flexures, and is therefore omitted. Duplicates are considered in a later stage and may replace the original design.

Infeasible combinations

Membrane combinations (x) (24)

The membrane transduction mechanism does not combine feasibly with mass hitting a side wall, the mass hitting a base, and the elastic beam and the spring loaded impact.

Ball and trajectory combinations (x) (6)

The ball and trajectory does not have a bistable snap thus cannot utilize this strategy, and is infeasible with the base hitting an end stop.

Membrane with integrated transducer (x) (12)

The membrane impact option works best if the transducer is also a membrane and is integrated. 12 infeasible combinations are removed: x.

Stacking of bistability and snap behavior (x) (36)

The snap of base is the only transmit solution where the stacking of bistability will not just be a replication of two times the bistable behavior.

Figure B.3: Elimination criteria for structured elimination of solutions from the morphological chart.

| Strategy | Embodiment | Solutions | | | | | | | | | |
|--------------------------------|-------------------------------|--------------|----------|--------------------------|----------------------------|-----------------------------|------------------|---------------------------|--|--|--|
| | | Double plate | Embedded | Flexible beam with angle | Beam and supports attached | Beam and supports separated | Ball and magnets | Bridge of connected beams | | | |
| Multiple stable positions | Bistable | | | | | | | | | | |
| | Multi-stable | | | | | | | | | | |
| Frequency up-conversion | Impact | | | | | | | | | | |
| | Plucking / Scrape-through | | | | | | | | | | |
| | Base-Impact | | | | | | | | | | |
| Piezoelectric transduction | d33 - mode | | | | | | | | | | |
| | d31 - mode | | | | | | | | | | |
| | d15 - mode | | | | | | | | | | |

B

Figure B.4: Resulting morphological chart after elimination procedure. All combinations of the resulting solutions were sketched as a conceptual drawing

The remaining 59 combinations of solutions were sketched and can be seen in Fig. B.5 and Fig. B.6. From the sketches, 8 concepts were selected and assessed based on a set of assessment criteria that was drafted and can be found in Fig. B.8. The result of this assessment is shown in Fig. B.7. Based on the assessment, three concepts were selected for further investigation.

B

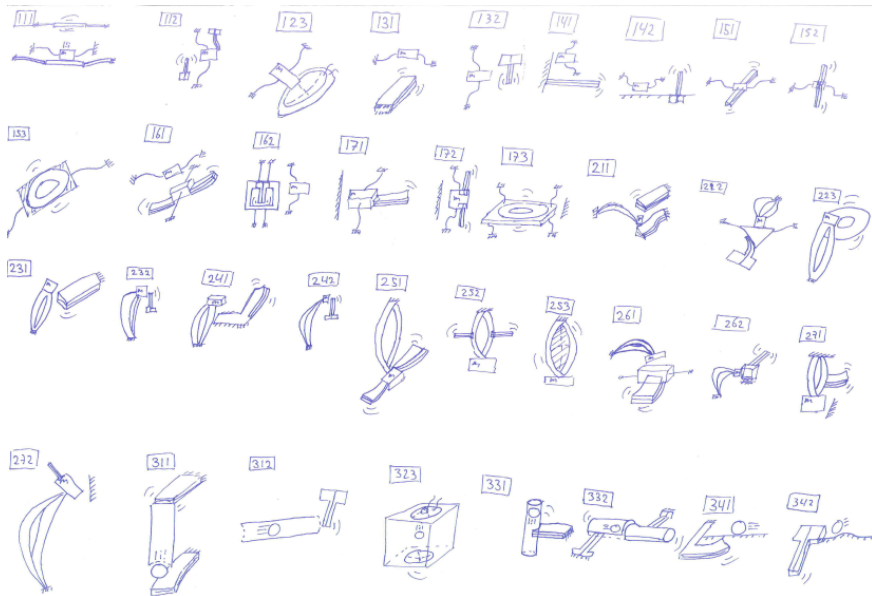


Figure B.5: First set of conceptual drawings.

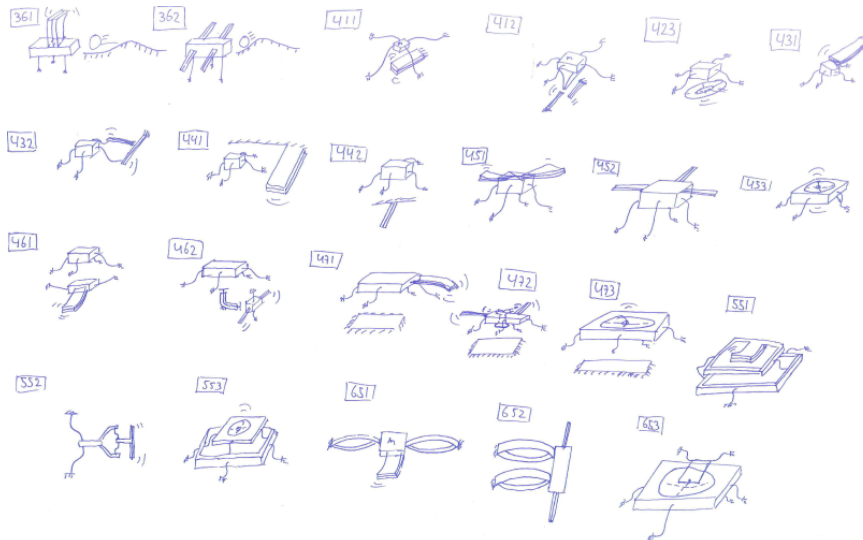


Figure B.6: Second set of conceptual drawings.

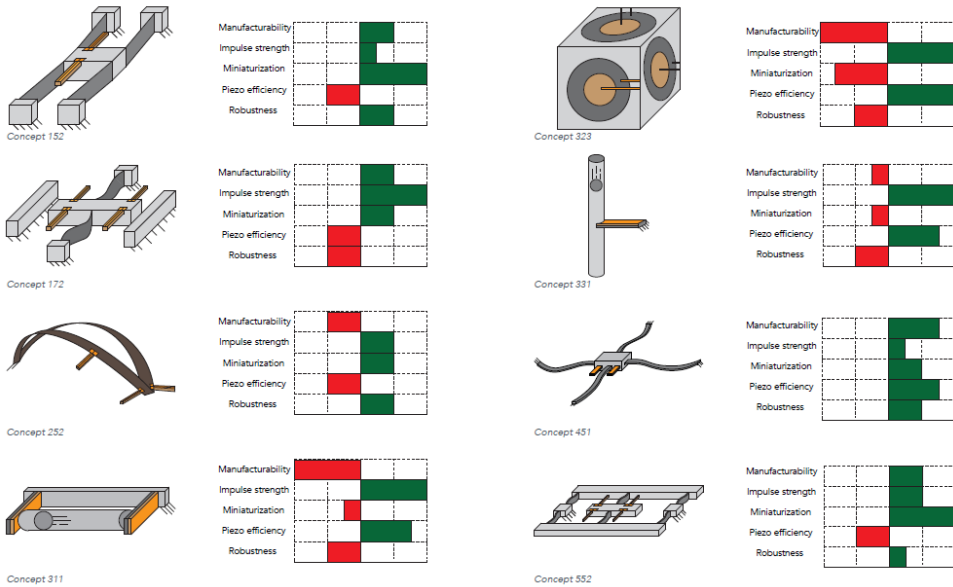


Figure B.7: Assessment of 8 selected concepts.

Manufacturability

Planar (+1.5)

Magnets are eliminated because their miniaturization is poor

Assembly (-1)

Plucking is unnecessary when combined with a multistable strategy and therefore removed.

Lamination (-0.5)

Impact compression, clamped clamped bending, shearing and the bending line pattern are removed for complexity or infeasibility.

Complexity (-0.5)

Catch and resonate together and hitting a rotational structure are removed because they unnecessarily increase complexity.

Impulse strength

Impact (+2)

Bistable snap (+1)

End stops (+0.5)

Piezoelectric efficiency

Impact on plate or membrane (+2)

Out of plane substrate cantilever (+1.5)

In plane separation of electrodes (+0.5)

Figure B.8: Assessment criteria for selected concepts.

B

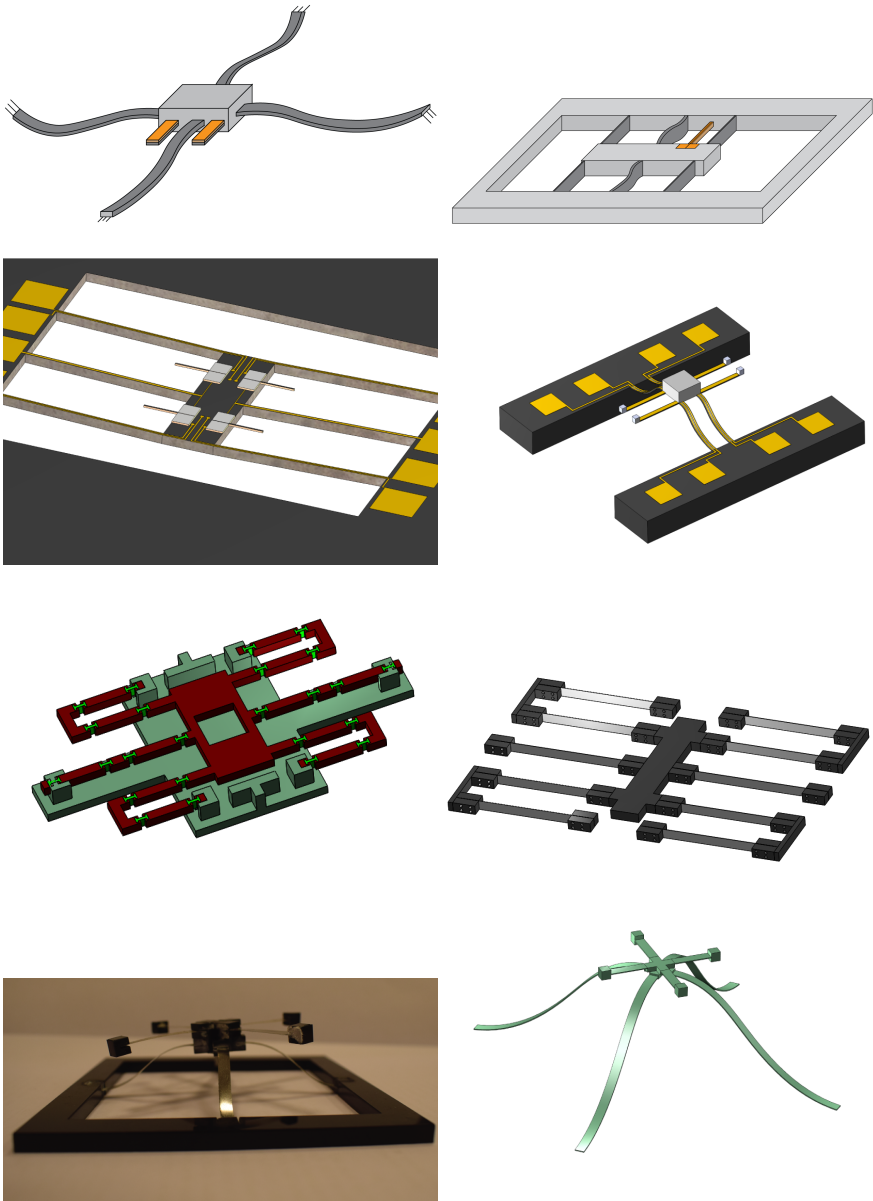


Figure B.9: Drawings, Solidworks models and prototypes of the most promising concepts.

Appendix C

Prototypes and practical work

"The trick to having good ideas is not to sit around in glorious isolation and try to think big thoughts. The trick is to get more parts on the table."

Steven Johnson

C.1 Introduction

Over the course of this project a number of prototypes were developed and fabricated. The practical work resulted in three functional vibration energy harvester systems, one experimental setup, two laser micro-machining projects and a number of components and parts. In this chapter, methods and materials and the resulting prototypes are presented.

C.2 Functional vibration energy harvester systems

In total, three series of prototypes of functional vibration energy harvester systems were manufactured. These systems were able to fulfill all the functions that make up a vibration energy harvester. Their design and manufacturing processes included the mechanical parts, the transducer and the electrical conditioning circuitry required to store and demonstrate the generated energy. The vibration energy harvesting systems that were generated are named the low-frequency resonant generator, the ball impact generator and the parametric frequency up-converter generator. Of the last prototype, the series includes three models (Mk.1, Mk.2 and Mk.3). Every prototype will be classified according to the classification developed in Table. 3.1, and have its working principles described briefly. Furthermore, manufacturing and assembly methods, design considerations, individual components, performance analyses and pictures of the prototypes will be discussed.

C.2.1 Low-frequency resonant generator

The first prototype that was developed was the low-frequency resonant generator (LFRG). This basic prototype was developed mainly to get a feeling for the working principles of an energy harvester in practice. The LFRG is basically a flexible cantilever with a heavy tip mass designed to have a resonance frequency of 2 Hz. The LFRG was equipped with a piezoelectric transducer from the flexible PVDF material. Therefore, the generator could generate output power over a large amplitude motion without breaking the transducer. The classification of the generator is given in Table. C.1.

| Function | Used strategy |
|-----------|---------------------|
| Transfer | Inertial - Resonant |
| Transmit | Non-coupled |
| Transduce | Piezoelectric |

Table C.1: Classification of low-frequency resonant generator.

Materials and methods

The mechanical harvesting element consists of a bilayer cantilever, a tip mass and clamps at the end of the cantilever. The bilayer cantilever is composed of a spring steel substrate layer bonded to a PVDF piezoelectric layer using Loctite super glue. Both the substrate and the piezoelectric material were manufactured using the laser-micro machining. The clamps were mounted at the ends of the bilayer cantilever and a block connector was pushed in one of the clamps from the other end such that one of the pins made contact with the electrode of the PVDF and another pin made contact with the substrate. The electrically connected cantilever without tip-mass can be seen in Fig. C.1. The whole assembly was fixed using super glue, and the mass was attached to the clamp at the other end of the cantilever. The materials, geometries and expected dynamic properties of the mechanical components are summarized in Tbl. C.2.



Figure C.1: Cantilever assembly of the LFRG prototype excluding proof mass.

| | Parameter | Value |
|----------|---------------------|----------------------|
| Material | Substrate | Stainless steel |
| | Piezo | PVDF |
| | Tip mass | Stainless steel |
| | Fixures | PMMA |
| Geometry | Free length | 30 mm |
| | Width | 7 mm |
| | Substrate thickness | 100 μm |
| | Piezo thickness | 110 μm |
| Dynamics | Stiffness | 40 N m^{-1} |
| | Tip mass | 64 g |
| | Eigenfrequency | 2 Hz |

Table C.2: Specifications of the LFRG prototype.

The electrical conditioning circuit of the energy harvester is shown schematically in Fig. C.2. The circuit consists of a full wave rectifier, a capacitor with capacitance, $C_e = 33 \text{ nF}$, a switch, an LED and two output terminals which can be used to measure the energy stored in the capacitor. When the device is excited the capacitor is charged. The capacitor can be discharged by flipping a switch which results in a bright flash of the LED.

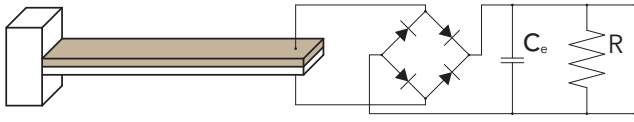
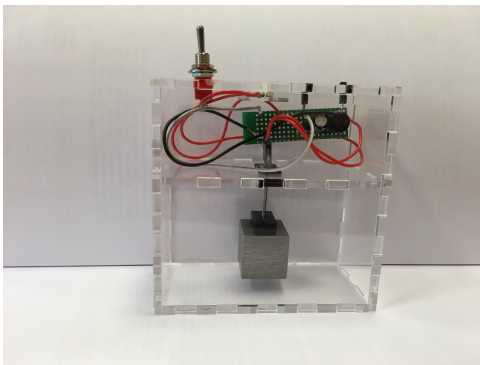


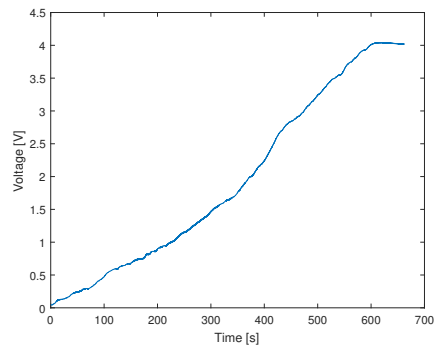
Figure C.2: **Harvesting circuit with full-wave rectifier followed by a smoothing capacitor, C_e , to obtain a constant rectified voltage over the resistive load, R .**

Result

The cantilever and electrical system were mounted in a PMMA casing, which resulted in the prototype shown in Fig. C.3. To measure the generated power, the capacitor was replaced with a larger capacitor of $11 \mu\text{F}$ and the voltage was recorded while shaking the prototype by hand. The charging of the capacitor to 4V took about 10 minutes. Back of the envelope calculations found that the energy output of the LFRG was about $0.3 \mu\text{W}$. Obviously, this prototype is a highly inefficient generator in all aspects, but the fabrication and testing of this prototype greatly helped to develop an intuitive feeling and practical understanding for the problems with harvesting energy from low-frequency vibrations. Furthermore, practical tips and tricks were learned that were used in the development of later prototypes.



(a)



(b)

Figure C.3: **Prototype of the LFRG (a) and voltage over capacitor while shaking device by hand (b).**

C.2.2 Ball impact generator

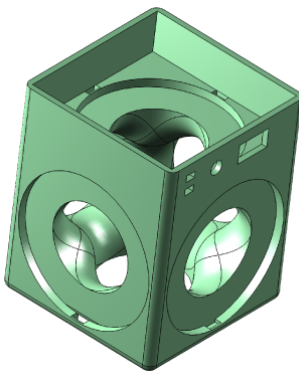
The second prototype that was developed was the ball impact generator (BIG). This prototype, inspired by the design of [21], was one of the alternative frequency-up conversion designs that was not selected for the final prototype. However, a prototype of this design was fabricated mainly out of interest for its working principle, and the unnerving desire of the author to tinker on a prototype. The BIG is a box with piezoelectric audio buzzers attached to the sides and metal balls rolling freely in the center. Upon shaking the device, the metal balls impact on the audio buzzers and thereby generate power. As a side-effect, a great deal of noise is generated. In Table. C.1, the classification of the generator strategy and the classification of the used frequency up-conversion method are given.

| Function | Used strategy |
|-----------|----------------------------------|
| Transfer | Inertial - Parametric |
| Transmit | Coupled - Frequency up-converter |
| Transduce | Piezoelectric |
| Coupling | LFO-HFO direct-impact type |

Table C.3: Classification of ball impact resonant generator, according to Table. 3.1 and Table xx.

Materials and methods

The housing of the BIG has the hollow structure shown in Fig. C.4 that was fabricated using 3d printing. This was the only manufactured parts, since the piezoelectric audio buzzers and metal balls were bought from a local hardware store. The parts were mounted in the casing using super glue, and the balls were placed in the middle, such that they could move freely. The materials, geometries and expected dynamic properties of the mechanical components are summarized in Tbl. C.2.



| | Parameter | Value |
|----------|-------------------------|-----------------|
| Material | Housing | PLA |
| | Piezo | PZT / Brass |
| | Balls | Stainless steel |
| Geometry | Ball diameter | 10 mm |
| | Buzzer diameter (brass) | 45 mm |
| | Buzzer diameter (piezo) | 30 mm |

Figure C.4: 3D model of the housing of the BIG prototype.

Table C.4: Specifications of the BIG prototype.

The electrical conditioning circuit of the BIG was identical to the electrical circuit used in the LFRG shown schematically in Fig. C.2. The only difference was that a bigger capacitor was used of $C_e = 125\mu\text{F}$.

Result

The BIG prototype is shown in Fig. C.3. To measure the generated power, the voltage was recorded while shaking the prototype quite rigorously by hand. From the figure can be seen that the charging of the capacitor to 5V took about 16 seconds. Back of the envelope calculations found that the energy output of the BIG was about $195\mu\text{W}$. Although this was a significant increase w.r.t the LFRG, the BIG still remained a highly inefficient generator. The most valuable lesson from the fabrication of the BIG was the insight that somewhat out-of-the-box generator concepts, like the BIG, could compete with the established cantilever concepts in terms of power generation per volume. Furthermore, it was learned that a BIG should never be applied in any application close to the ear without proper sound proof insulation.

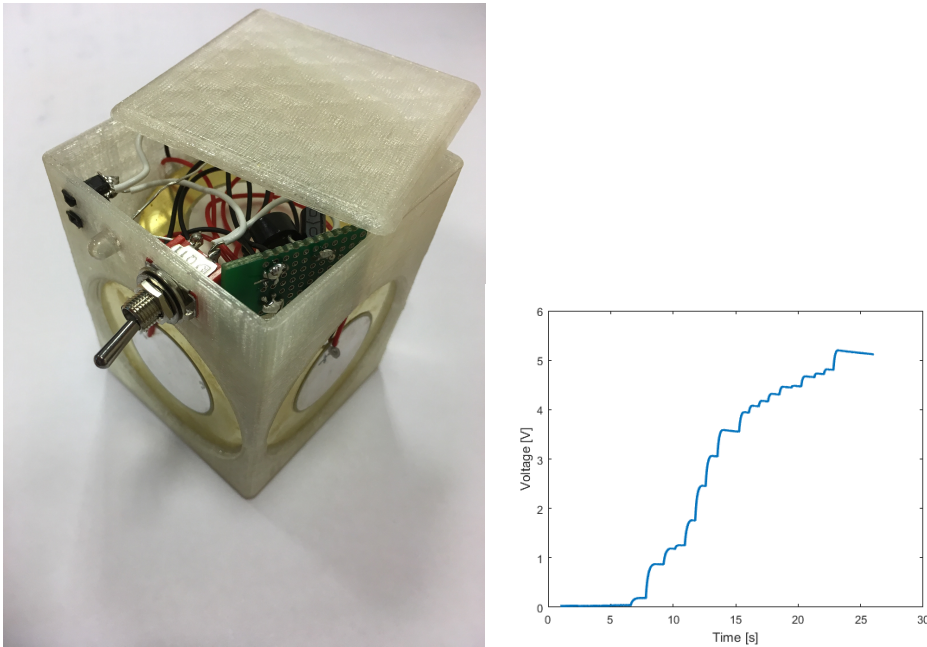


Figure C.5: Prototype of the BIG (a) and voltage over capacitor while shaking device by hand (b).

C.2.3 Parametric frequency up-converter generator

The parametric frequency up-converter generator (PFupCG), shown in Fig. C.6, is a non-resonant generator designed to harvest from low-frequency vibrations with an amplitude larger than its internal displacement limit. In the PFupCG an inertial mass is connected to the housing by a suspension with a bi-stable characteristic, and mechanical stops. Upon excitation by a driving motion with sufficient acceleration the inertial mass can snap out of one of its stable positions, pass its instable position and reach the displacement limit at the other side with considerable velocity. At the displacement limit the suspended mass will experience an impact on the mechanical stop, which will trigger an impulse response in the secondary oscillator such that it begins to vibrate in its own natural frequency. Energy is generated by a transducer harvesting from the relative motion between the inertial masses of the suspension system and the secondary oscillator. During a harmonic excitation the inertial mass snaps back and forth between the two stable positions, exciting the secondary oscillator on every impact and generating power.

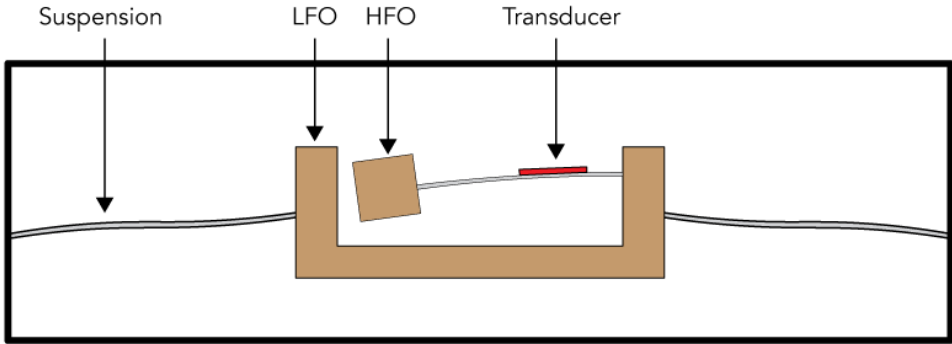


Figure C.6: Overview of the PFupCG architecture

| Function | Used strategy |
|-----------|----------------------------------|
| Transfer | Inertial - Parametric |
| Transmit | Coupled - Frequency up-converter |
| Transduce | Piezoelectric |
| Coupling | Base-LFO direct-impact type |

Table C.5: Classification of ball impact resonant generator, according to Table. 3.1 and Table xx.

Mk.1

The first version of the PFupCG was made from 3d printed housing, a laser machined shuttle and spring steel flexures. In the shuttle and the housing, slots of 0.2mm were designed and the spring steel flexures were attached in the slots using super glue. In the housing, a pre-loading mechanism was designed with which the pre-loading on the central flexures could be tuned. By turning the bolts, the bolt would push the mounting point of the central flexure inwards and the flexure would buckle. The other sets of flexures were fabricated under a very slight angle such that they would allow a small displacement of the shuttle and act as mechanical stops when loaded in tension. To finish the device, some assembled piezoelectric cantilevers identical to the one shown in Fig. C.1 were mounted on the shuttle. The result of the PFupCG Mk.1 is shown in Fig. C.7.

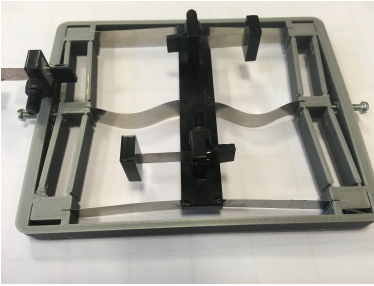


Figure C.7: **Prototype of the PFupCG Mk.1**

| | Parameter | Value |
|----------|---------------------|--------------|
| Material | Housing | PLA |
| | Flexures | Spring steel |
| | Shuttle | PMMA |
| Geometry | Flexure thickness | 0.1 mm |
| | Flexure free length | 45 mm |
| | Flexure width | 5 mm |

Table C.6: **Specifications of the PFupCG Mk.1.**

Mk.2

The second version of the PFupCG was constructed from PMMA parts and spring steel flexures. The parts were manufactured from 5 mm thick PMMA using laser machining. In the sides of the parts, tiny slots of 0.2mm thickness were designed as mounting parts for the flexures. The 0.05mm thick flexures were mounted in the slots and fixed with super glue. Finally, a 15 g proof mass made from aluminum was mounted on the central platform to create the high frequency oscillator. The pre-loading of the bistable flexures was done by moving the central parts together, and fixing them with super glue.

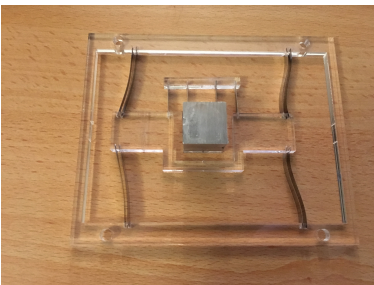


Figure C.8: **Prototype of the PFupCG Mk.2**

| | Parameter | Value |
|----------|--------------------------------|--------------|
| Material | Housing | PMMA |
| | Flexures | Spring steel |
| | Proof mass | Aluminum |
| Geometry | Flexure thickness | 0.1 mm |
| | Flexure free lengths (outside) | 40 mm |
| | Flexure free lengths (inside) | 15 mm |
| | Flexure width | 5 mm |

Table C.7: **Specifications of the PFupCG Mk.2.**

Laser-cut PMMA, stainless steel flexures and super glue are an excellent rapid prototyping method for compliant mechanisms. Therefore, many versions of the PFupCG Mk.2 were fabricated over the course of the project. However, many imperfections are induced by the gluing of the flexures which makes it virtually impossible to accurately calculate the stiffnesses of buckled flexures. Generally, the prototypes could exhibit stiffnesses of roughly 10 to 60% of the calculated stiffness.

Mk.3

The third and final version of the PFupCG was manufactured from aluminum parts and spring steel flexures. The 5 body parts and 4 flexure attachments were milled by hand and the flexures were fabricated by laser micro-machining. At both ends of each flexure, a 15 mm space with two holes was added to the free length to facilitate the clamp mounting. In the aluminum parts, holes were drilled and tapped with M3 thread such that they would align with the holes in the flexures. The flexures were mounted by clamping them between the part and a 2 mm thick plate of aluminum by means of M3 bolts. A PMMA baseplate was laser-cut as a mounting for the flexure attachments. Pre-loading was applied by mounting the flexure attachments to the baseplate with M3 bolts and nuts.

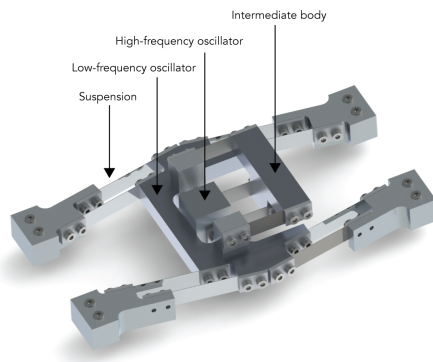


Figure C.9: Render of the PFupCG Mk.3 prototype.

| | Parameter | Value |
|----------|--------------------------------------|--------------|
| Material | Body parts | Aluminum |
| | Flexures | Spring steel |
| | Baseplate | PMMA |
| Geometry | Flexure thickness (outside) | 0.05 mm |
| | Flexure free length (outside) | 35 mm |
| | Flexure thickness (LFO-intermediate) | 0.2 mm |
| | Flexure thickness (intermediate-HFO) | 0.1 mm |
| | Flexure free length (inside) | 20 mm |
| | Flexure width | 10 mm |
| Dynamics | Total suspended mass | 140 g |
| | Mass intermediate body | 33 g |
| | Mass HFO | 26 g |
| | Eigenfrequency HFO | 20 Hz |

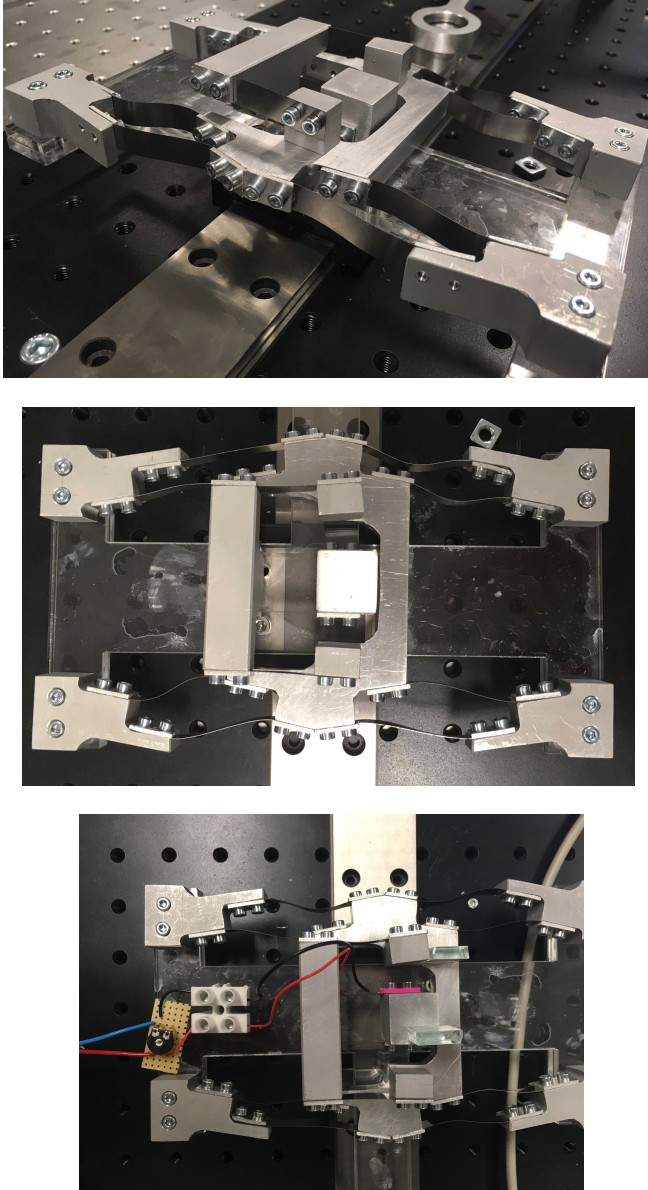
Table C.8: Specifications of the PFupCG Mk.3.

The manufacturing of this prototype took a total of two weeks and the most difficult part was the milling of the aluminum surfaces at a 10 deg angle. Due to the handwork, the holes on the outside of the body did not align properly with the holes in the designed flexures, and the prototype could not be assembled. To solve this problem, the whole prototype was measured, re-modeled in Solidworks and 8 new, unique outside flexures were manufactured. These flexures fitted perfectly and the prototype could be assembled.

The transducer in this prototype was manufactured on top of one of the 0.1 mm thick flexures between the intermediate body and the HFO. A 110 μ m thick sheet of PVDF was attached to the flexure by epoxy. The top electrode of the PVDF sheet was removed over the width of the flexure in the middle by grinding.

Result

The result of the PFupCG Mk.3 prototype is shown in Fig. C.10. The prototype exhibits the desired bi-stable behavior but has a very slight preference for one of the stable points that is most likely caused due to the small variation in lengths of the outside flexures.



C

Figure C.10: Resulting prototype of the PFupCG Mk.3

C.3 Other manufacturing projects

Next to the functional energy harvesting systems, a crank-slider mechanism and two laser micro-machined prototypes were part of the practical work conducted throughout this project. For the laser micro-machining projects, a collaboration was formed with Boran Jia, who was responsible for operating the laser and selecting the proper parameters. This collaboration resulted in two prototypes: the piezoelectric micro-beam actuator and a micro-scale demonstrator of the PFupCG.

C

C.3.1 Experimental setup

The experimental setup consists of a frequency generator, a measurement system and the PFupCG prototype and is shown in Fig. C.11. The frequency generator is custom-built and consists of a crank-slider mechanism driven by an electro-motor. The frequency of the driving vibration can be controlled by controlling the voltage fed to the motor, and the amplitude of the driving vibration is fixed at 25 mm by the kinematics of the crank. The measurement system consists of three laser interferometer position sensors from (Brand X, type Y). Three positions are measured simultaneously: the slider position, y , the position of the LFO, x_1 , and the position of the HFO, x_2 . The relative positions of the oscillators can be found by subtracting the position of the slider such that $z_1 = x_1 - y$ and $z_2 = x_2 - y$ give the relative positions of the LFO and HFO, respectively.

Materials and methods

The frequency generator system consists of an electro motor that was obtained from the meethop, and a crank-slider mechanism. The parts of the crank-slider mechanism were milled by hand and roller bearings were press-fitted in the mountings. The crank has a 25 mm arm and was connected to the axis of the electro motor by a screw.

Result

The resulting experimental setup is shown in Fig. C.11. The frequency of the input vibration can be controlled by controlling the output voltage of the the source.

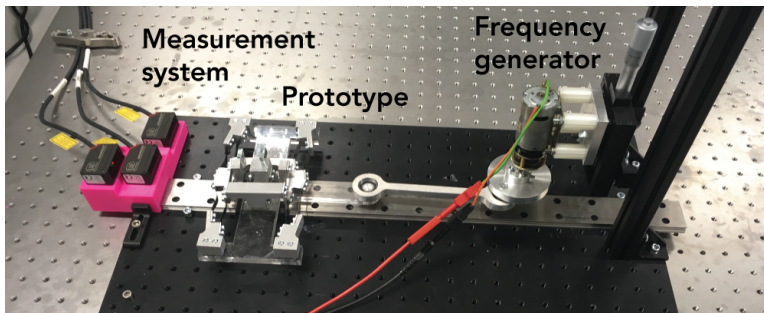


Figure C.11: Experimental setup consisting of crank-slider mechanism, laser position sensors and the PFupCG prototype.

C.3.2 Piezoelectric micro-beam actuator

The piezoelectric micro-beam actuator was one of the concept designs for the piezoelectric transducer of the PFupCG, as shown in Fig. 3.15. Especially for miniaturized planar generators this design could provide an alternative to the out-of-plane cantilevers. Since the electrodes are placed on the top and bottom instead of the sides, this concept could theoretically allow much easier micro-fabrication. Although the design was not selected, prototyping methods were explored for this manufacturing process.

Materials and methods

Piezoelectric material of the PZT-5H family with a thickness of $100\mu\text{m}$ was ordered from PI ceramic and laser micro-machined into a $200\mu\text{m}$ wide cantilever. Along the central axis of the cantilever, the electrodes were removed over a $40\mu\text{m}$ by micro-machining at a much lower power setting with the laser. Two bonding pads were cut at one side of the cantilever such that electrical connections could be made to the outside world.

Result

The result of the piezoelectric micro-beam actuator can be seen in Fig. C.12. Unfortunately, no successful tests were conducted with the prototype.

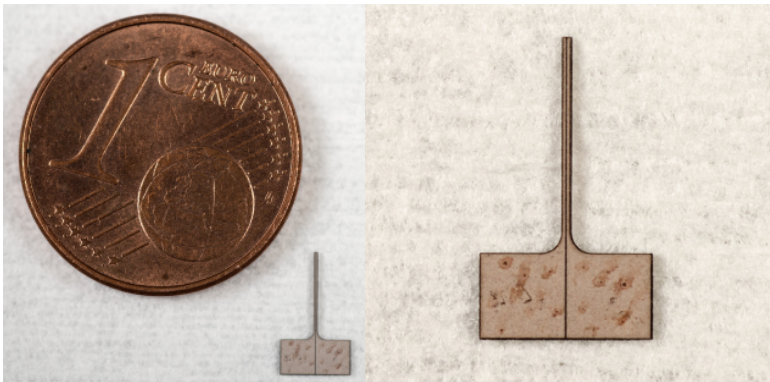


Figure C.12: Resulting prototype of the piezoelectric micro-beam actuator.

C.3.3 Micro-scale demonstrator

The second laser-micro machining project was a micro-scale demonstrator of the PFupCG concept. This project was conducted to demonstrate what a micro-scale version of the PFupCG could look like. The prototype is merely intended as a demonstrator and has no functional bi-stability.

Materials and methods

The demonstrator was manufactured from 0.2mm thick silicon wafer by laser micro-machining.

Result

The resulting prototype can be seen in Fig. C.13. In Fig. ?? the demonstrator is placed on a printed circuit board to demonstrate a how the device could be integrated in a possible application. The fabrication of a functional micro-scale prototype is one of the main targets for future research.

C

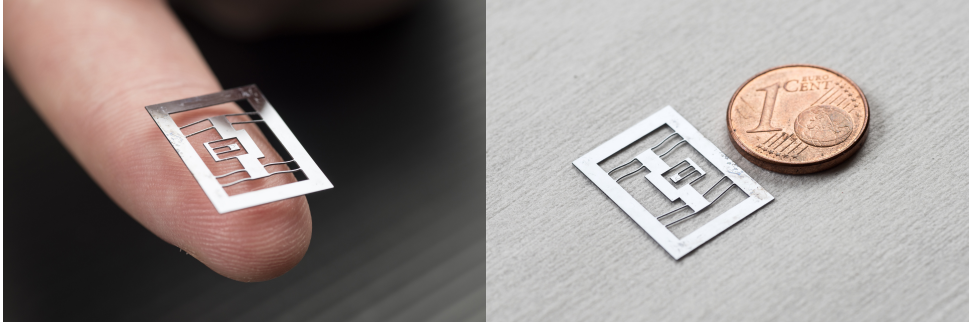


Figure C.13: Resulting prototype of the micro-scale PFupCG demonstrator.

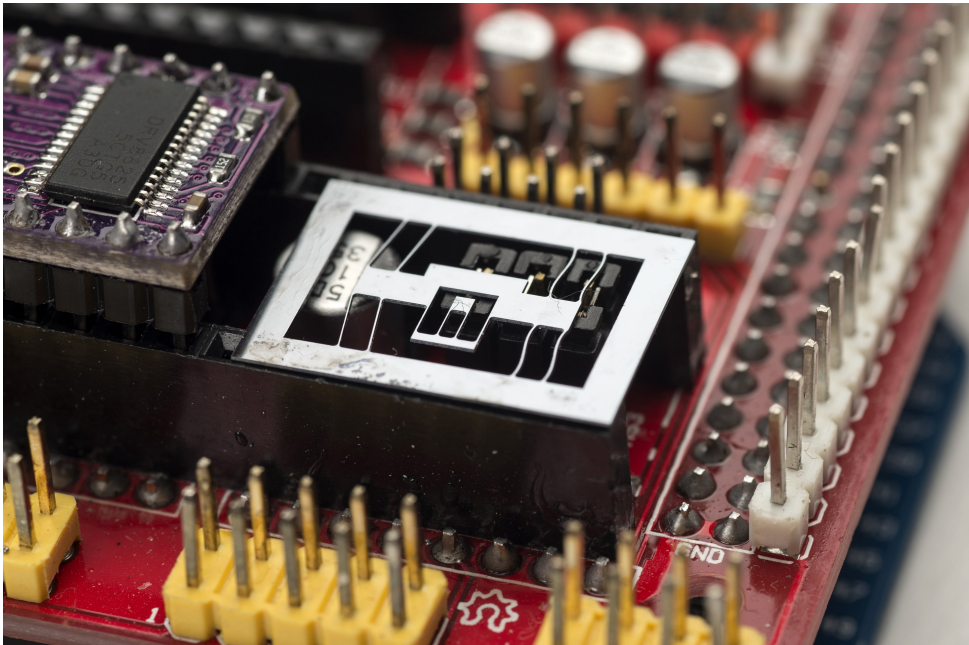


Figure C.14: Impression of integration of a micro-scale vibration energy harvester on a PCB.

Appendix D

Technical drawings of PFupCG

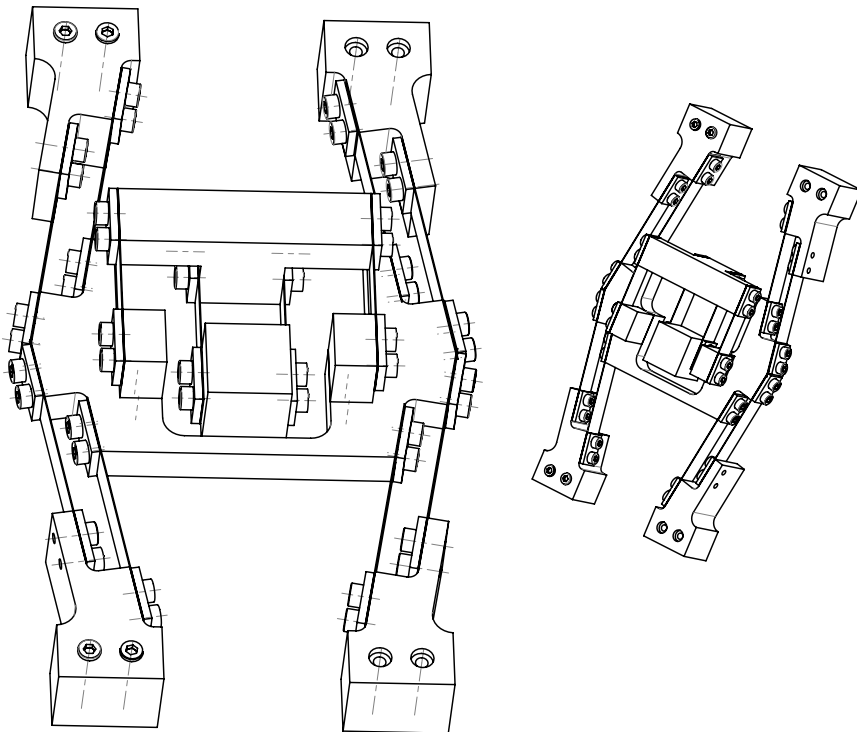


Figure D.1: Overview of PFupCG assembly

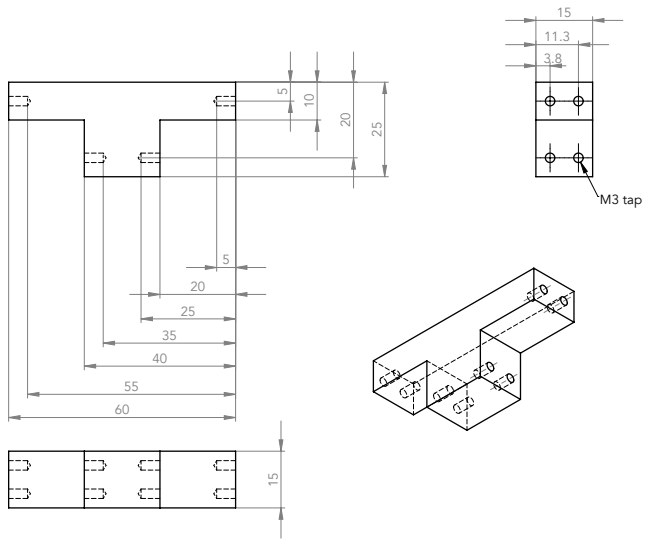


Figure D.4: Technical drawing and measures of the intermediate body.

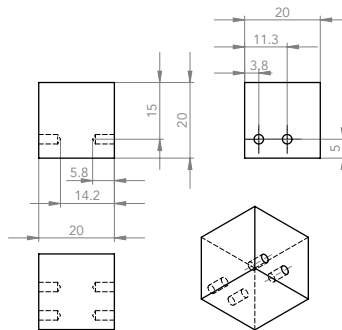


Figure D.5: Technical drawing and measures of the HFO.

D

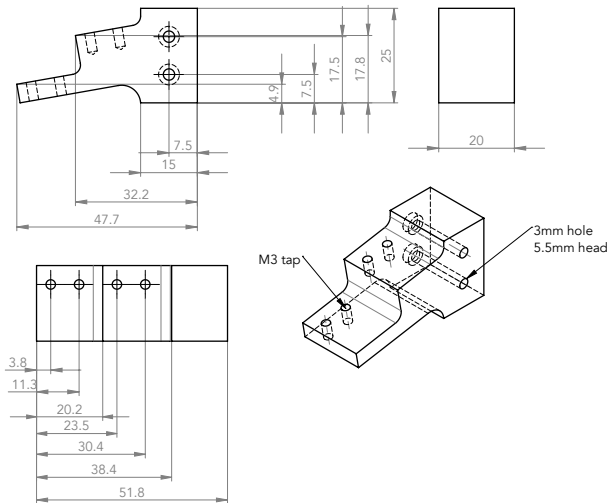


Figure D.6: Technical drawing and measures of the 1st set of connectors of the LFO flexures.

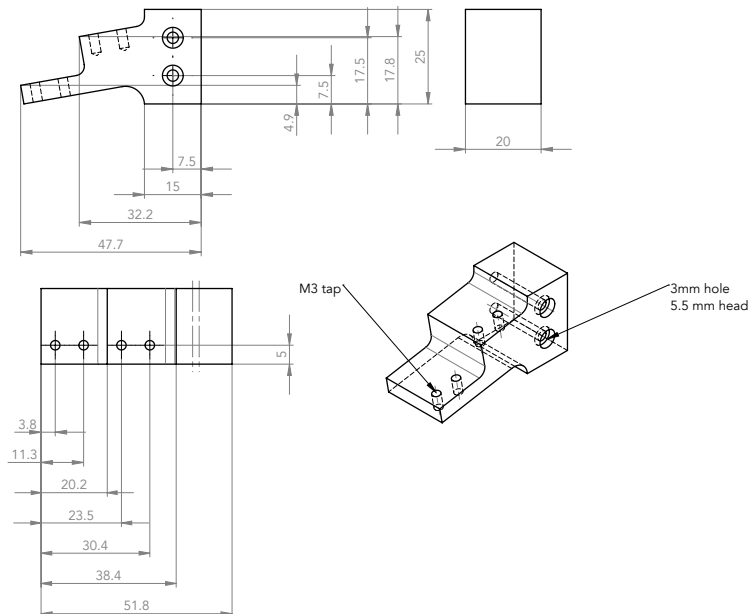


Figure D.7: Technical drawing and measures of the 2nd set of connectors of the LFO flexures.

Appendix E

PRBM models of buckled flexures

E.1 Pseudo rigid body models of building blocks

The pseudo-rigid-body model (PRBM) is a technique that can be used to predict the deflection path and the force-deflection relationships of the flexible elements [30]. In this model, the motion of the flexible elements is modeled by rigid links connected to pin joints. Moreover, the force-deflection behavior is modeled by rotational springs at the pin joints. The main application of the PRBM is to facilitate the transition from a rigid body model (RBM), with lumped masses and stiffnesses, to a compliant model, where the distributed stiffnesses are governed by the material and geometry. This is depicted in Fig. E.1, where a cantilever beam is modeled using the three models.

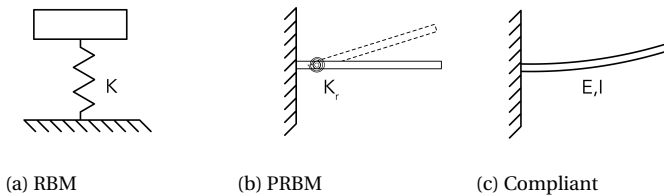


Figure E.1: **Different models of a cantilever beam; a) rigid body model with lumped stiffness, b) pseudo-rigid-body model with lumped rotational stiffness, and c) compliant model with distributed stiffness.**

The positions of the pin joints, and the stiffnesses of the rotational springs are the design parameters of this modeling technique, and have to be selected carefully. The accuracy of the PRBM is greatly determined by the selected design parameters, and the magnitudes of the angular deflections. In Fig. E.2 these parameters are identified for a cantilever beam. The location of the pin joint, or *characteristic pivot*, as a fraction of the total beam length, L , is called the *characteristic radius factor*, γ . Furthermore, the angular deflection of the the beam is called the *pseudo-rigid-body angle*, Θ , and the rotational stiffness of the torsional spring is K_r . For a more complete description of the

theory behind the PRBM technique the reader is referred to [29].

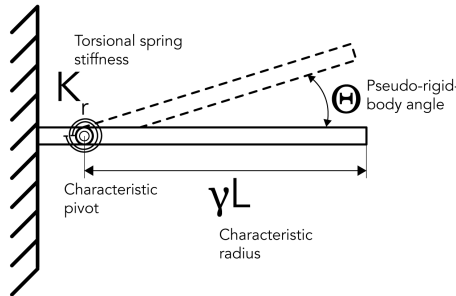


Figure E.2: PRBM of a cantilever beam; the accuracy of the model greatly depends on the selection of the characteristic radius factor, and value of the pseudo-rigid-body angle.

E

In the topology of the designed mechanism three building blocks can be identified; the fixed-free flexure, the fixed-guided flexure, and the preloaded fixed-guided flexure. Using the PRBM, we can construct models for these building blocks to evaluate their deflection path and the force-deflection behaviors. These building blocks can then be stacked to reconstruct the desired mechanical behavior of the system, as modeled by the RBM. In the next sections, the PRBM's of the building blocks will be constructed and evaluated.

E.1.1 Fixed-free flexure

The first building block is the fixed-free flexure that bends as a result of a vertical force, F , applied at the tip of the flexure. This model can be used to represent the bending and force-deflection behavior of flexible structures such as cantilever beams with a tip mass. In Fig. E.3 the PRBM of the fixed-free flexure is shown.

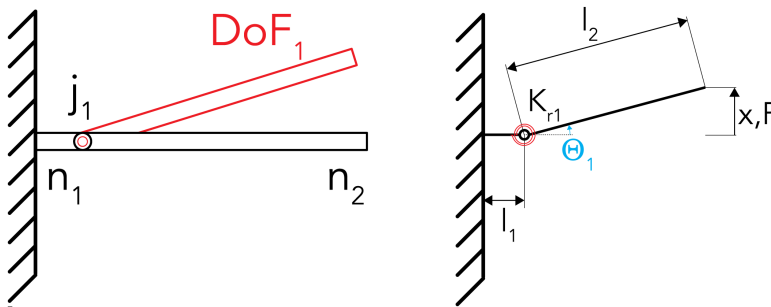


Figure E.3: PRBM of the fixed-free flexure; the model represents the bending and force-deflection behavior of flexible structures, and can be used as a building block for more complex models.

The planar model contains two bodies ($n = 2$) and one rotational joint ($j = 1$) that constrains two translations. Therefore, using Gruebler's equation the single DoF of the system can be identified.

$$3(n-1) - 2(j) = 1 \quad (\text{E.1})$$

The motion that results from the single DoF is the combined vertical translation, axial translation, and rotation at the tip of the cantilever. The linear displacement of the tip, x can be found as a function of the angle and the distance between the tip and the characteristic pivot.

$$x = l_2 \sin(\Theta) \quad (\text{E.2})$$

The potential energy in the system, E , can be found from the stiffness of the torsional spring, K_r , and the deflection of the torsional spring, Θ .

$$E = \frac{1}{2} K_r \Theta^2 \quad (\text{E.3})$$

The vertical force, F , at the tip of the flexure can be found by deriving the potential energy to the vertical coordinate at the tip of the cantilever, x . The *equilibrium positions* of the system are found where the first derivative of the energy equation equals zero.

$$F = \frac{\partial E}{\partial x} = \frac{\partial E}{\partial \Theta} \frac{\partial \Theta}{\partial x} = \frac{K_r \arcsin(\frac{x}{l_2})}{\sqrt{l_2^2 - x^2}} \quad (\text{E.4})$$

As one would expect, a single equilibrium position is found at $x = 0$. The stability of this equilibrium position can be checked by evaluating the second derivative to the energy equation at the equilibrium position.

$$K_{eq} = \left. \frac{\partial^2 E}{\partial x^2} \right|_{x=0} = \frac{K_r}{l_2^2} \quad (\text{E.5})$$

Since the second derivative of the energy equation is positive at the equilibrium point, the position is stable. The force-deflection behavior of the system is nonlinear and dependent on the deflection angle. However, if small deflections are assumed the *linearized* stiffness around $x = 0$ found in Eq. E.5 can be used. Using this linearization, the torsional stiffness of the PRBM can be synthesized from a desired linear stiffness, K .

E.1.2 Validation of the fixed-free flexure PRBM

For these fixed-free flexures a characteristic radius of $l_2 = \gamma L = 0.85L$ was determined to yield accurate results [29]. Using these assumptions, the torsional stiffness of the PRBM can be found.

$$K_r \approx 0.72L^2 K \quad (\text{E.6})$$

The PRBM was constructed in Simulink using the Simmechanics toolbox, and the force-deflection behavior was recorded. A low frequency sinusoidal displacement of $d = 1 \times 10^{-3} \sin(\frac{0.1}{2\pi} t)$ was applied to the structure and the resulting restoring force was measured. The resulting force-deflection graph of Fig. E.4 shows that the model is in good correspondence with the predicted stiffness of $K = 1$.

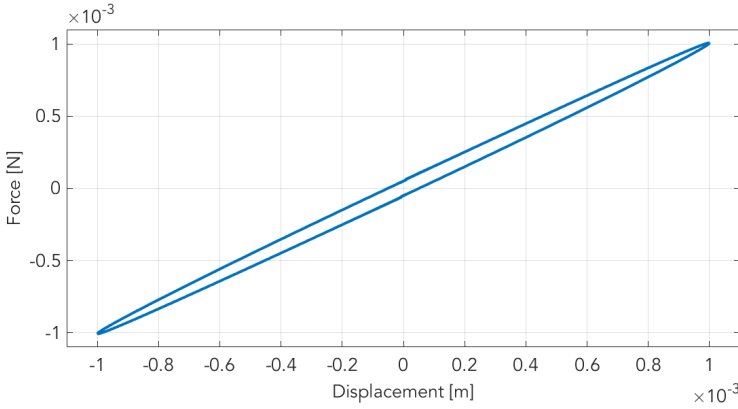


Figure E.4: Force-deflection curve of the PRBM of the fixed-free flexure. The rotational stiffnesses calculated by Eq. E.6 resulted in a linear stiffness of $K = 1$.

E

E.1.3 Fixed-guided flexure

The fixed-guided flexures differ from the fixed-free flexures in the sense that the rotation at the tip is constrained. Parallel sets of this building blocks are often encountered in compliant mechanisms to guide a linear motion. The PRBM of the fixed-guided flexure, shown in Fig. E.5, can essentially be constructed by the series combination of two fixed-free flexures.

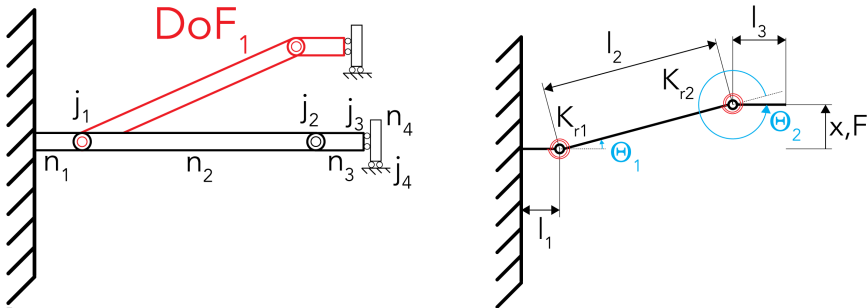


Figure E.5: PRBM of the fixed-guided flexure can be constructed by the series combination of two fixed-free flexures; If the axial deflection is constrained the model is only valid for infinitesimal small rotations.

The angular constraint enforced by the sliding joints is formulated as $\Theta_2 = -\Theta_1$. As a result, the planar model contains four bodies ($n = 4$), two rotational joints that constrain two translations, and two sliding joints that constrain a translation and a rotation ($j = 4$). Therefore, using Gruebler's equation a single DoF of the system can be identified.

$$3(n - 1) - 2(j) = 1 \tag{E.7}$$

The motion that results from the DoF is the vertical translation of the tip of the cantilever

combined with a translation in the axial direction. The linear displacement of the tip, x can be found as a function of the angle and the length of the beam.

$$x = l_2 \sin(\Theta_1) \quad (\text{E.8})$$

The energy equation of the system, E , can be found by summing the energies in the torsional springs, and is a function of the stiffnesses of the torsional springs, K_i , and their deflections, Θ_i .

$$E = 0.5K_{r1}\Theta_1^2 + 0.5K_{r2}(\Theta_2)^2 \quad (\text{E.9})$$

Again, the energy equation is derived w.r.t. x to find the force, F , and the equilibrium positions of the system are found where the first derivative of the energy equation equals zero.

$$F = \frac{\partial E}{\partial x} = \frac{\partial E}{\partial \Theta_1} \frac{\partial \Theta_1}{\partial x} = (K_{r1} + K_{r2}) \frac{\arcsin(\frac{x}{l_2})}{\sqrt{l_2^2 - x^2}} \quad (\text{E.10})$$

The same equilibrium position is found at $x = 0$, and evaluating the second derivative at the equilibrium shows that the position is stable.

$$K_{eq} = \left. \frac{\partial^2 E}{\partial x^2} \right|_{x=0} = \frac{K_{r1} + K_{r2}}{l_2^2} \quad (\text{E.11})$$

E.1.4 Validation of the fixed-guided flexure PRBM

Effectively, the stiffness that is found here is a series combination of two times the linearized stiffness found in E.5. If a symmetric combination of two identical fixed-free PRBM's mirrored around the center is assumed, the following simplifications can be made.

$$l_2 = \gamma L \quad (\text{E.12})$$

$$l_1 = l_3 = (1 - \gamma) \frac{L}{2} \quad (\text{E.13})$$

$$K_{r1} = K_{r2} = K_r \quad (\text{E.14})$$

Using the same assumptions from the previous sections, the torsional stiffnesses of the PRBM can be synthesized from a desired linear stiffness, K .

$$K_r \approx 0.36L^2 K \quad (\text{E.15})$$

The PRBM was constructed in Simulink using the Simmechanics toolbox, and the force-deflection behavior was recorded. A low frequency sinusoidal displacement of $d = 1 \times 10^{-3} \sin(\frac{0.1}{2\pi} t)$ was applied to the structure and the resulting restoring force was measured. The rotation of the tip was constrained, but the axial translation was free. The resulting force-deflection graph of Fig. E.4 shows that the model is in good correspondence with the predicted stiffness of $K = 1$.

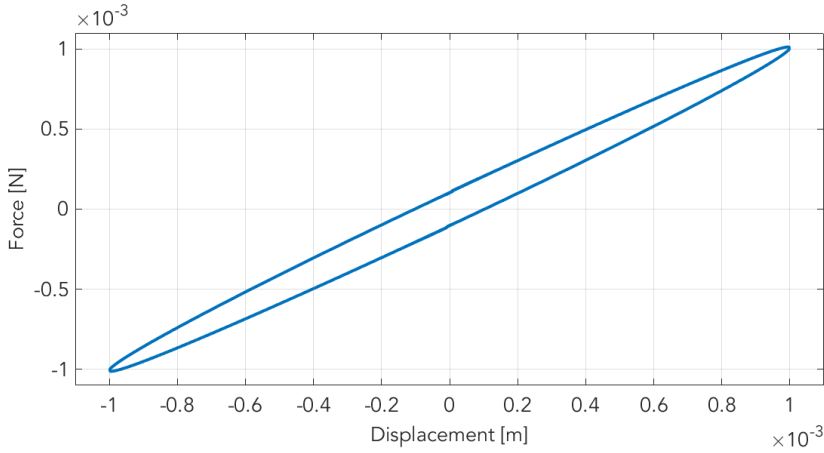


Figure E.6: Force-deflection curve of the PRBM of the fixed-guided flexure; The rotation of the tip was constrained, but the axial translation was free. The rotational stiffnesses calculated by Eq. E.15 resulted in a linear stiffness of $K = 1$.

E

E.1.5 Preloaded fixed-guided flexure

The preloaded fixed-guided flexure is the building block and is used to introduce a negative stiffness into the system. In this building block, both the axial translation and the rotation at the tip are constrained. A preload is introduced in the system by a distance constraint between the two grounds of $D = \eta L$, where $\eta < 1$. The PRBM of the fixed-guided flexure, shown in Fig. E.5, can essentially be constructed by the series combination of two fixed-guided flexures in a deflected state.

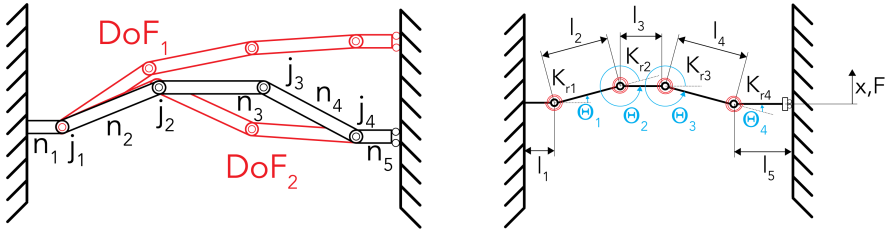


Figure E.7: PRBM of the fixed-guided flexure can be constructed by the series combination of two fixed-free flexures; If the axial deflection is constrained the model is only valid for infinitesimal small rotations.

The two constraints introduced by fixing the rotation and axial translation of the tip can be formulated in the following way.

$$\Theta_4 = -(\Theta_1 + \Theta_2 + \Theta_3) \tag{E.16}$$

$$\Theta_3 = \arccos\left(\frac{L - l_1 - l_2 \cos(\Theta_1) - l_3 \cos(\Theta_1 + \Theta_2) - l_5}{l_4}\right) - \Theta_1 - \Theta_2 \tag{E.17}$$

Therefore, the resulting model contains five bodies ($n = 5$), four rotational joints that constrain two translations and a sliding joint that constrains axial translation and rotation at the tip ($j = 5$). Using Gruebler's equation two DoF's of the system can be found.

$$3(n - 1) - 2(j) = 2 \quad (\text{E.18})$$

The motion that results from the first DoF is the vertical displacement at the tip, x , and the motion that results from the second DoF is the rotation of the middle body, T_2 . These motions of the system can be expressed in terms of the angles Θ_i .

$$x = l_2 \sin(\Theta_1) + l_3 \sin(\Theta_1 + \Theta_2) + l_4 * \sin(\Theta_1 + \Theta_2 + \Theta_3) \quad (\text{E.19})$$

$$T_2 = \Theta_1 + \Theta_2 \quad (\text{E.20})$$

The energy equation of the system, E , can be found by summing the energies in the torsional springs, and is a function of the stiffnesses of the torsional springs, K_i , and their deflections, Θ_i .

$$E = 0.5K_{r1}\Theta_1^2 + 0.5K_{r2}(\Theta_2)^2 + 0.5K_{r3}(\Theta_3)^2 + 0.5K_{r4}(\Theta_4)^2 \quad (\text{E.21})$$

The following two methods are used to continue further analysis of the 2DoF system.

Trapezoid method

The first method that is used is the trapezoid method that introduces an additional geometric constraint. In this method, the torsional stiffnesses are considered equal.¹ It is assumed that for a uniform beam of a single material, this is a reasonable assumption.

$$K_1 = K_2 = K_3 = K_4 = K_r \quad (\text{E.22})$$

The method of finding a solution is graphically described in Fig. E.8 where the geometry of the system is assumed to be of a trapezoidal shape. This symmetric position is the state of lowest energy for a vertical displacement of $x = 0$.

In the figure, the length of the trapezoid base is β and the angle the trapezoid makes with the horizontal is ϕ . By geometric relations these variables can be determined.

$$\beta = \sqrt{(x^2 + (L - l_1 - l_5)^2)} \quad (\text{E.23})$$

$$\phi = \arctan\left(\frac{x}{L - l_1 - l_5}\right) \quad (\text{E.24})$$

By introducing this geometrical constraint the system is reduced to a single DoF system with exactly two solutions for a given x . Those solutions are the "knee-up" and "knee-down" solutions, of which the "knee-down" will be considered in the further analysis. As a result, the pseudo rigid body angles Θ_i of Fig. E.7 can be found.

¹In fact, $K_1 = K_4$ and $K_2 = K_3$ is satisfactory, but an overall equality is chosen for simplicity

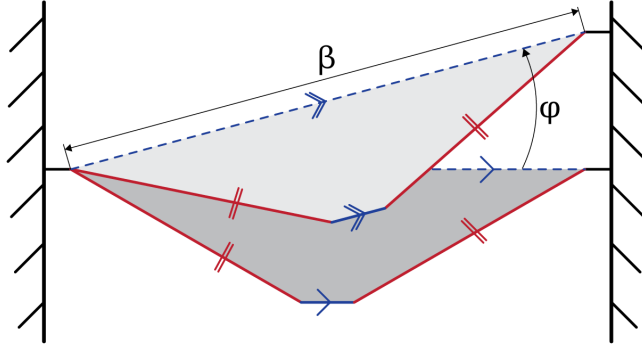


Figure E.8: Illustration of the trapezoid method used to model the characteristics of the 2PRBM

E

$$\begin{aligned}
 \Theta_1 &= -\arccos\left(\frac{\beta - l_3}{2l_2}\right) + \phi \\
 \Theta_2 &= \arccos\left(\frac{\beta - l_3}{2l_2}\right) \\
 \Theta_3 &= \arccos\left(\frac{\beta - l_3}{2l_2}\right) \\
 \Theta_4 &= -\arccos\left(\frac{\beta - l_3}{2l_2}\right) - \phi
 \end{aligned} \tag{E.25}$$

The energy equation can be derived to x to find the force, F , and the equilibrium positions are found when the force equals zero.

$$F = \frac{\partial E}{\partial x}$$

Conform to our expectations, an equilibrium position is found at $x = 0$. Evaluating the second derivative at the equilibrium shows us that the position is unstable, which corresponds to the negative stiffness behavior of the system.

$$K_{eq} = \left. \frac{\partial^2 E}{\partial x^2} \right|_{x=0}$$

Energy-minimization method

Another method is to use an optimization algorithm (*fmincon*) that minimizes the total potential energy in the torsional springs by changing the values for Θ_i . This optimization can be physically interpreted as finding a state of minimum energy for a given discretized displacement X . The following optimization scheme was used.

min E (Eq. E.21)

$$\begin{aligned} \text{s.t.} \quad & x_{\text{base}} = 0 \\ & y_{\text{base}} = 0 \\ & x_{j4} - X = 0 \\ & x_{\text{tip}} - X = 0 \\ & y_{\text{tip}} - L = 0 \end{aligned}$$

The initial values Θ_i^0 used in this method were the results from the trapezoid method. The force-displacement characteristic at the tip can be found by numerically deriving the found optimum energy to the discretized displacement X .

$$F = \frac{\partial E}{\partial X} \approx \frac{dE}{dX} \quad (\text{E.26})$$

Improved trapezoid method

It can be seen that in the trapezoid method the torsional springs in the joints 1 and 4 are loaded equally in the horizontal position, $x = 0$. As a result, these joints exercise an equal moment on the central body and the trapezoid geometry is the state of minimum potential energy. However, if the tip is displaced from the horizontal position these joints are no longer loaded equally. When the tip moves upwards, the moment in the torsional spring of joint 4 increases while the moment in the torsional spring of joint 1 decreases. This results in a moment imbalance that must be compensated by the torsional springs in the joints of the central body. Therefore, the state of minimum potential energy is achieved when the central body rotates slightly more than ϕ , depicted as the second DoF in Fig. E.7. As a result, the trapezoid methods underestimates the potential energy differences, and thus predicts a lower magnitude of the negative stiffness.

$$\begin{aligned} \Theta_1^* &= -0.11(-2.864\eta^3 + 7.722\eta^2 - 7.185\eta + 2.398) \frac{x}{L_0} \\ \Theta_2^* &= 1.11(-2.864\eta^3 + 7.722\eta^2 - 7.185\eta + 2.398) \frac{x}{L_0} \\ \Theta_3^* &= -1.11(-2.864\eta^3 + 7.722\eta^2 - 7.185\eta + 2.398) \frac{x}{L_0} \\ \Theta_4^* &= -(\Theta_1^* + \Theta_2^* + \Theta_3^*) \end{aligned} \quad (\text{E.27})$$

Motion in the second DoF can be added to compensate for this error, as shown in Fig E.9. Using the results from the energy optimization method the error in the rotation of the central body was studied and the compensation factors of E.27 were iteratively determined. Most likely, it would be possible to find an exact solution for the second DoF compensation of the system. However, this falls outside the scope of this thesis, and is therefore included as a recommendation for future research.

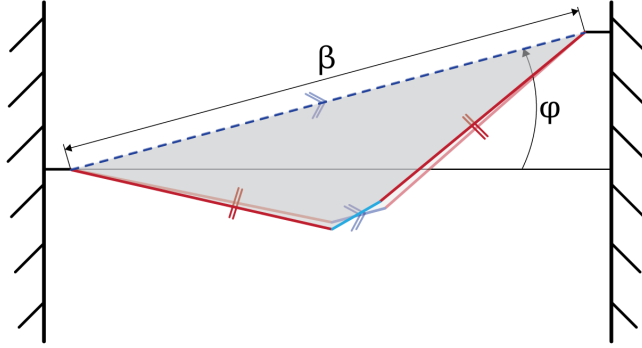


Figure E.9: Improved trapezoid method where a compensation is added conform to the second DoF of the system.

E

E.1.6 Validation of the Preloaded fixed-guided flexure

Using $\gamma = 0.85$ and $\eta = .9$, the following torsional stiffnesses of the PRBM can be synthesized from a desired linear stiffness, K .

$$K_r \approx -0.33L^2K \tag{E.28}$$

The found force-deflection curves for both methods, as well as the numerical simulation, are shown in Fig. E.10. It can be seen that all methods resulted in matching force-deflection behaviors for the preloaded fixed-guided flexure.

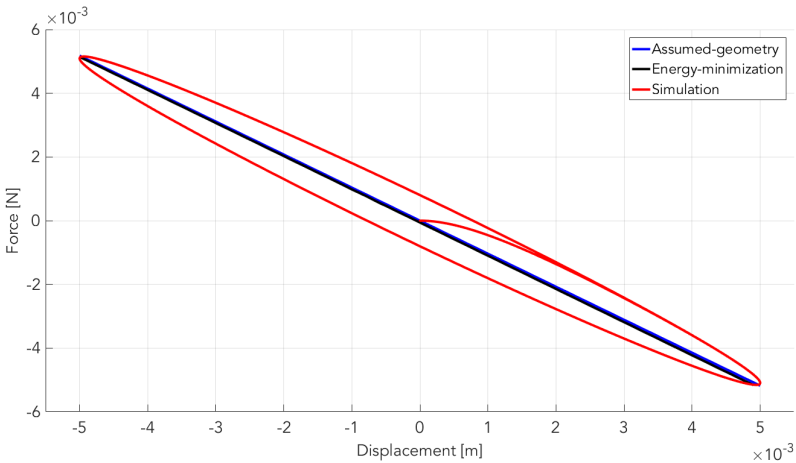


Figure E.10: Force-deflection curve of the PRBM of the preloaded fixed-guided flexure; The rotation of the tip and the axial translations were constrained.

E.2 Compliant models of the building blocks

E.2.1 Fixed-free flexure

The deflection of a beam can be calculated using the beam deflection equation.

$$\frac{F}{x} = \frac{3EI}{L^3} \quad (\text{E.29})$$

By setting the right side of the equation equal to the right side of Eq. E.5, the rotational stiffness of the pseudo-rigid-body model can be written in terms of the rigidity of the compliant element. The following equation is obtained.

$$K_r = \frac{3EI\gamma^2}{L} \quad (\text{E.30})$$

Now, this result can be applied in the pseudo-rigid-body formula to find the stiffness of the overall system. For the fixed-free flexure the result is merely a reproduction of linear beam theory, but is derived here for completeness. The regular linear beam theory formula is obtained when Eq. E.30 is substituted in E.5.

$$K = \frac{3EI\gamma^2}{Ll_2^2} = \frac{3EI}{L^3} \quad (\text{E.31})$$

E.2.2 Fixed-guided flexure

The same procedure can be used to synthesize the rigidity of a fixed-guided beam. Substituting Eq. E.30 in the obtained PRBM of Eq. E.11 finds the following stiffness for the fixed-guided compliant beam. This result is in accordance with regular theory for a fixed-guided beam.

$$K = \frac{\frac{3EI\gamma^2}{Ll_2} + \frac{3EI\gamma^2}{Ll_2}}{(\gamma L^2)} = \frac{12EI}{L^3} \quad (\text{E.32})$$

E.2.3 Preloaded fixed-guided flexure

For the preloaded fixed-guided flexure, the same procedure is adopted. The flexure is divided in four sections with lengths $\frac{L_0}{4}$. Then, Eq. E.30 is substituted in the PRBM. This finds the following stiffness for the fixed-guided compliant beam.

$$K = \frac{96EI\gamma^2}{L_0^3(2\eta + \gamma - 1)^2} - \frac{96EI\gamma \arccos\left(\frac{2\eta + 2\gamma - 2}{2\gamma}\right)}{L_0^3 \sqrt{1 - \frac{(2\eta + 2\gamma - 2)^2}{4\gamma^2}}} \quad (\text{E.33})$$

E.3 Simulink implementation

It was attempted to implement the constructed equations in a Simulink model, but no useable results were obtained.

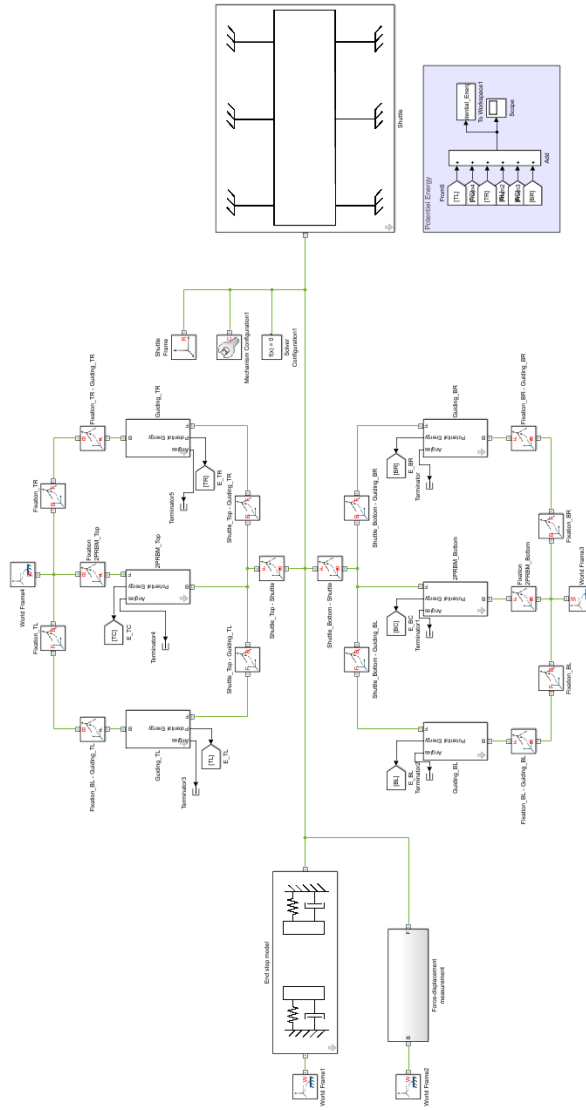


Figure E.11: Overview of attempted Simulink network of full system

Appendix F

Transducer models of piezoelectric beams

F.1 Mechanical Equation of Motion and Modal Analysis of Cantilever Beam

In this section an analytical model for the beam depicted in Fig. E1 is given. In the figure $w(x, t)$ is the displacement of the neutral axis of point x at time t , M_t is the value of the tip mass, and I_t is the moment of inertia of the tip mass. Following the analysis of [8], the linear vibrations are considered and the expressions for the undamped natural frequencies and mode shapes are obtained.

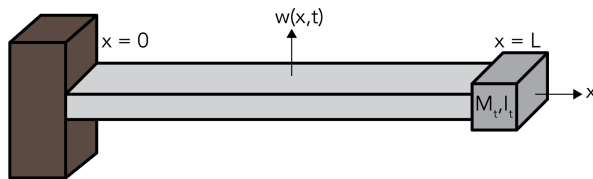


Figure E1: Cantilevered uniform beam with a tip mass

F.1.1 Boundary-Value Problem

Using the Euler-Bernoulli assumptions, the governing equation of motion for the undamped free vibrations of a uniform beam can be obtained [35].

$$EI \frac{\partial^4 w(x, t)}{\partial x^4} + m \frac{\partial^2 w(x, t)}{\partial t^2} = 0 \quad (\text{E.1})$$

Where EI is the bending stiffness and m is the mass per unit length of the beam. The boundary conditions (i.e. clamped in one end and free in the other end) for the beam depicted in Fig. E.1 can be expressed in the following way.

$$\begin{aligned} w(0, t) = 0 \quad \left. \frac{\partial w(x, t)}{\partial x} \right|_{x=0} = 0 \\ \left[EI \frac{\partial^2 w(x, t)}{\partial x^2} + I_t \frac{\partial^3 w(x, t)}{\partial t^2 \partial x} \right]_{x=L} = 0 \quad \left[EI \frac{\partial^3 w(x, t)}{\partial x^3} - M_t \frac{\partial^2 w(x, t)}{\partial t^2} \right]_{x=L} = 0 \end{aligned} \quad (\text{E.2})$$

E.1.2 Modal Analysis using Assumed Mode Formulation

To find a solution for $w(x, t)$ in Eq. E.1 the method of separation of variables can be used. In this method, $w(x, t)$ is separated in function $\phi(x)$ which is only a function of the spacial coordinate and function $\eta(t)$ which is only a function of time. Furthermore, the solution can be built from an infinite sum of vibration modes where the subscript r denotes the number of the vibration mode.

$$w(x, t) = \sum_{r=1}^{\infty} \phi_r(x) \eta_r(t) \quad (\text{E.3})$$

For the spacial function $\phi_r(x)$ a displacement field can be assumed that is kinematically admissible given the boundary conditions of Eq. E.2.

E.1.3 Single Assumed Mode Solution

In this analysis the solution of Eq. E.3 is found using a single vibration mode. Therefore, this solution will only have value at or close to the resonance frequency of the considered mode. In this case, the first eigenmode of the system will be considered and the following function is assumed to represent the displacement field.

$$\phi(x) = \left(\frac{x}{L} \right)^2 \quad (\text{E.4})$$

The maximum strain energy, V , and kinetic energy, T , for the cantilevered beam with the tip mass are given by the following functions.

$$V = \frac{1}{2} \int_0^L EI \left[\frac{\partial^2 \phi(x)}{\partial x^2} \right]^2 dx \quad (\text{E.5})$$

$$T = \frac{1}{2} \int_0^L \rho W H \dot{\phi}^2(x) dx + \frac{1}{2} M \dot{\phi}^2(L) \quad (\text{E.6})$$

Now, the Rayleigh coefficient can be used to estimate the first eigenfrequency of the system based on the assumed mode shape.

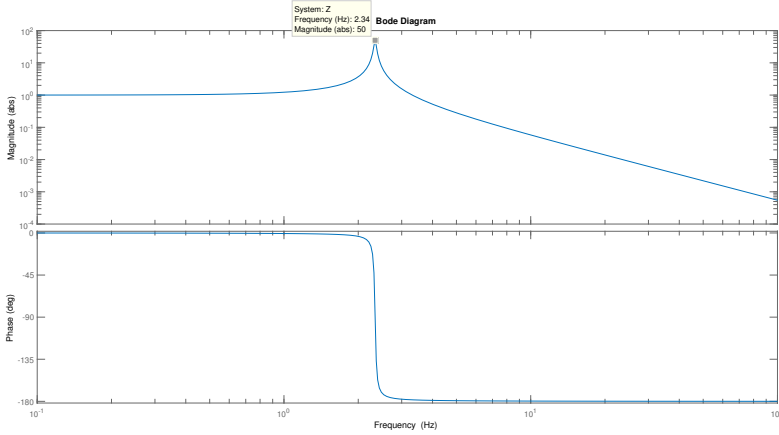


Figure E2: Frequency response of Z

$$\omega_n = \sqrt{\frac{V}{T}} \approx 14.7 \text{ rad s}^{-1} \approx 2.34 \text{ Hz} \tag{E.7}$$

The temporal part of the solution of the free vibration problem is given by $\eta(t)$. When excited by a harmonic input, the following equation can be used to represent $\eta(t)$.

$$\eta(t) = Z_0 \cos(\Omega t) \tag{E.8}$$

$$w(x, t) = \left(\frac{x}{L}\right)^2 Z_0 \cos(\Omega t) \tag{E.9}$$

The frequency response can now be found from the transfer function. The lumped-parameter transfer function of the transmissibility of the second order system is given by the following expression and its frequency response is plotted in Fig. E2.

$$\frac{Z_0}{Y_0} = \frac{\left(\frac{\Omega}{\omega_n}\right)^2}{\sqrt{\left(1 - \left(\frac{\Omega}{\omega_n}\right)^2\right)^2 + \left(2\zeta\frac{\Omega}{\omega_n}\right)^2}} \tag{E.10}$$

E.1.4 Multi Assumed Mode Solution

The solution of Eq. E3 can also be found using multiple vibration modes. Such a solution will have value over a wider frequency range than the single mode solution. An approach to finding such a solution can be the use of the following function to represent the displacement field. In this function r represents the mode number.

$$\phi_r(x) = 1 - \cos\left[\frac{(2r - 1)\pi x}{2L}\right] \tag{E.11}$$

F.2 Electrical coupling modeling

The electromechanical coupling of the piezoelectric material can be described by the two constitutive equations for linear piezoelectric material. The equations Eq. F.12 and Eq. F.13 are known as the piezoelectric actuator and sensor equations, respectively.

$$S = S^E T + D_t E \quad (\text{F.12})$$

$$D = d_t T + \epsilon^T E \quad (\text{F.13})$$

Where S is mechanical strain, T applied stress, E electric field, D electric displacement, S^E the matrix of elasticity under conditions of constant electric field, d piezoelectric coefficient matrix, ϵ^T permittivity matrix at constant mechanical strain.

In order to understand the coupling that occurs in a cantilever with a piezoelectric element we examine the boundary conditions of the sensor equation. These boundary conditions are the open circuit condition, where $D = 0$, and the short circuit condition, where $E = 0$.

F.2.1 Open circuit condition

In the open circuit condition the electrodes are connected to the piezoelectric material at one end, and free on the other end as shown in Fig. F.3. The electric displacement equals zero, as there is no way for the charges to flow from one side to the other. Therefore, an electric field is induced across the piezoelectric material.

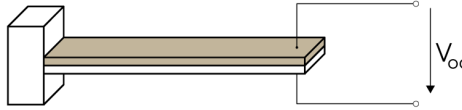


Figure F.3: Schematic representation of open circuit boundary condition. In this case, the electric displacement equals zero and maximum voltage is induced across the terminals.

The magnitude of the electric field can be found from Eq. F.13 for $D = 0$. For the cantilever geometry, it is assumed that there is only stress in the 11-direction, which corresponds to the length of the cantilever. Therefore, the stress matrix T is reduced to σ_{11} and the d_t matrix is reduced to d_{31} .

$$E_{oc} = -\frac{d_{31}\sigma_{11}}{\epsilon^T} \quad (\text{F.14})$$

This equation can be rewritten in terms of voltage by substituting $V_{oc} = E_{oc} t$, where t is the thickness of the piezoelectric element. The resulting equations Eq. F.15 and Eq. F.16 can be used to calculate the open circuit voltage of a cantilever with a piezoelectric element with a given stress or strain, respectively.

$$|V_{oc}| = t\sigma_{11} \frac{d_{31}}{\epsilon^T} = t\sigma_{11}g_{31} \quad (\text{F.15})$$

$$|V_{oc}| = tS_{11} \frac{d_{31}}{\epsilon^T S_{11}^E} = tS_{11} h_{31} \quad (\text{F.16})$$

F.2.2 Short circuit condition

The other boundary condition is the short circuit condition. Here, the electrodes are connected to the piezoelectric material at one end, and to each other on the other end, as illustrated in Fig. F.4. When we assume the wire has zero resistance, charges can flow freely from one end to the other. As a result, the electric field across the piezoelectric material must be zero.

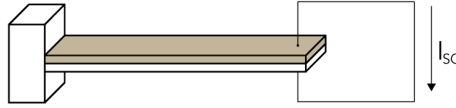


Figure F4: Schematic representation of short circuit boundary condition. In this case, the electric field equals zero and the current through the circuit is maximum.

The piezoelectric sensor equation can now be used for $E = 0$ to find the electric displacement. Similar to the open circuit case, it is assumed that there is only stress in the 11-direction which reduces the stress matrix T to σ_{11} and the d_t matrix to d_{31} .

$$D_{sc} = d_{31}\sigma_{11} \quad (\text{F.17})$$

The electric displacement can be written in terms of charge per unit area by making use of Gauss's law. The area can be rewritten in terms of the thickness, t , and the capacitance, C_p , of the piezoelectric element.

$$D_{sc} = \frac{q}{A} = \frac{q\epsilon^T}{C_p t} \quad (\text{F.18})$$

Substitution of Eq. F.18 in Eq. F.17 results in a form where the charge that flows between the electrodes can be found for a given stress. By differentiation with respect to time the short circuit current can be found. The resulting equations Eq. F.19 and Eq. F.20 can be used to calculate the short circuit current of a cantilever with a piezoelectric element with a given stress or strain, respectively.

$$|I_{sc}| = ftC_p\sigma_{11} \frac{d_{31}}{\epsilon^T} = ftC_p\sigma_{11}g_{31} \quad (\text{F.19})$$

$$|I_{sc}| = ftC_pS_{11} \frac{d_{31}}{\epsilon^T S_{11}^E} = ftC_pS_{11}h_{31} \quad (\text{F.20})$$

F.3 Constitutive equations of piezoelectric cantilevered beam

The following declaration of variables will be used in the constitutive equations of the piezoelectric cantilevered beam.

| Domain | Variable | Symbol | Unit |
|------------------------|--|------------|-------------------|
| Mechanical | Tip force | f | N |
| | Tip displacement | δ | m |
| | Velocity | u | m s^{-1} |
| | Strain in substrate layer (11-direction) | S_s | m m^{-1} |
| | Stress in substrate layer (11-direction) | T_s | Pa |
| | Strain in piezoelectric layer (11-direction) | S_p | m m^{-1} |
| | Stress in piezoelectric layer (11-direction) | T_p | Pa |
| Electrical | Electric displacement | D | C m^{-2} |
| | Current | I | A |
| | Voltage | V | V |
| | Electric field | \vec{E} | V m^{-1} |
| Geometrical properties | Length of the beam | L | m |
| | Width of the beam | b | m |
| | Thickness of the substrate layer | h | m |
| | Thickness of the piezoelectric layer | t | m |
| | Distance to neutral line | y | m |
| Material properties | Elastic modulus of substrate layer | Y_s | Pa |
| | Elastic modulus of piezoelectric layer | Y_p | Pa |
| | Piezoelectric strain coefficient in 31-mode | d_{31} | NC^{-1} |
| | Permittivity of piezoelectric material | ϵ | F m^{-1} |

Table F.1: Overview of variables used in the constitutive equations of the piezoelectric cantilevered beam.

F.3.1 Mechanical constitutive equations

In the previous section, the function of Eq. F.4 was assumed as the first eigenmode of the system. Using this function, the strain in the substrate layer can be found. The cantilevered beam is assumed to be loaded in pure bending, and the piezoelectric layer is assumed not to contribute to the stiffness of the beam. Therefore the following expression can be found for the strain in the bending beam.

$$\sigma = y \frac{\partial^2 \phi(x)}{\partial x^2} Y \quad (\text{F.21})$$

This can be averaged over the length of the beam and the thickness direction of the piezoelectric element.

$$\sigma_a = \frac{2}{LW} \int_0^L \int_0^{\frac{w}{2}} \sigma dy dx \quad (\text{F.22})$$

F.3.2 Electro mechanical coupling modeling

The electrical and mechanical domains are weakly coupled. therefore, we may use a coupling that does not include actuation feedback, but only sensing. The electric displacement can be estimated by the following formula.

$$D = d_{31}\sigma_a \tag{F.23}$$

The electric displacement can be multiplied by the area of the electrode to find the charge, Q .

$$Q = d_{31}hL\sigma_a\eta \tag{F.24}$$

Since the current is equal of the amount of charge per time, the following formula can be found for the current that the piezoelectric element supplies to the electrical circuitry.

$$I = d_{31}hL\sigma_a \frac{\partial \eta}{\partial t} \tag{F.25}$$

F.3.3 Full beam model

Summation of all the contributions of a bending moment leads to the following system of equations.

$$EI \frac{\partial^2 \phi(x)}{\partial x^2} = F(L-x) - \frac{\partial^2 \phi(x)}{\partial x^2} \left(\frac{h}{2}\right)^2 Y_p A - d_{31}EA \tag{F.26}$$

$$D = d_{31} \frac{\partial^2 \phi(x)}{\partial x^2} Y_p \frac{h}{2} + \epsilon E \tag{F.27}$$

F.4 Simulink implementation

It was attempted to implement the constructed equations in a Simulink model, but no useable results were obtained.

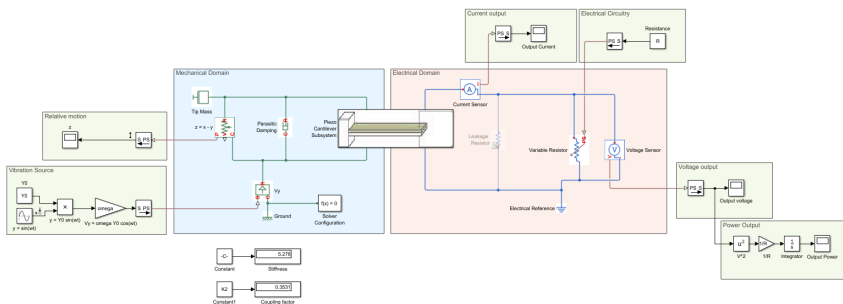


Figure E.5: Overview of attempted Simulink implementation with the cantilever model in the center.

Appendix G

Literature search data

G.1 Multi-DoF vibration energy harvesters

| Source | DoF | TD | Area / Volume | Frequency | Acceleration | Power output |
|----------------------|-----|----|-----------------------|-----------|--------------|-------------------------|
| Paracha (2006) [36] | 2 | S | 1 cm ³ | 300 Hz | | 1.8 μW |
| Zhu (2009) [37] | 2 | S | 4 mm ² | 38 kHz | | 0.1 nW |
| Paracha (2009) [38] | 2 | S | 1 cm ² | 246 Hz | 0.25 g | 2.6 μW |
| Bartsch (2009) [39] | 2 | S | 16 cm ² | 1 kHz | | 100 pW |
| Bartsch (2010) [40] | 2 | S | 16 cm ² | 370 Hz | | |
| Yang (2010) [41] | 2 | S | 39.4 mm ² | 110 Hz | 2.5 g | 0.35 μW |
| Zhu (2011) [42] | 2 | S | 4 mm ² | 38 kHz | | 21.4 nW |
| Liu (2012) [43] | 3 | M | 80 mm ² | 1.5 kHz | 1 g | 16 nW |
| Kim (2012) [44] | 2 | S | 81 mm ² | 191 Hz | 0.12 g | 35.5 nW |
| Fowler (2012) [45] | 3 | S | 15 mm ² | 36 kHz | | 21.4 nW |
| Cueff (2013) [46] | 2 | M | | 15 Hz | 0.5 g | 100 μW cm ⁻³ |
| Janicek (2013) [47] | 3 | S | | 106 Hz | | |
| Crovetto (2013) [48] | 2 | S | 1 cm ² | 179 Hz | 0.03 g | 32.5 nW |
| Fowler (2013) [49] | 3 | S | 16 mm ² | 25 kHz | | 24.7 nW |
| Fowler (2013) [50] | 2 | S | 1 mm ² | 39 kHz | | 27.6 nW |
| Iannacci (2013) [51] | 2 | S | 2.25 mm ² | 2 kHz | 0.5 g | 1 pW |
| Wei (2013) [52] | 2 | S | 2.25 mm ² | 30 Hz | 17.7 g | 6.5 nW |
| Wu (2014) [53] | 2 | P | 259.2 cm ³ | 37 Hz | 0.2 g | 2.5 mW |
| Yang (2014) [54] | 2 | M | | 4.2 Hz | 0.6 g | |
| Han (2014) [55] | 3 | M | 1 cm ³ | | 0.5 g | 0.75 μW |
| Tao (2014) [56] | 3 | S | | 66 Hz | 0.05 g | 4.8 nW |

Table G.1: **Properties of MDoF vibration energy harvesters found in literature.** P = piezoelectric, M = electromagnetic, S = electrostatic transduction mechanism.

G.2 Generators with human motion vibration sources

| Source | Year | Transfer | Transduction | Mechanical Input | Generator location | Volume cm ³ | Power output W |
|----------------|------|----------|---------------|-----------------------------|--------------------|------------------------|-----------------------|
| Alghishi [21] | 2015 | IFI | Piezo | Walking 2km/h | Ankle | 90 | 5.38×10^{-6} |
| Berdy [57] | 2015 | DNS | Coil | Walking 3mp/h (6Hz, 0.057g) | | 2.8 | 7.14×10^{-5} |
| Bowers [58] | 2009 | DS | Coil | Walking 4km/h | | 4.0 | 2.60×10^{-4} |
| Choi [59] | 2011 | DNS | Electrostatic | Walking 8 km/h | | 1.0 | 3.67×10^{-5} |
| Geisler [60] | 2016 | DNS | Coil | Walking 6.4 km/h | Upperarm | 9.0 | 3.94×10^{-3} |
| Halim [61] | 2015 | IFI | Coil | Hand shaking (5.2 Hz, ~2g) | Hand | 6.5 | 2.13×10^{-3} |
| Halim [62] | 2017 | IFB | Piezo | Hand shaking (4.96 Hz, ~2g) | Hand | 23 | 1.75×10^{-4} |
| Halim [63] | 2014 | IFI | Coil | Hand shaking (4.6 Hz, ~2g) | Hand | 7.2 | 1.10×10^{-4} |
| Halim [22] | 2016 | IFI | Coil | Slow running (1.2 Hz) | Shoesole | 3.9 | 7.80×10^{-5} |
| Haroun [64] | 2016 | DNS | Coil | Jogging 150m/min | Pocket | 0.74 | 2.21×10^{-4} |
| Haroun [64] | 2016 | DNS | Coil | Fast walk 108m/min | Pocket | 0.74 | 1.89×10^{-4} |
| Haroun [64] | 2016 | DNS | Coil | Walking 75m/min | Pocket | 0.74 | 1.60×10^{-4} |
| Lu [23] | 2015 | IFI | Electrostatic | Shaker (4.7Hz, 2g) | | 0.046 | 1.43×10^{-7} |
| Patel [65] | 2013 | DNS | Coil | | | 86 | 9.00×10^{-4} |
| Pillatsch [66] | 2012 | IFP | Piezo | Shaker (2Hz, .27g) | | 125 | 2.10×10^{-3} |
| Pillatsch [67] | 2014 | IFP | Piezo | Shaker (2Hz,2g) | | 1.85 | 4.30×10^{-5} |
| Pillatsch [68] | 2013 | IFP | Piezo | Activity | Upperarm | 1.85 | 7.00×10^{-6} |
| Rao [69] | 2013 | DS | Coil | Walking 2.5mph | Ankle | 100 | 3.00×10^{-4} |
| Rao [69] | 2013 | DS | Coil | Jogging 4mph | Wrist | 100 | 2.60×10^{-4} |
| Rao [70] | 2014 | DS | Coil | Jogging 4mph | Ankle | 70 | 2.34×10^{-4} |
| Renaud [71] | 2009 | IFI | Piezo | Hand shaking (10Hz, 10cm) | Hand | 25 | 6.00×10^{-4} |
| Romero [72] | 2009 | DS | Coil | Walking (1.7Hz,2.5g) | Ankle | 1.5 | 3.90×10^{-6} |
| Saha [73] | 2008 | DNS | Coil | Walking (2Hz,0.5 g) | Rucksack | 12.7 | 3.00×10^{-4} |
| Sauladin [74] | 2017 | DNS | Coil | Hand shaking (6Hz, .5 g) | hand | 30 | 2.25×10^{-3} |
| Wei [75] | 2013 | IFP | Piezo | walking 5kmh | | 86 | 5.10×10^{-5} |
| Xie [76] | 2016 | DNS | Coil | Walk 2 m/s | Torso | 137 | 1.00×10^{-2} |
| Yilli [77] | 2015 | DNS | Coil | walk 6kmh | ankle | 144 | 3.30×10^{-3} |
| Yilli [78] | 2014 | DNS | Coil | Walking 4km/h | Shoesole | 33.3 | 1.00×10^{-3} |
| Yilli [79] | 2015 | DNS | Coil | Walk 6kmh | shoe | 21 | 8.40×10^{-4} |
| Zhang [80] | 2014 | DNS | Coil | walk 3.58m/s (3.3Hz) | rucksack | 120 | 3.20×10^{-2} |

Table G.2: Literature experimental results; DNS = Damping No Storage, DS = Damping Storage, IFI = Impulse Frequency up-conversion Impact, IFP = Impulse Frequency up-conversion Plucking, IFB = Impulse Frequency up-conversion Base-impact.

Two additional literature searches were conducted in this project and their methods and results are presented in this appendix. The topics of the literature searches were Multi DoF vibration energy harvesters and generators with human motion vibration sources. Both literature searches were conducted in the databases of Google scholar, WebofScience and Researchgate.

Appendix H

References

References

- [1] CB Williams and Rob B Yates. Analysis of a micro-electric generator for microsystems. *sensors and actuators A: Physical*, 52(1):8–11, 1996.
- [2] BUNDU power. 225w solar panel.
- [3] Alibaba.com. Dynamo bicycle light set.
- [4] PULSAR. Drawing of kinetic watch mechanism.
- [5] Paul D Mitcheson, Eric M Yeatman, G Kondala Rao, Andrew S Holmes, and Tim C Green. Energy harvesting from human and machine motion for wireless electronic devices. *Proceedings of the IEEE*, 96(9):1457–1486, 2008.
- [6] Shad Roundy, Paul K Wright, and Jan Rabaey. A study of low level vibrations as a power source for wireless sensor nodes. *Computer communications*, 26(11):1131–1144, 2003.
- [7] Pieter de Jong. *Power Harvesting Using Piezoelectric Materials*. PhD thesis, PhD thesis, University of Twente, 2013.
- [8] Alper Erturk and Daniel J Inman. *Piezoelectric energy harvesting*. John Wiley & Sons, 2011.
- [9] Steve P Beeby, RN Torah, MJ Tudor, P Glynne-Jones, T O donnell, CR Saha, and S Roy. A micro electromagnetic generator for vibration energy harvesting. *Journal of Micromechanics and microengineering*, 17(7):1257, 2007.
- [10] Nathan S Shenck and Joseph A Paradiso. Energy scavenging with shoe-mounted piezoelectrics. *IEEE micro*, 21(3):30–42, 2001.
- [11] Haluk Kulah and Khalil Najafi. Energy scavenging from low-frequency vibrations by using frequency up-conversion for wireless sensor applications. *IEEE Sensors Journal*, 8(3):261–268, 2008.

- [12] Ibrahim Sari, Tuna Balkan, and Haluk Kulah. An electromagnetic micro energy harvester based on an array of parylene cantilevers. *Journal of Micromechanics and Microengineering*, 19(10):105023, 2009.
- [13] Paul D Mitcheson, Tim C Green, Eric M Yeatman, and Andrew S Holmes. Architectures for vibration-driven micropower generators. *Journal of microelectromechanical systems*, 13(3):429–440, 2004.
- [14] Daniel Hoffmann, Bernd Folkmer, and Yiannos Manoli. Fabrication, characterization and modelling of electrostatic micro-generators. *Journal of Micromechanics and Microengineering*, 19(9):094001, 2009.
- [15] Paul D Mitcheson, Elizabeth K Reilly, T Toh, Paul K Wright, and Eric M Yeatman. Performance limits of the three mems inertial energy generator transduction types. *Journal of Micromechanics and Microengineering*, 17(9):S211, 2007.
- [16] Alper Erturk, Jamil M Renno, and Daniel J Inman. Modeling of piezoelectric energy harvesting from an l-shaped beam-mass structure with an application to uavs. *Journal of intelligent material systems and structures*, 2008.
- [17] Ibrahim Sari, Tuna Balkan, and Haluk Klah. An electromagnetic micro power generator for low-frequency environmental vibrations based on the frequency upconversion technique. *Journal of Microelectromechanical Systems*, 19(1):14–27, 2010.
- [18] Tzeno Galchev, Hanseup Kim, and Khalil Najafi. Micro power generator for harvesting low-frequency and nonperiodic vibrations. *Journal of Microelectromechanical Systems*, 20(4):852–866, 2011.
- [19] Tudor M J Beeby, S P and White N M. Energy harvesting vibration sources for microsystems applications. *Measurement science and technology*, 17(12):R175, 2006.
- [20] KA Cook-Chennault, N Thambi, and AM Sastry. Powering mems portable devices, a review of non-regenerative and regenerative power supply systems with special emphasis on piezoelectric energy harvesting systems. *Smart Materials and Structures*, 17(4):043001, 2008.
- [21] D Alghisi, S Dalola, M Ferrari, and V Ferrari. Triaxial ball-impact piezoelectric converter for autonomous sensors exploiting energy harvesting from vibrations and human motion. *Sensors and Actuators A: Physical*, 233:569–581, 2015.
- [22] Miah A Halim, Hyunok Cho, Md Salauddin, and Jae Y Park. A miniaturized electromagnetic vibration energy harvester using flux-guided magnet stacks for human-body-induced motion. *Sensors and Actuators A: Physical*, 249:23–31, 2016.
- [23] Y Lu, F Cottone, S Boisseau, F Marty, D Galayko, and P Basset. A nonlinear mems electrostatic kinetic energy harvester for human-powered biomedical devices. *Applied Physics Letters*, 107(25):253902, 2015.

- [24] Lei Gu and Carol Livermore. Impact-driven, frequency up-converting coupled vibration energy harvesting device for low frequency operation. *Smart Materials and Structures*, 20(4):045004, 2011.
- [25] Seok-Min Jung and Kwang-Seok Yun. Energy-harvesting device with mechanical frequency-up conversion mechanism for increased power efficiency and wideband operation. *Applied Physics Letters*, 96(11):111906, 2010.
- [26] Seok-Min Jung and Kwang-Seok Yun. A wideband energy harvesting device using snap-through buckling for mechanical frequency-up conversion. In *Micro Electro Mechanical Systems (MEMS), 2010 IEEE 23rd International Conference on*, pages 1207–1210. IEEE, 2010.
- [27] Sergio P Pellegrini, Nima Tolou, Mark Schenk, and Just L Herder. Bistable vibration energy harvesters: a review. *Journal of Intelligent Material Systems and Structures*, page 1045389X12444940, 2012.
- [28] M Ferrari, V Ferrari, M Guizzetti, and D Marioli. A single-magnet nonlinear piezoelectric converter for enhanced energy harvesting from random vibrations. *Procedia Engineering*, 5:1156–1159, 2010.
- [29] Larry L Howell. *Compliant mechanisms*. John Wiley & Sons, 2001.
- [30] Larry L Howell, Spencer P Magleby, and Brian M Olsen. *Handbook of compliant mechanisms*. John Wiley & Sons, 2013.
- [31] Mattias Vangbo and Ylva Bäcklund. A lateral symmetrically bistable buckled beam. *Journal of Micromechanics and Microengineering*, 8(1):29, 1998.
- [32] Sachin Nadig, Serhan Ardanuc, and Amit Lal. Monolithic piezoelectric in-plane motion stage with low cross-axis-coupling. In *Micro Electro Mechanical Systems (MEMS), 2014 IEEE 27th International Conference on*, pages 524–527. IEEE, 2014.
- [33] Sachin Nadig, Serhan Ardanuc, and Amit Lal. Planar laser-micro machined bulk pzt bimorph for in-plane actuation. In *Applications of Ferroelectric and Workshop on the Piezoresponse Force Microscopy (ISAF/PFM), 2013 IEEE International Symposium on the*, pages 152–155. IEEE, 2013.
- [34] Ryan R Knight, Changki Mo, and William W Clark. Mems interdigitated electrode pattern optimization for a unimorph piezoelectric beam. *Journal of electroceramics*, 26(1-4):14–22, 2011.
- [35] Leonard Meirovitch. *Fundamentals of vibrations*. Waveland Press, 2010.
- [36] A Mahmood Paracha, P Basset, CLP Lim, F Marty, P Poulichet, G Amendola, and T Bourouina. Design and fabrication issues of a silicon-based vibration powered electric energy generator using parallel plate and in-plane mechanism. In *IECON 2006-32nd Annual Conference on IEEE Industrial Electronics*, pages 2915–2920. IEEE, 2006.

- [37] Yong Zhu, SOR Moheimani, and MR Yuce. A 2-dof wideband electrostatic transducer for energy harvesting and implantable applications. In *Sensors, 2009 IEEE*, pages 1542–1545. IEEE, 2009.
- [38] A Mahmood Paracha, P Basset, D Galayko, A Dudka, F Marty, and T Bourouina. Mems dc/dc converter for 1d and 2d vibration-to-electricity power conversion. In *TRANSDUCERS 2009-2009 International Solid-State Sensors, Actuators and Microsystems Conference*, pages 2098–2101. IEEE, 2009.
- [39] U Bartsch, J Gaspar, and O Paul. A 2d electret-based resonant micro energy harvester. In *Micro Electro Mechanical Systems, 2009. MEMS 2009. IEEE 22nd International Conference on*, pages 1043–1046. IEEE, 2009.
- [40] U Bartsch, J Gaspar, and O Paul. Low-frequency two-dimensional resonators for vibrational micro energy harvesting. *Journal of Micromechanics and Microengineering*, 20(3):035016, 2010.
- [41] Bin Yang, Chengkuo Lee, Rama Krishna Kotlanka, Jin Xie, and Siak Piang Lim. A mems rotary comb mechanism for harvesting the kinetic energy of planar vibrations. *Journal of Micromechanics and Microengineering*, 20(6):065017, 2010.
- [42] Yong Zhu, SO Reza Moheimani, and Mehmet Rasit Yuce. A 2-dof mems ultrasonic energy harvester. *IEEE Sensors journal*, 11(1):155–161, 2011.
- [43] Huicong Liu, Bo Woon Soon, Nan Wang, CJ Tay, Chenggen Quan, and Chengkuo Lee. Feasibility study of a 3d vibration-driven electromagnetic mems energy harvester with multiple vibration modes. *Journal of Micromechanics and Microengineering*, 22(12):125020, 2012.
- [44] Sehwan Kim and Kukjin Chun. 2d vibration based mems energy harvester. In *Int. Conf. on Renewable Energies and Power Quality*, 2012.
- [45] Anthony G Fowler, SO Reza Moheimani, and Sam Behrens. A 3-dof mems ultrasonic energy harvester. In *Sensors, 2012 IEEE*, pages 1–4. IEEE, 2012.
- [46] M Cueff and S Basrour. A multi degree of freedom vibration magnetic energy harvester for transport application. In *Journal of Physics: Conference Series*, volume 476, page 012092. IOP Publishing, 2013.
- [47] V Janicek and M Husak. Designing the 3d electrostatic microgenerator. *Journal of Electrostatics*, 71(3):214–219, 2013.
- [48] Andrea Crovetto, Fei Wang, and Ole Hansen. An electret-based energy harvesting device with a wafer-level fabrication process. *Journal of Micromechanics and Microengineering*, 23(11):114010, 2013.
- [49] AG Fowler, SOR Moheimani, and S Behrens. A 3-dof soi mems ultrasonic energy harvester for implanted devices. In *Journal of Physics: Conference Series*, volume 476, page 012002. IOP Publishing, 2013.

- [50] Anthony G Fowler, SO Reza Moheimani, and Sam Behrens. Design and characterization of a 2-dof mems ultrasonic energy harvester with triangular electrostatic electrodes. *IEEE Electron Device Letters*, 34(11):1421–1423, 2013.
- [51] Jacopo Iannacci, Guido Sordo, Massimo Gottardi, Thomas Kuenzig, Gabriele Schrag, and Gerhard Wachutka. An energy harvester concept for electrostatic conversion manufactured in mems surface micromachining technology. In *Semiconductor Conference Dresden-Grenoble (ISCDG), 2013 International*, pages 1–4. IEEE, 2013.
- [52] Bian Wei, Xiaoming Wu, Ling Bu, Xiaohong Wang, and Litian Liu. Multiple axes vibration energy harvester based on ptfе and metal balls. In *2013 Transducers & Eurosensors XXVII: The 17th International Conference on Solid-State Sensors, Actuators and Microsystems (TRANSDUCERS & EUROSENSORS XXVII)*, pages 2253–2256. IEEE, 2013.
- [53] Hao Wu, Lihua Tang, Yaowen Yang, and Chee Kiong Soh. Feasibility study of multi-directional vibration energy harvesting with a frame harvester. In *SPIE Smart Structures and Materials+ Nondestructive Evaluation and Health Monitoring*, pages 905703–905703. International Society for Optics and Photonics, 2014.
- [54] Jin Yang, Xihai Yue, Yumei Wen, Ping Li, Qiangmo Yu, and Xiaoling Bai. Design and analysis of a 2d broadband vibration energy harvester for wireless sensors. *Sensors and Actuators A: Physical*, 205:47–52, 2013.
- [55] Mengdi Han, Wen Liu, Bo Meng, Xiao-Sheng Zhang, Xuming Sun, and Haixia Zhang. Springless cubic harvester for converting three dimensional vibration energy. In *2014 IEEE 27th International Conference on Micro Electro Mechanical Systems (MEMS)*, pages 425–428. IEEE, 2014.
- [56] Kai Tao, Shuwei Liu, Sun Woh Lye, Jianmin Miao, and Xiao Hu. A three-dimensional electret-based micro power generator for low-level ambient vibrational energy harvesting. *Journal of Micromechanics and Microengineering*, 24(6):065022, 2014.
- [57] DF Berdy, DJ Valentino, and D Peroulis. Kinetic energy harvesting from human walking and running using a magnetic levitation energy harvester. *Sensors and Actuators A: Physical*, 222:262–271, 2015.
- [58] Benjamin J Bowers and David P Arnold. Spherical, rolling magnet generators for passive energy harvesting from human motion. *Journal of Micromechanics and Microengineering*, 19(9):094008, 2009.
- [59] Dong-Hoon Choi, Chang-Hoon Han, Hyun-Don Kim, and Jun-Bo Yoon. Liquid-based electrostatic energy harvester with high sensitivity to human physical motion. *Smart Materials and Structures*, 20(12):125012, 2011.
- [60] Matthias Geisler, Sebastien Boisseau, Matthias PEREZ, Pierre Gasnier, Jerome Willemin, Imene Ait-Ali, and Simon Perraud. Human-motion energy harvester for autonomous body area sensors. *Smart Materials and Structures*, 2016.

- [61] MA Halim and JY Park. Optimization of a human-limb driven, frequency up-converting electromagnetic energy harvester for power enhancement. In *Solid-State Sensors, Actuators and Microsystems (TRANSDUCERS), 2015 Transducers-2015 18th International Conference on*, pages 1013–1016. IEEE, 2015.
- [62] Miah Abdul Halim and Jae Yeong Park. Piezoelectric energy harvester using impact-driven flexible side-walls for human-limb motion. *Microsystem Technologies*, pages 1–9, 2017.
- [63] Miah A Halim and Jae Y Park. A non-resonant, frequency up-converted electromagnetic energy harvester from human-body-induced vibration for hand-held smart system applications. *Journal of Applied Physics*, 115(9):094901, 2014.
- [64] A Haroun, I Yamada, and S Warisawa. Investigation of kinetic energy harvesting from human body motion activities using free/impact based micro electromagnetic generator. *Diabetes Cholest metabol*, 1(104):13–16, 2016.
- [65] Pratik Patel and Mir Behrad Khamesee. Electromagnetic micro energy harvester for human locomotion. *Microsystem technologies*, 19(9-10):1357–1363, 2013.
- [66] P Pillatsch, EM Yeatman, and AS Holmes. A scalable piezoelectric impulse-excited energy harvester for human body excitation. *Smart Materials and Structures*, 21(11):115018, 2012.
- [67] Pit Pillatsch, Eric M Yeatman, and Andrew S Holmes. A piezoelectric frequency up-converting energy harvester with rotating proof mass for human body applications. *Sensors and Actuators A: Physical*, 206:178–185, 2014.
- [68] P Pillatsch, EM Yeatman, and AS Holmes. Real world testing of a piezoelectric rotational energy harvester for human motion. In *Journal of Physics: Conference Series*, volume 476, page 012010. IOP Publishing, 2013.
- [69] Yuan Rao, Shuo Cheng, and David P Arnold. An energy harvesting system for passively generating power from human activities. *Journal of Micromechanics and Microengineering*, 23(11):114012, 2013.
- [70] Yuan Rao, Kelly M McEachern, and David P Arnold. A compact human-powered energy harvesting system. *Energy Harvesting and Systems*, 1(1-2):89–100, 2014.
- [71] Michael Renaud, Paolo Fiorini, Rob van Schaijk, and Chris Van Hoof. Harvesting energy from the motion of human limbs: the design and analysis of an impact-based piezoelectric generator. *Smart Materials and Structures*, 18(3):035001, 2009.
- [72] Edwar Romero, Robert O Warrington, and Michael R Neuman. Body motion for powering biomedical devices. In *Engineering in Medicine and Biology Society, 2009. EMBC 2009. Annual International Conference of the IEEE*, pages 2752–2755. IEEE, 2009.

- [73] CR Saha, T O donnell, N Wang, and P McCloskey. Electromagnetic generator for harvesting energy from human motion. *Sensors and Actuators A: Physical*, 147(1):248–253, 2008.
- [74] Md Salauddin and Jae Y Park. Design and experiment of human hand motion driven electromagnetic energy harvester using dual halbach magnet array. *Smart Materials and Structures*, 2017.
- [75] Sheng Wei, Hong Hu, and Siyuan He. Modeling and experimental investigation of an impact-driven piezoelectric energy harvester from human motion. *Smart Materials and Structures*, 22(10):105020, 2013.
- [76] Longhan Xie, Jiehong Li, Siqi Cai, and Xiaodong Li. Design and experiments of a self-charged power bank by harvesting sustainable human motion. *Advances in Mechanical Engineering*, 8(5):1687814016651371, 2016.
- [77] K Ylli, D Hoffmann, A Willmann, B Folkmer, and Y Manoli. Investigation of pendulum structures for rotational energy harvesting from human motion. In *Journal of Physics: Conference Series*, volume 660, page 012053. IOP Publishing, 2015.
- [78] K Ylli, D Hoffmann, P Becker, A Willmann, B Folkmer, and Y Manoli. Human motion energy harvesting for aal applications. In *Journal of Physics: Conference Series*, volume 557, page 012024. IOP Publishing, 2014.
- [79] K Ylli, D Hoffmann, A Willmann, P Becker, B Folkmer, and Y Manoli. Energy harvesting from human motion: exploiting swing and shock excitations. *Smart Materials and Structures*, 24(2):025029, 2015.
- [80] Qian Zhang, Yufeng Wang, and Eun Sok Kim. Power generation from human body motion through magnet and coil arrays with magnetic spring. *Journal of Applied Physics*, 115(6):064908, 2014.